MICROCOPY RESOLUTION TEST CHART

NATIONAL BUREAU OF STANDARDS-1963-A

NAVAL POSTGRADUATE SCHOOL
Monterey, California

THESIS

INTERPRETATION OF A SAR IMAGE
OF THE BAY OF BISCAY

by

Jean-François Soubrier

September 1983

Thesis Advisor: C. N. K. Mooers
                               J. L. Mueller

83

REPORT DOCUMENTATION PAGE		READ INSTRUCTIONS BEFORE COMPLETING FORM
1. REPORT NUMBER	2. GOVT ACCESSION NO. AD-A135 981	3. RECIPIENT'S CATALOG NUMBER
4. TITLE (and Subtitle) Interpretation of a SAR image of the Bay of Biscay		5. TYPE OF REPORT & PERIOD COVERED Master's Thesis September, 1983
		6. PERFORMING ORG. REPORT NUMBER
7. AUTHOR(s) Jean-Francois Soubrier		8. CONTRACT OR GRANT NUMBER(s)
9. PERFORMING ORGANIZATION NAME AND ADDRESS Naval Postgraduate School Monterey, California 93943		10. PROGRAM ELEMENT, PROJECT, TASK AREA & WORK UNIT NUMBERS
11. CONTROLLING OFFICE NAME AND ADDRESS Naval Postgraduate School Monterey, California 93943		12. REPORT DATE September 1983
		13. NUMBER OF PAGES 135
14. MONITORING AGENCY NAME & ADDRESS(if different from Controlling Office)		15. SECURITY CLASS. (of this report) UNCLASSIFIED
		15a. DECLASSIFICATION/DOWNGRADING SCHEDULE

16. DISTRIBUTION STATEMENT (of this Report)

Approved for public release, distribution unlimited.

17. DISTRIBUTION STATEMENT (of the abstract entered in Block 20, if different from Report)

18. SUPPLEMENTARY NOTES

19. KEY WORDS (Continue on reverse side if necessary and identify by block number)

Bay of Biscay	Synthetic Aperture Radar	Military Oceanography
Golfe de Gascagne	Remote Sensing	Oceanic Canyons
Armorican Shelf	Imaging Radar	Wave Current Interaction
Celtic Sea	Shelfbreak Jet	Tidal Internal Waves

20. ABSTRACT (Continue on reverse side if necessary and identify by block number)

On August 20, 1978, the Synthetic Aperture Radar (SAR) on board the satellite SEASAT, gave evidence of high energy internal oceanic activity at the shelfbreak in the northern part of the Bay of Biscay.

Quantitive spatial measurements of internal wave patterns were correlated with conventional, quasi-synoptic in situ data and yielded phase speeds of 0.55M/S for high frequency, nonlinear internal waves, generated in groups at the canyons indenting the shelfbreak and at the time of low tide in Brest.

Block 20 Cont'd.

Their periods were found to be of 70MIN and their amplitudes estimated to be 15M. Ocean swell refraction, observed on the SAR image, together with a localized significant increase in wave height detected by the SEASAT altimeter, was related to the shear of a northwestward geostrophic jet (ca. 0.5M/S) at the break.

Possible operational consequences of these features are summarized as an assessment of a SAR's capability to give tactical as well as scientific real-time information on the internal ocean.

DTIC COPY INSPECTED 3

Accession For	
NTIS GRA&I	☒
DTIC TAB	☐
Unannounced	☐
Justification	
By	
Distribution/	
Availability Codes	
Dist	Avail and/or Special
A/1	

Interpretation
of a SAR Image
of the Bay of Biscay

by

Jean-Francois Soubrier
Lieutenant de Vaisseau, French Navy

Submitted in partial fulfillment of the
requirements for the degree of

MASTER OF SCIENCE IN METEOROLOGY AND OCEANOGRAPHY

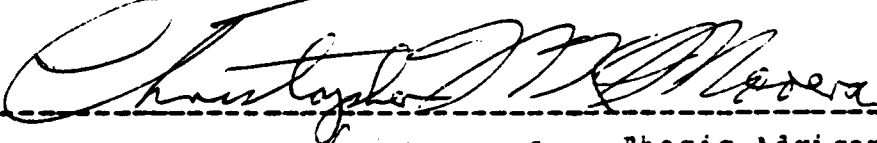from the

NAVAL POSTGRADUATE SCHOOL
September 1933
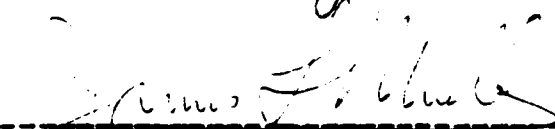
Author: _____

Approved by: _____
                                              Thesis Advisor

_____
                                              Second Reader

_____
                   Chairman, Department of Oceanography

_____
                        Dean of Science and Engineering

3

ABSTRACT

On August 20, 1978, the Synthetic Aperture Radar (SAR) on board the satellite SEASAT, gave evidence of high energy internal oceanic activity at the shelfbreak in the northern part of the Bay of Biscay.

Quantitative spatial measurements of internal wave patterns were correlated with conventional, quasi-synoptic in situ data and yielded phase speeds of 0.55M/S for high frequency, nonlinear internal waves, generated in groups at the canyons indenting the shelfbreak and at the time of low tide in Brest. Their periods were found to be of 70MIN and their amplitudes estimated to be 15M. Ocean swell refraction, observed on the SAR image, together with a localized significant increase in wave height detected by the SEASAT altimeter, was related to the shear of a northwestward geostrophic jet (ca. 0.5M/S) at the break.

Possible operational consequences of these features are summarized as an assessment of a SAR's capability to give tactical as well as scientific real-time information on the internal ocean.

4

RESUME

Le 20 Août 1978, le SAR (Synthetic Aperture Radar) embarqué sur le satellite SEASAT, a mis en évidence une intense activité interne de l'océan au voisinage du talus continental dans la partie nord du Golfe de Gascogne.

Des mesures quantitatives des manifestations de surface des ondes internes ont été corrélées avec des données conventionnelles "in-situ", et quasi simultanées. Des vitesses de phase de 0,55 mètres par seconde ont été mises en évidence pour les trains d'ondes internes non-linéaires, générés a l'heure de la basse mer de Brest, dans les canyons bordant le plateau continental; la période de ces ondes est de 70 minutes et leur amplitude a ete estimée a 15 mètres. La réfraction de la houle observée sur l'image SAR, en conjonction avec l'observation par l'altimètre de SEASAT d'une amplification localisée mais significative de la hauteur de vague, a ete attribuée au courant de cisaillement dun "jet" géostrophique de surface (de l'ordre de 0,5 mètres par seconde) portant vers le nord-ouest le long du talus.

Les conséquences opérationelles possibles de ces phénomènes sont récapitulées, pour démontrer les capacités d'un radar SAR à donner des informations tactiques aussi bien que scientifiques, en temps réel, sur l'océan interne.

TABLE OF CONTENTS

7

8

LIST OF TABLES

LIST OF FIGURES

ACKNOWLEDGMENTS

I. INTRODUCTION

A. FOREWARD

Remote sensing gives satellites an essential role in the
monitoring of ocean variability. Synthetic Aperture Radar
(SAR) in particular, has the ability to display images of
surface manifestations of internal processes which could
typically only be inferred from lengthy and costly in-situ
sampling from ships at sea or instrumented buoys. Even
though the dynamical nonlinear linkage involved in the SAR
imaging mechanism is presently incompletely understood, the
vivid and spectacular images ; e.g., as those acquired by
SEASAT, give a tremendous amount of information about well-
known or totally new oceanic phenomena. To study such an
image of the Bay of Biscay (Fig. 1.1 and 1.2) was a chal-
lenging and exciting topic of thesis research for the author
who has experienced, over several years, the sea-going
approach to military oceanography in this area. The excep-
tional opportunity for doing such research was offered at
the Naval Postgraduate School where direct support was found
and the introduction to other facilities was given, espe-
cially to the Fleet Numerical Oceanography Center in
Monterey and to the Jet Propulsion Laboratory in Pasadena.

B. DATA ACQUISITION

The optically processed SAR image was the starting point
of the total data set collected. It was forwarded by the
Jet Propulsion Laboratory (JPL) of the California Institute
of Technology in Pasadena, and a first heuristic study of
the image gave the necessary evidence of its research possi-
bilities. The swath is 100KM wide and goes roughly from

14

Brest in Britanny to La Coruna in Galicia; internal wave activity is clearly visible, particularly over the continental slope (Fig. 1.2).

Conventional, quasi-synoptic data were then sought and requested, either directly through the French Navy authorities, or by the Naval Postgraduate School from U.S. and foreign, military and civilian institutions.

A fairly dense set of XBT's (bathythermographs) was collected from the Fleet Numerical Oceanography Center (FNOC) and the French "Service Hydrographique et Oceanographique de la Marine" (SHOM). The format of these BT's gave the depth-temperature pairs at turning points; only five profiles extend below 500M. Sixty nine XBT profiles were finally considered, corresponding to a time period of seven days around the SAR date and located in the neighbourhood of the image. The densest spacing covers the continental slope, but not where the most intense activity is noted from the SAR image.

Local atmospheric data were obtained from the French National Weather Service. Global weather charts over the Atlantic Ocean and swell hindcast for the Bay of Biscay were obtained from the FNOC archive center.

Contemporaneous moored current meter time series were considered as important auxiliary information regarding the internal baroclinic modes of vertical movements, and the mean flow. The closest mooring was a subsurface array at 1524, 3032, 3976M depth anchored at 46°57'2N, 009°57'1W during the Northeastern Atlantic Deep Sea (NEADS) mission. The digital data (current speed, direction, temperature, recorded depth) were forwarded by the "Centre National d'Exploitation des Oceans" in Brest, where the " Bureau National des Donnees Oceaniques" is located.

Other satellite sensors carried by SEASAT acquired substantial information on the same area at rapid intervals. It was another privilege to get direct computer access to the Pilot Ocean Data System (PODS) of JPL, thus enabling a thorough survey of related data given by the SEASAT altimeter and scatterometer.

Climatological data were blended from several sources in the open literature, recent papers and official unclassified documents of the U.S. and French Navies.

C. OBJECTIVES

The main aim in this study is to establish a definite correlation between the SAR surface patterns and internal quasi-synoptic features established by other means: conventional hydrographic observations, current observations and other satellite sensors.

Avoiding the complex problem of physical linkage in the SAR imaging process, a pragmatic, heuristic approach to SAR analysis was made, thus tentatively establishing the power of SAR to monitor the oceans. The study has been restricted to the upper layer of the Bay of Biscay on each side of the continental slope and shelfbreak, where both the SAR image and other data bases were found to provide rich information. Being interested only in internal oceanic features, the swell was only considered in regards to interaction with quasi-steady currents.

In the course of the research, many different topics had to be considered, thus greatly enhancing the personal benefit that could be gathered strictly from the SAR study. Conversely, this fact, added to the limits in time and scientific expertise of the author, prevents this study from being in any way exhaustive. Furthermore, an inherent feature of this kind of quasi-synoptic study is its

16

inability to support objective "sea-truth". All the results presented here must be thought of as describing a particular event at a particular time and in a particular environment that can only be considered as part of the ever-growing information available to oceanographers.

Overall, the objective of a thesis is to increase the knowledge of the author himself and, in this case, in topics related both to the use of conventional methods and of promising satellite-related techniques. Consequently, this research was a learning experience and an enriching introduction to the new era of operational military satellite oceanography.

D. UNITS NOTATIONS CONVENTIONS

Unless explicitly stated otherwise, the following units will be used, with the S.I. system as a general basis.

Units of time

GMT Greenwich time (Z) in Hours, Minutes, Seconds.
(The local summer time in France is: GMT-020000;
the solar time at the SAR image location is: GMT-002000)
Day-Hour groups are expressed as DDHHMM, implicitly days of August 1978.

Units of length

Depths in meters (M)
Distances in kilometers (KM)

Units of temperature.

Degrees Celsius (^{0}C).

Geographic coordinates

Geographic units are expressed in decimal degrees of latitude and longitude (lat,lon). Longitudes are counted from 0 to 360 in most computations.

Auxiliary geographic grid

An auxiliary Cartesian grid was adjusted over a map projection of the area to meet the needs of the particular SAR image orientation and general bathymetric gradient (Fig. 1.1) This grid is in units of kilometers. The x-axis is oriented along the shelfbreak with positive values towards the southeast (directed seaward in the Bay).

The y-axis is oriented along the center of the SAR swath and towards the northeast (directed onto the French continental shelf).

Hence x values give the relative positions on each side of the SAR image : ($|x| < 60$ for locations on the ground track). y values give relative positions on each side of the shelfbreak.

The transformation was established as follows :

Two geographic points clearly visible on the SAR image and a representative offshore bathymetric sounding were chosen to get the linear transform parameters.

lat 47.80	x=000.00	
lon 355.67	y=132.42	Penmarc'h point.
lat 43.59	X=000.00	
lon 352.74	Y=-388.92	Los Cairos point.
lat 46.00	X=116.7	
lon 356.00	Y=000.00	Offshore reference.

The corresponding relationships are :

$$lat = -0.006261 \ X + 0.008075 \ Y + 46.73$$

$$lon = 0.009205 \ X + 0.005620 \ Y + 354.92$$

$$X = -51.315 \ lat + 73.73 \ lon - 23772.$$

$$y = 34.050 \ lat + 57.17 \ lon - 24217.$$
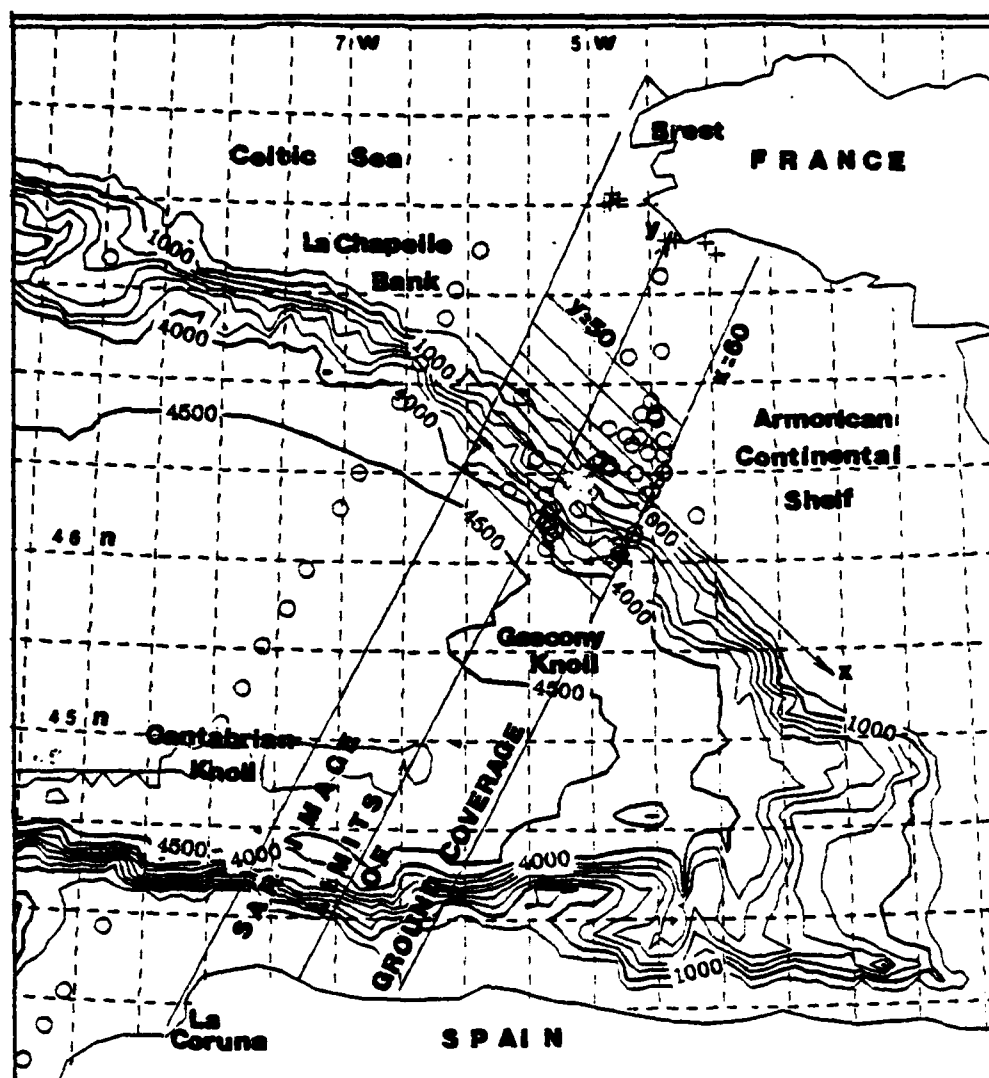
Conformal biconic projection.
Circles locate XBT soundings.
Isobaths (in meters) are smoothed to 10KM.

Figure 1.1   GEOGRAPHIC GRID.
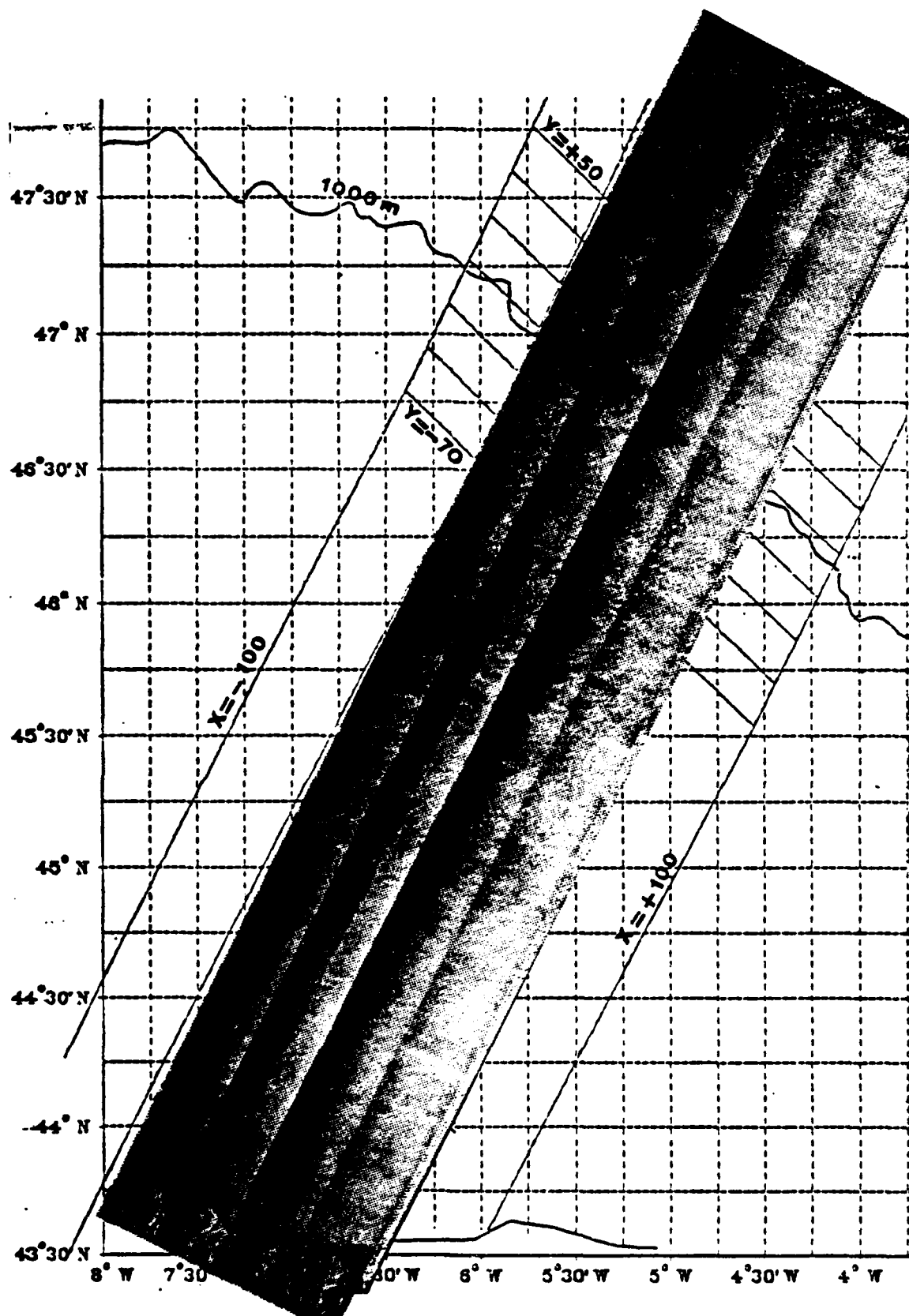
Figure 1.2   PHOTO REPRODUCTION OF THE SAR IMAGE.

II. SAR IMAGING OF INTERNAL WAVES

Starting with a survey of the recent literature on the SAR principles and its capabilities to detect oceanic features, the various assessments made of the dominant mechanisms of interaction between an internal wave field and the short wind-driven capillary/ultragravity waves that a SAR can detect are reviewed.

A. SYNTHETIC ANTENNAS

Synthesizing a radar antenna consists of using a moving antenna of limited size and combining all information gathered on a given point of the earth during a given time interval (Fig. 2.2). The distance of travel on the orbit gives the length of a virtual antenna of much finer resolution. The resulting resolution is independent of range and speed, and it is theoretically half the real antenna's aperture. In the range (cross-velocity) direction, the length of coherent pulses determine (in the usual way) the corresponding accuracy.

In the case of SEASAT, the data were transmitted in real time by the satellite to one of the special processing earth stations. The final record is either a computer-compatible tape format, or a film conversion. The photographic output is displayed in four parallel subswaths to account for a progressive decrease in the radar response intensity with range (Fig. 1.2). Some particular images over limited areas have been digitally processed with a valuable enhancement of resolution.

21

The extraction of a two-dimensional surface image spectrum is done either by an optical Fast Fourier Transform [Gonzales 1979 and Shuchman 1978], or by numerical methods [algorithm of Hasselman 1980]. Considerations of the relative qualities of these processing techniques can be found in Mitchel [1982] and Tomiyasu [1978].

Characteristics of the SEASAT SAR are given here (Table I and Fig. 2.1).

TABLE I
SEASAT SAR CHARACTERISTICS

satellite altitude	800 KM
satellite velocity	7.2 KM/S
near-polar orbit	108 degrees
view angle from nadir	20 degrees
swath width	100 KM
wavelength	.235 M
frequency L-band	1275 GHZ
real antennae	11x2 M
synthetic antenna	15 KM
antenna polarization	99 % linear horiz.
contrast ratio	9 dB
radar gain	35 dB
processing resolution	25 M
pulse repetition rate	500 microseconds
pulse length	33.4 microseconds

B. OCEAN IMAGING MECHANISMS

The application of SAR systems to oceanography requires extension of the basic SAR earth imaging theory to account for scattering from a time-varying surface that satisfies nonlinear hydrodynamic constraints. On the other hand, the general scattering models for low resolution radars do not apply to the spaceborne high-resolution SAR's. The complexity of the problem results from the widely nonlinear electromagnetic and hydrodynamic interactions. But this nonlinearity is at the same time the main reason for the

22

remarkable capabilities of SAR for detection of mesoscale oceanic phenomena.

1. Doppler Effects from the Moving Ocean Surface

The fact that the ocean surface is not rigid has two effects: (1) defocusing of the SAR image and (2) apparent displacement of the radar echo, as can be seen by comparing echos of moving ships and their stationnary wakes (Cf para V-B-1).

Empirical studies have shown that to recover the optimal focus of SAR imagery over ocean surfaces, the best speed correction to use is the long wave phase velocity, and not as would seem intuitively, the long waves orbital velocity on which the capillary short waves ride. In the case of internal waves, this phase velocity is given by

$$ c_P^2 = g h \frac{\rho_2 - \rho_1}{\rho_2} $$

where "h" is the depth of the thermocline and "ρ_1", "ρ_2" are the densities each side of the thermocline. This displacement effect will periodically modulate the image intensity backscattered by long waves, causing in some cases periodic dark and light bands associated with the pattern of the real long wave pattern. In the case of a "closing" current (cross-track component toward the satellite) the surface image will be artificially translated in the positive along-track direction; hence if this "closing" current is increasing along-track (fig 2.3), the value of this translation will increase accordingly and there will be stretching of the image and a lower Bragg-scatter than expected.

23

2. Scattering of Radar Signal from Ocean Waves

Based on a review [Valenzuela 1978] of electromagnetic wave scattering from ocean waves, the standard approach considers the ocean surface as statistically described, but a deterministic formulation might be more appropriate when the resolution area is small enough to correspond to a few wavelengths only. The former description is nevertheless easier and most of the time more accurate. The statistical approach may lead either to a Bragg-resonance-like mechanism or a "facet" mechanism (tangent-plane theory) [Brown 1976].

3. Bragg Model versus Tangent Plane Model

The Bragg mechanism is limited to rough surfaces satisfying the Rayleigh criterion :

$$2 k H(rms) \cos \theta \leq \frac{\pi}{2} ,$$

where "H" is the typical surface height fluctuation and "θ" is the incident angle of the radar wave on the water surface. The total backscatter is then given by :

$$\sigma^{\circ}(\theta, k)_{i,j} = 16 \pi k^4 \cos^4 \theta \left| g_{i,j}(\theta) \right|^2 \psi(K_x, K_y) ,$$

where "$\psi(K_x, K_y)$" is the two-dimensional Fourier spectrum of the sea surface with an ocean wavenumber "$2k\cos\theta$" and "$g_{i,j}$" represents the radar reflectivity of the air-water interface. The alternative approach is the tangent plane or facet model applicable to gently undulating rough surfaces and small ($\theta \ll 30^{\circ}$) incidence angles (for SEASAT SAR, $\theta = 23^{\circ}$).

We have in this case

$$\sigma^{\circ}(\theta, s) = \frac{|R(0)|^2}{2 \langle s^2 \rangle} \sec^4 \theta \exp\left(-\frac{\tan^2 \theta}{2 \langle s^2 \rangle}\right) \psi(K_x, K_y),$$

where $R(0)$ is the Fresnel coefficient for normal incidence and "$<s^2>$" is the total slope variance for ocean waves of long period. In both cases the intensity variations of the SAR signal will be correlated to the energy density "Ψ" of the ocean waves. (They will be at the same time modified by the mean incidence angle, resulting in a decreasing average intensity along a cross track line.) Therefore, the nonlinear periodic energy tranfer from the capillary waves to the mesoscale phenomena (currents, swell and internal waves) will dramatically affect the SAR imagery.

C. COUPLING WITH INTERNAL OCEAN DYNAMICS

Small coherent disturbances in the current field can cause important modulations in the ultragravity wavefield [Mollo-Christensen 1982] : e.g., for wavelengths of 30 cms, a shear current of 0.003 M/sec can induce a modulation at the surface to which a SAR will be sensitive.

1. The Surface Straining and the Bunching Effects

The possible mechanism involved appear to be either an hydrodynamic effect (the surface straining), or a Doppler effect (the bunching).

The straining effect applies to all internal ocean phenomena (internal waves, shear currents, eddies). Variations of "σ^0" along the direction of wave propagation are induced by hydrodynamic interactions between short resonant waves ($\lambda \simeq .3M$) and large ocean periodic motions ($\lambda > 100M$). This mechanism can be thought of as an alternating pattern of divergence-convergence of the free surface, riding on a long-wave modulation (swell or internal wave). The resonant waves are saturated locally at the region of maximum convergence of velocity, ahead of the wave crest (Fig. 2.4).

25

In the short wave (Phillips) spectrum, the modulation transfer function can be written [Alpers,Ross and Ruffenach 1981]:

$$R_{hydr.} = -4.5\,\Omega\,\frac{\Omega - i\mu}{\Omega^2 + \mu^2}\,\sin^2\phi,$$

where "μ" is a time constant related to the resonant waves, "ϕ" is the angle between the flight (azimuth) direction and the direction of propagation of the internal wave, and "Ω" is the angular frequency of the wave component.

The velocity bunching effect is the result of artificial displacement of the image of periodically moving surface [Alpers and Rufenach 1979, Alpers et al. 1981]. Simply put, the Doppler shift due to surface velocity is attributed to location (azimuth) and the signal is mislocated in the image. It seems to be the best model for azimuth traveling swell and eventually for internal waves. However, it is a geometric effect that does not account for energy transfer as well as the surface straining dynamic mechanism.

2. Application to Internal Waves

The general form of "σ^o" for a wave component of wave number "$\vec{K}$", angular frequency "Ω", and amplitude "A", may therefore be written more generally as [Vesecky and Stewart 1982]:

$$\sigma^o = \langle\sigma^o\rangle\left[1 + \frac{R}{A}\cos\left(\vec{K}\cdot\vec{r} - \Omega + \zeta\right)\right],$$

with

$$\zeta = \arctan\left[\frac{Im\,(R)}{Re\,(R)}\right],$$

where "R" is the total modulational transfer function and can be considered as the result of two different mechanisms (neglecting the tilting effect applicable only to swell):

$$R = R(hydrodyn.) + R(vel.bunching)$$

With a theory relating the surface wave field to the internal wave amplitude and surface winds, information on the internal wave amplitude, and simultaneously on the wind field, can be obtained from the imagery. However, such a theory is not available yet [Beal 1981].

It is generally believed that internal waves are seen by a radar as a result of two mechanisms :

(1) The surface currents associated with the internal wave field sweep together surface oils and materials in the surface water convergence zones resulting in severe damping of short capillary/gravity waves to form slicks, and

(2) The surface current field induced by the internal waves result in a periodic modulation of the height of the capillary/gravity waves.

Actually the two possible mechanisms implied give contradictory results: damping by oil slicks will occur over the convergence lines, whereas the current hydrodynamic damping will be localized on the divergence areas. It is the author's assumption that whenever the surface patterns visible on the SAR image are linear, localized and filamentary (Cf patterns described in V-B-1), the oil slick explanation is appropriate, whereas alternation of high and low brightness can be more easily explained by hydrodynamical damping due to internal waves (Cf group patterns described in V-B-3 and V-B-4).

According to the surface straining mechanism, an internal wave traveling at phase speed "c" produces a surface straining and a velocity pattern "u(x-ct)" moving with the waves. Short surface gravity waves traveling in the same general direction as the internal waves can strongly interact, particularly when the group velocity of the surface wave is close to the phase velocity of the internal wave.

27

Gargett and Hughes [1981] give another description of the same principle. The horizontal surface currents associated with internal waves are large, being of the same order as the wave phase velocities themselves. They are oriented approximately either parallel (in the troughs) antiparallel (on the crests), to the direction of propagation. A wind field superimposed on the current will excite a capillary/ultragravity wave spectrum that is steeper where the wind opposes the internally generated current than where it is parallel to it (Fig. 2.4). Eventually, a modulational interaction couples the surface-wave spectrum to that of the internal waves and possibly creates a growth of the latter [Dysthe 1981].

Indirect detection of internal waves may be possible by analyzing the variations of the swell energy spectrum directly extracted by FFT of the SAR data. Refraction of the swell is then the mechanism by which the internal waves are manifested on the sea surface.

D. SENSITIVITY OF A SAR TO INTERNAL MOTIONS

1. Environmental Limitations

For possible radar imaging of ocean internal wave motion, the first essential condition is the existence of surface capillary or ultra-gravity waves. This excludes total calm wind conditions, but not rough and even breaking seas. The relative directions of the short surface waves and the internal wave field affects the hydrodynamical interaction process. Furthermore, the displacement of the satellite may induce Doppler imaging effects dependent on the angle which the radar waves make with the surface waves. Hence , for a given internal wave field and known satellite orbit parameters, the optimal wind velocity conditions could be stated. It seems, but it would need experimental confir-

mation, that a wind blowing parallel to the propagation of
the internal waves is optimal for strong interaction. The
radar modulation is largest for internal waves traveling in
azimuthal direction, but on the other hand, it is assumed
that a satellite track parallel to the same internal wave
field may induce enhancing Doppler-effects.

That these geophysical factors are sometimes contra-
dictory does not seem, however, to inhibit the capability of
a SAR to display surface manifestations (observed in many
different cases) of internal motions. In particular the
analysis conducted in chapter V shows internal waves propa-
gating in almost all relative directions, thus proving that
at least some interaction and radar modulation exists for
every configuration.

2. Propitious Internal Wave Properties

The group velocity of wind-driven short waves is
given by

$$c_g^2 = \frac{g}{2k} + kT,$$

where "T" is the surface tension. The optimal internal wave
phase speed should then be of the same order such that

$$gH \frac{\Delta\rho}{\rho} \approx \frac{g}{2k},$$

implying approximately for ultra-gravity waves

$$\frac{\Delta\rho}{\rho} \approx \frac{1}{2kH},$$

which, in the case of the 30CM wavelength waves that SEASAT
SAR can detect gives

$$\frac{\Delta\rho}{\rho} \approx \frac{1}{40H}.$$

For a two-layer ocean with a thermocline at 50M we obtain

$$\frac{\Delta\rho}{\rho} \approx 0.5 \, 10^{-3}.$$

29

The surface horizontal particle velocities must, on the other hand, be large enough. But we know they are directly related to the amplitude of the internal wave itself.

We therefore think that detection of internal waves by their surface manifestation should be favored by:

    a deep mixed layer (H),

    a sharp thermocline, and

    a density jump of the order of 1 / 40 H
        (H in meters)

3. Favorable Cases : an Assessment

Internal tidally generated waves on the continental shelf have frequency properties and amplitudes that cause them to fall into the stated favorable conditions. Those internal waves are generated most commonly in the highly stratified seasonal thermocline by interaction between a barotropic internal tide and bathymetric irregularities.

As a particular example, the continental shelf offshore France in the Bay of Biscay has strong tidal currents relative to a semidiurnal tide propagating northward. The day (20 August 1978) of passage of SEASAT over this area corresponds to a spring tide, and the bathythermographs show the strong stratification common to the summer season. A search of meteorological data has confirmed average summer conditions to have prevailed, with probable winds from the northeast. Previous conventional studies have shown that internal waves are frequently observed and propagate perpendicular to the NW/SE orientation of the continental slope.

30

E. COMBINED UTILIZATION OF CONVENTIONAL SENSORS

Adequate knowledge of wind conditions is necessary for the reliability of any SAR analysis. Ship observations, as well as data from other remote sensors (e.g., a scatterometer), were used in this study. (Both the scatterometer and SAR are side-looking sensors. Hence they offer generally overlapping coverage.) The required knowledge of the stratification and of the spectrum of periodic movements can be derived from bathythermographs, and from moored instrumentation measuring current and temperature time-series.

1. Bathythermographs

One bathythermographic or bathycelerimetric measurement allows the computation of the eigenvalues solution to the internal wave generation problem [Baines 1982]. It is then possible to find the wavelength of internal waves from the spacing of wave-packets generated by tidal flow over topography.

If the repetition rate of the forcing "r" is known (tidal internal waves for instance) one can derive from the spacing between packets "d", the phase speed

$$c_p = d\, r \quad .$$

A bathythermograph in situ makes possible the computation of the main density gradient on the thermocline from

$$c_p^2 = g H \frac{\Delta\rho}{\rho} \quad .$$

Comparing observed and theoretical values of the phase speed, it is possible to infer the thermocline depth by

$$H = \frac{\lambda^2 r^2}{g}\, \frac{\rho}{\Delta\rho} \quad \diagup$$

31

and eventually, by combining this information with sea-
surface temperatures, the heat storage in the ocean
[Mollo-Christensen and Mascarenhas 1979].

2. Current and Temperature Observations

Time series of current and/or temperature measure-
ments at several depths make possible the vertical modal
analysis of the vertical and horizontal movements at a
point.

High resolution observations of the sea surface
temperature by airborne or spaceborne infrared radiometers
might detect horizontal gradients due to variations of the
surface thermal layer depth directly related to the
stretching effect of an internal wave field.
Quasi-simultaneous temperature transects, in the same way,
can resolve the space characteristics of an internal wave
field that can only be inferred from a fixed observation
station together with internal wave theory.

Spacecraft velocity
vector $v \sim$ 8 km/s

Synthetic aperture
length
$L \sim$ 16 km

D, real aperture, $\sim$ 12 m

θ = real beamwidth

ϕ' = effective angular
resolution

h, slant range, $\sim 10^6$ m

Nadir

r_a, azimuth resolution,
$\sim$ 6 m
$\cong$ one-half real aperture

From Spaceborne SAR for Oceanography [1981]
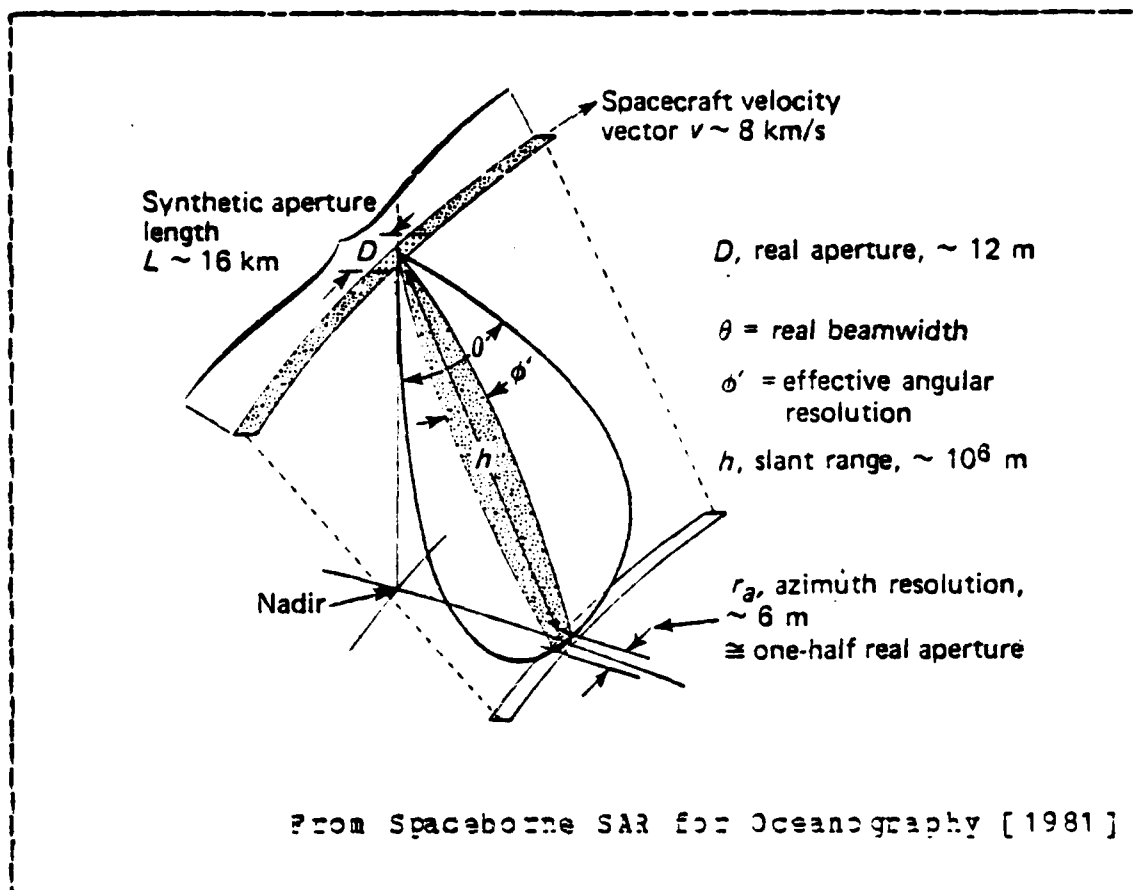
Figure 2.1   SEASAT SAR GEOMETRY.

For a moving target
Along track shift
due to
a Doppler effect
(time)
Line of flight
Correlation
direction
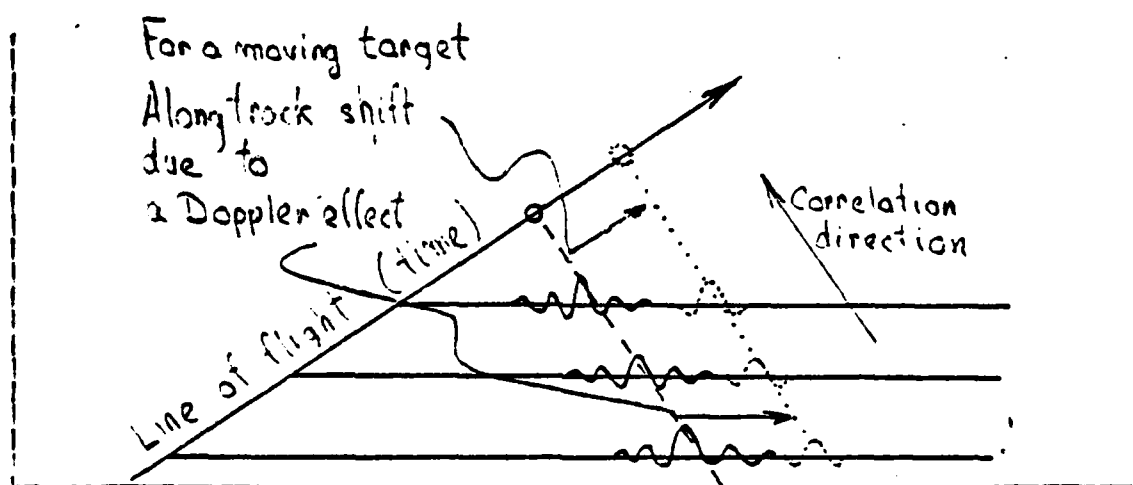
Figure 2.2   SYNTHETISATION OF AN ANTENNA.

33
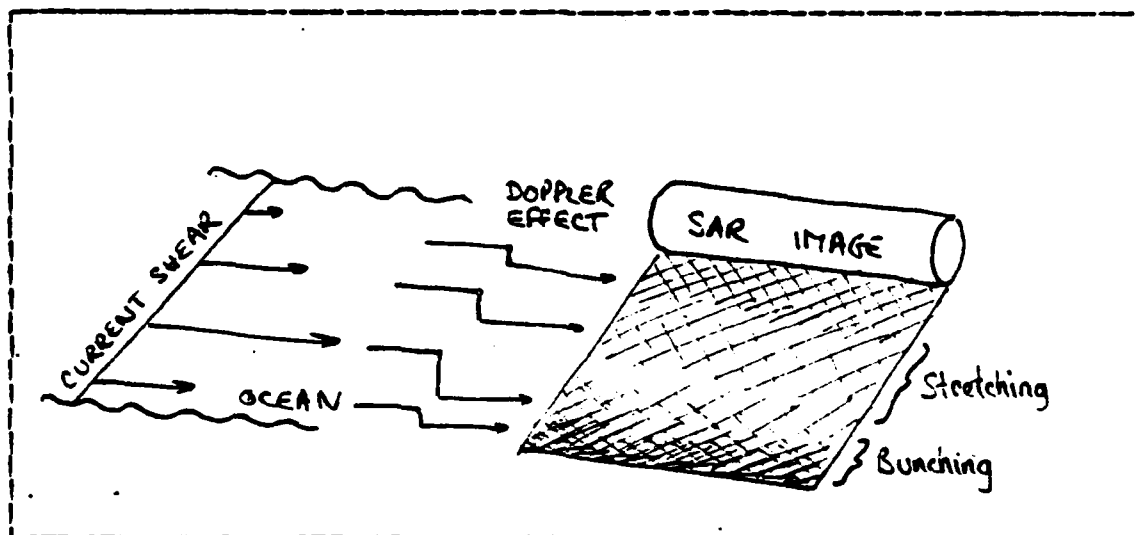
Figure 2.3   DOPPLER EFFECTS OF CURRENT SHEAR.

Dashed lines are isotachs
Small arrows indicate water movement.
"Cp" is the phase speed (propagation of the isotherms)
Black arrow points to surface rip.
White arrow points to surface damping.
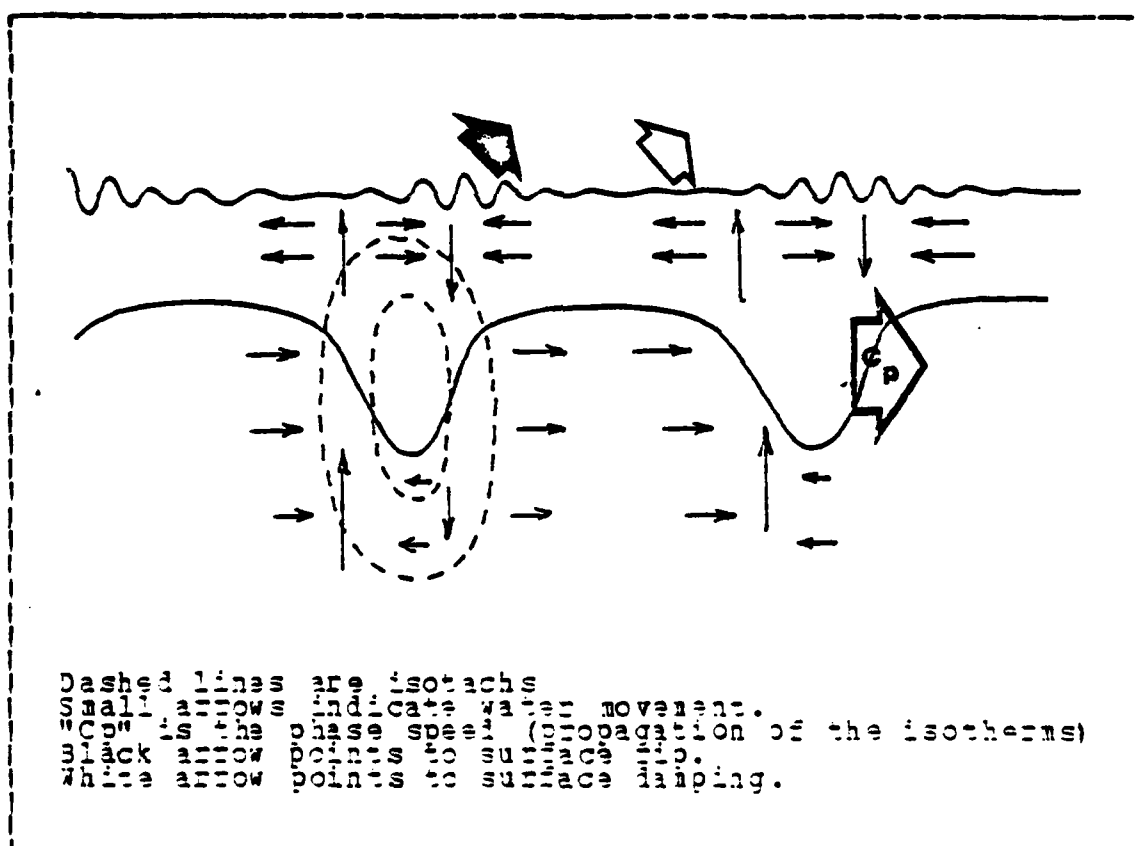
Figure 2.4   INTERACTION OF INTERNAL AND SURFACE WAVES.

34

III. GENERAL GEOPHYSICAL FEATURES OF THE BAY OF BISCAY

According to Sverdrup et al. [1942] "the terminal branches of the Gulf Stream system are not all well known; irregular branches which turn to the south terminate in great whirls off the European coast". These irregularities could correspond to semi-permanent circulation patterns or propagating eddies. Recent studies have been made of the mean circulation and of mesoscale features in the Bay of Biscay, particularly in the vicinity of the Armorican continental slope, from which some general conclusions can be drawn.

Several general geophysical features relevant to the subarea covered by the SAR image will be considered, giving particular emphasis to the summer climatological conditions under which the SAR image was taken.

A. ATMOSPHERIC CIRCULATION

Atmospheric conditions over the Bay of Biscay are determined by the location of the North Atlantic Subtropical High (pressure center) centered in February around 25ºN and in August around 35ºN. The High extends over 20 to 25 degrees of latitude in summer (vs. only 15 in winter) and is limited to the north by the Icelandic Low. The general atmospheric circulation is consequently a mean eastward flow, weak in summer, which is modified by the presence of the European continent and perturbed by the passage of fronts originated over the Nortwest Atlantic in the vicinity of the Polar Front (between 45ºand 50ºN in summer). Table II gives the statistical averages for August at three stations, respectively north, east, and southeast of the Bay of Biscay.

TABLE II

CLIMATOLOGY FOR AUGUST

Observations from 1946 to 1950			OUESSANT Ushant	BORDEAUX	SOCOA
Latitude................ Longitude.............. Height from sea level...			43°28'N 05°09'W 25 M	45°42'N 01°14'W 06 M	43°23'N 01°41'W 25 M
Sea Level Pressure at		1200GMT	1015.7	1016.8	1017.2
Temperature	(1) Mean	°C	16.5	20.2	19.6
	(2) Mean	Min °C	13.9	15.5	15.6
	(3) Mean	Max °C	19.1	24.9	23.7
	(4) Extreme	Min °C	7.4	6.6	7.2
	(5) Extreme	Max °C	29.0	39.0	38.2
Mean relative humidity		At 0600	94	85	88
		At 1200	84	67	73
Nebulosity	N<2/8	At 0600	11	33	19
	N<2/8	At 1200	16	27	24
	N>2/8	At 0600	47	35	50
	N>2/8	At 1200	39	23	39
Precipitation Fog	Mean Height(mm)		49	48	108
	(6) Number of days		12	11	12
	(7) Number of days		7	1	0
	Calm		4	2	5
	01 to 14 knots	N	11	10	10
		NE	13	11	7
		E	1	8	5
		SE	5	5	5
		S	8	3	10
		SW	11	7	13
		W	12	14	12
		NW	12	24	19
Frequency of observ. at 06 Z 12 Z 18 Z	15 to 31 knots	N	1	1	1
		NE	3	0	1
		E	"	"	0
		SE	2	1	0
		S	5	1	1
		SW	5	2	2
		W	3	5	7
		NW	3	5	2
	32 & more	N	0	"	"
		NE	"	"	"
		E	"	"	"
		SE	0	"	"
		S	0	"	0
		SW	1	"	0
		W	0	"	0
		NW	0	0	"

(1) (Daily MIN + Daily MAX)/2
(2) Mean of Daily MIN
(3) Mean of Daily MAX
(4) Lower Minimum
(5) Highest Maximum
(6) More than 0.1 MM
(7) Visibility < 1KM
(8)) means <.5% occurrence
" means 'no observation'

B. BATHYMETRY

The Bay of Biscay (Golfe de Gascogne) is a fairly large bay. It is 450KM (250NM) wide at its western opening on the West European Basin and extends 550KM (300 NM) to the southeast (Fig. 3.1). Its physiographic characteristics have been presented by Laughton [1975].

The abyssal plain has an average depth of 4500M, increasing southward to 4800M. It is limited to the south by the narrow (40KM) Cantabrian continental shelf, and to the north by a wide (200KM) and shallow (130M) shelf (Fig. 3.2). This latter shelf extends far beyond the Bay of Biscay to encompass the British Isles. The designation of Celtic Sea is generally given to the northern part of the shelf; the Armorican Continental Shelf is to the south of 48°N, the latitude of Brest.

The "La Chapelle Bank", at the above approximate limit (48°N, 007°W) is 100 to 150M deep and characterized by large scale and smooth ridges (amplitude ca. 40M) oriented NNE-SSW and 20KM apart. Its southwestard limit (47°41'N, 007°13'W), sometimes referred to as the bank per se, exhibits sand waves [Cartwright 1958], correlated with scattering layer undulations [Stride 1960] as a consequence of internal tidal wave activity [Carruthers 1963 and Cartwright 1963]. These sand-waves have an average height of 8M and a wavelength of 850M; they are oriented toward 110°T (parallel to the edge of the shelf) and extend over at least 20KM from the slope. Southeast of La Chapelle Bank, the continental seafloor has a variable geological nature (rocks, mud, gravel and sand), homogeneous in depth with a very gentle slope (0.05%).

The shelfbreak of the Armorican Shelf is oriented 130°T and occurs between 180 and 200M (Fig. 3.3) The width of the continental slope decreases from 35KM at La Chapelle Bank to 20KM at 47°N, 005°30'W, where the steepness is maximum (20%

37

between the 200 and 1000M isobaths). This steep slope is indented by many canyons and ridges normal to its axis. The designations given by Laughton [1975] will be used here. On the swath covered by the SAR image, five major canyons are visible: the Penmarc'h Canyon, the Guilvinec Canyon, the Odet Canyon, the Blavet Canyon and the Belle-Ile Canyon (Fig. 3.3).

The continental rise, south of the slope, is 200KM wide. It is broken by the Gascony Knoll at 45°20'N, 005°20'W, with a minimum depth of 3950M, at the eastern edge of the SAR image. The Cantabrian Knoll centered at 45°05'N, 008°00'W is steeper and higher (3000M minimum depth, 20 by 40KM horizontally), but it is 50KM off the western edge of the SAR image.

C. OCEAN CLIMATOLOGY

The surface circulation in the Northeastern Atlantic is not as well defined as that in the western (Gulf Stream) regime of the North Atlantic anticyclonic circulation. After crossing the mid-Atlantic ridge, the Gulf Stream loses its coherency and splits into several branches, which are weak and greatly variable on all space and time scales and which eventually decay into fields of poorly defined eddies (Fig. 3.4). The easternmost of these branches flows south along the European coast, probably creating a weak cyclonic circulation in the Bay of Biscay, as it weakens along the north coast of Spain [Millet 1980]. A transient westward surface current in the northern part of the Bay follows long periods of eastward winds; it is referred to as the Rennel Current and described in the French "Instructions Nautiques" [SHOM 1975] as being probably narrow, but strong (0.5 to 0.7M/S).

The near-bottom circulation is highly variable, too. However, there is a quasi permanent cyclonic bottom circulation on the abyssal plain centered at 44°30'N, 004°30'W, which is driven by the eastward flow along the Iberian Peninsula. On the Armorican Shelf the mean bottom current drifts to the northwest from March to July, and then towards the southeast from August to November. The average current speed measured at 1M above the sea floor is 0.04M/S. [Camus 1971].

The intermediate waters in the abyssal plain of the Bay are under the influence of the Mediterranean outflow, which spreads north out of the Straits of Gibraltar. This intruding water mass is centered at a depth of about 1100M and its T-S characteristics, originally T=11.9, s=36.50°/oo, decrease by mixing to T=10, S=35.30°/oo in the greater part of the Bay of Biscay. Assuming a level of no-motion at 2000M, results from two separate hydrographic data sets (July 1963 and November 1967) exhibit the following characteristics of the Mediterranean Water circulation [Le Floch 1969]: a permanent cyclonic circulation occurs in the southwest portion of the Bay of Biscay, approximately centered at 44°30'N, 007°30'W on which is superimposed variable meanders and probable eddies; the speed of this circulation is of the order of 0.05M/S.

D. WATER MASSES, FRONTAL STRUCTURES, AND EDDIES

Hydrographically, the deep ocean waters of the Bay of Biscay have three main components; the relatively warm surface waters are from the North Atlantic anticyclonic gyre; the deep and bottom waters are derived from Antarctic Bottom and Intermediate Water; the midcolumn water mass characteristics vary with the degree of mixing of Mediterranean Waters with either one of the first two

39

components. On the Armorican Shelf a mass of colder, less saline water occurs as a bottom layer adjacent to the French coast (Fig. 3.5).

We will consider as a front, the locus of sharp horizontal gradients in temperature or salinity at an arbitrary depth. Two main surface fronts are driven by tidal currents, one offshore Britanny due to a horizontal decrease in mixing, and the other at the continental slope which will be discussed in more detail. Two pelagic fronts have been identified : (1) the thermalhaline front delimiting the extension of Mediterranean Waters, which is difficult to monitor but which may have important acoustical effects, and (2) the thermal front bounding the coastal bottom cold water mass of the Armorican Shelf, which is enhanced in summer by surface heating, but which has no surface temperature manifestation in that season.

Eddies occur in the Bay of Biscay in summer conditions, when the thermal structure of the upper water column is strongly developed. Based on infrared satellite images of eddies bordering the Ushant frontal zone, these eddies are most apparent along geostrophically balanced fronts where cross frontal mixing takes the form of cyclonic disturbances [Pingree 1978]. They have a length scale of 20 to 40 KM, with a time scale of a few days and translational velocity less than 2CM/S. In the case of the Armorican shelfbreak, irregular eddies form on each side of the 200M isobath; in this process "the cooler water sinks below the warmer water and is stretched vertically" [Pingree 1978].

Over the abyssal plain, less apparent eddies have been detected by drifting-buoy experiments and by satellite imagery (Diskson 1981). These eddies, both anticyclonic and cyclonic, seem to partly decouple salinity and temperature features from density surfaces. From an AVHRR image taken on 14 May 1979, and in the vicinity of the SAR image, it

appears that cyclonic eddies were aligned on the continental rise east of 006°W, and that a pair of cyclonic and anticyclonic eddies was located, respectively, northwest and southeast of 45°30'N, 007°30'W. The length scale of these deep-water eddies is 50 to 100KM [Dickson 1981].

E. TIDES

"The tides of the Atlantic Ocean can be considered as composed of two parts, a co-oscillating tide which is maintained by the tide of the Antarctic Ocean, and a free tide which is maintained by the direct effect of the tide producing forces. As a result, the semidiurnal tide can be considered as composed of two standing oscillations having a phase difference of one quarter of three lunar hours." [Sverdrup 1942] The amphidromic point is "estimated reliably" [Cartwright 1980] at 50°N, 039°W, so that the tide will propagate from south to north in the Bay of Biscay with a 90 degrees Greenwich phase lag in the south versus 110 in the north (Fig. 3.6). The tidal amplitudes increase from 1.0M offshore, to 1.2M over the continental rise and 1.4M at 50KM off the French coast. By way of comparison, the diurnal tidal amplitudes over the area are of the order of 0.07M (Table III). The tidal energy dissipation computed by Cartwright [1980] largly exceeds direct estimates based on bottom friction, leading him to conclude that "a substantial loss must occur along the Biscay shelf south of Ouessant (Ushant Island)." And indeed, Pingree [1982] infers from both observations and nonlinear tidal models that "about 60% of the tidal energy flux onto the shelf occurs in the regions where the tidal streams reach about 40CM/S (ca. 005°30'W to 008°30'W)". Furthermore, he notes that "the shelfbreak bathymetric contours tend to increase this tidal strength wherever they are concave (canyons)".

TABLE III
TIDAL CONSTITUENTS

Constituent	Q1	O1	P1	K1	N2	M2	S2	K2
	47°45N		007°14W		depth	171M		
Amplitude	2.0	6.8	2.4	7.1	28.0	129.6	44.8	12.8
Phase	283	327	061	074	082	103	136	133
	47°27N		008 26W		depth	2158M		
Amplitude	2.1	7.5	2.7	7.9	25.8	122.9	42.0	12.1
Phase	283	328	063	076	081	102	134	131
Greenwich phase lag in degrees. Tidal amplitudes in CM.								

Internal tidal modes have been studied from current meter observations at 47°47N 010°13'W in April 1978, [James 1982]. Results support the notion that internal tides are dominated by the lowest vertical modes and that the M2 component is significantly coherent with the equilibrium tide. Barotropic tidal current ellipses were found to be narrow and directed perpendicular to the shelf, thus "forcing the isopycnal surfaces over topographic features (the accepted explanation for the generation of internal tides)" [James 1982]. They show a regular turning (counterclockwise) of their orientation axis from 570 to 3670M depth and could thus produce baroclinic activity. The tidal ellipses are themselves of clockwise rotation at depths less than 1270M.

F. INTERNAL WAVE MOTIONS

Internal waves are a common phenomenon in the stratified ocean and exist in the frequency band from the local inertial frequency (16.4H period at 48°N) to the maximum Brunt-Vaisala frequency. At tidal frequencies (e.g. such as, semidiurnal), these periodic motions should be called

internal (baroclinic) tides as they result from forcing by tidal forces. At frequencies greater than the Brunt-Vaisala frequency, perturbations cannot propagate as waves and are turbulent.

In the center of the Bay of Biscay, temperature time series [Hecht and Hughes, 1971] have shown that semidiurnal internal tides are greatly enhanced by spring (barotropic) tides and can generate high frequency oscillations with marked peaks at periods of T=71 and 24MIN. These deep-water internal tides could be generated by the incidence of the barotropic tide on the continental shelf, to then propagate offshore normal to the coast line [Rattray 1960]. Their amplitudes would then be given by:

$$\frac{A}{H} \approx \left(\frac{1}{d} - \frac{1}{D}\right) hqW \left(\frac{D}{D-h}\right)^{1/2} \cos\left\{qW\left(\frac{d}{d-h}\right)^{1/2}\right\} ,$$

where

$$q^2 = \frac{n^2 - f^2}{gh \frac{\Delta \rho}{\rho}}$$

and "A" is the amplitude of the internal wave, "2H" is the tidal range, "h" is the depth to the thermocline, "D" is the deep-water depth, "d" is the depth of the shelf (assumed constant), "W" is the width of the continental shelf, "n" is the frequency of the internal wave, "f" is the Coriolis parameter, "g" is the acceleration due to gravity, and "$\frac{\Delta \rho}{\rho}$" is the relative density difference between the two layers. Hecht's [1971] observed amplitudes exceed those estimated by the above formula (23M observed vs. 15.8M computed at spring tide). On the continental shelf (46°N 003°50W), nearbottom current records occasionally exhibit bursts of periodic oscillations (ca. 30MIN) followed during a few hours by apparent white noise fluctuations [Le Floch 1969].

Bathymetry
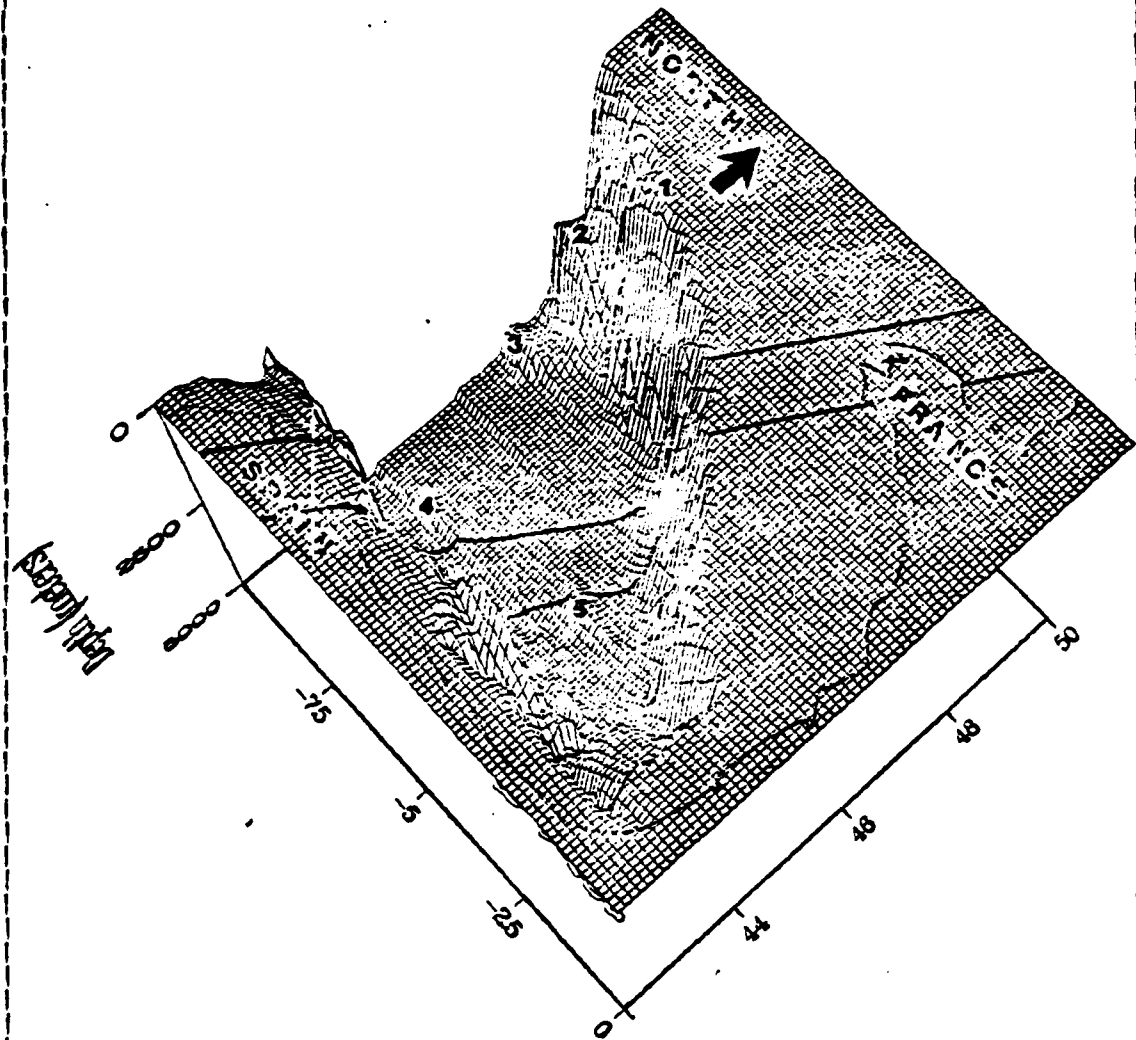
Three-dimensional view from the southeast.
Dashed lines are limits of the SAR image.
Longitude values are degrees west of Greenwich.
1-La Chapelle Bank 2-Meriadzek Terrace
3-Trevelyan escarpment 4-Cantabria Knoll 5-Gascony Knoll

Figure 3.1   TOPOGRAPHY OF THE BAY OF BISCAY.

44

Isobaths are in fathoms (1.83M) with intervals of 100
(500 between heavy lines).

[from Laughton 1975]
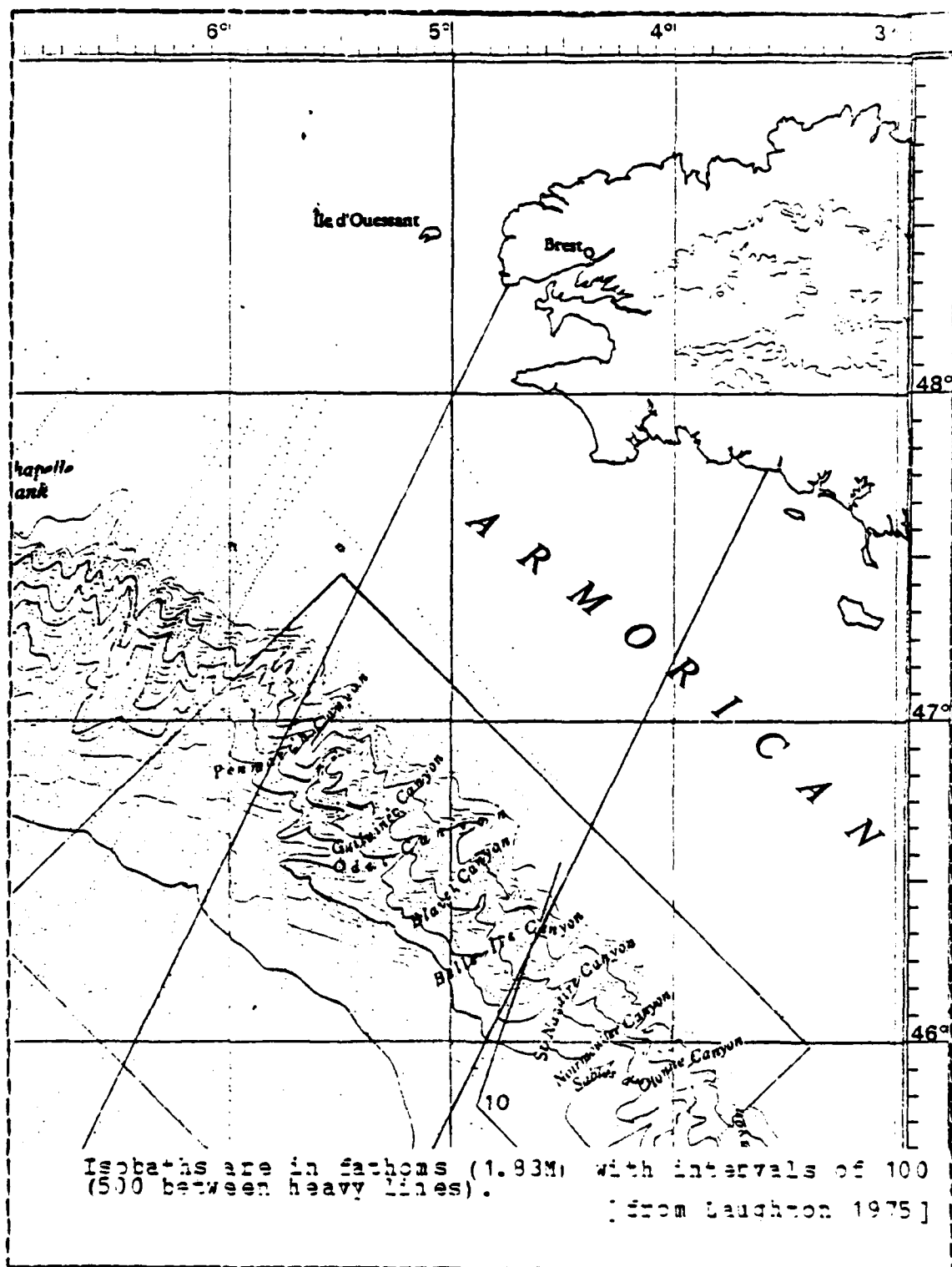
Figure 3.2   BATHYMETRY OF THE BAY OF BISCAY (SHELF).

45
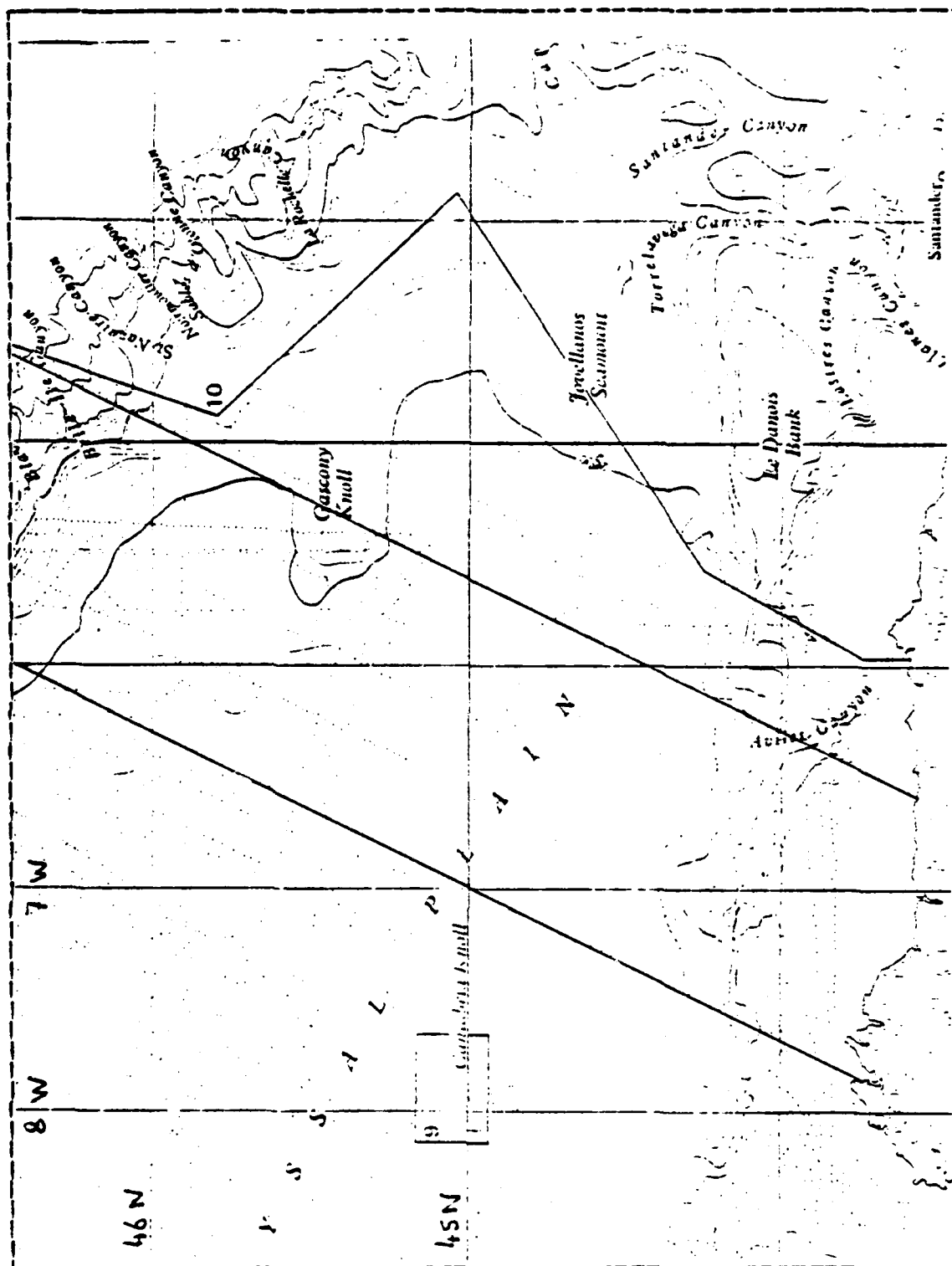
Figure 3.3   BATHYMETRY OF THE BAY OF BISCAY (OPEN SEA).

1- Region of frequent upwelling   [Dickson 1980]
2- Tidally mixed thermal front   [Raillard 1976]
3- Cold bottom water mass   [Le Floch 1978]
⬚ -AVHRR observations of eddies   [Pingree 1978-1979]
↷ -Deep and bottom circulation   [Le Floch 1969]
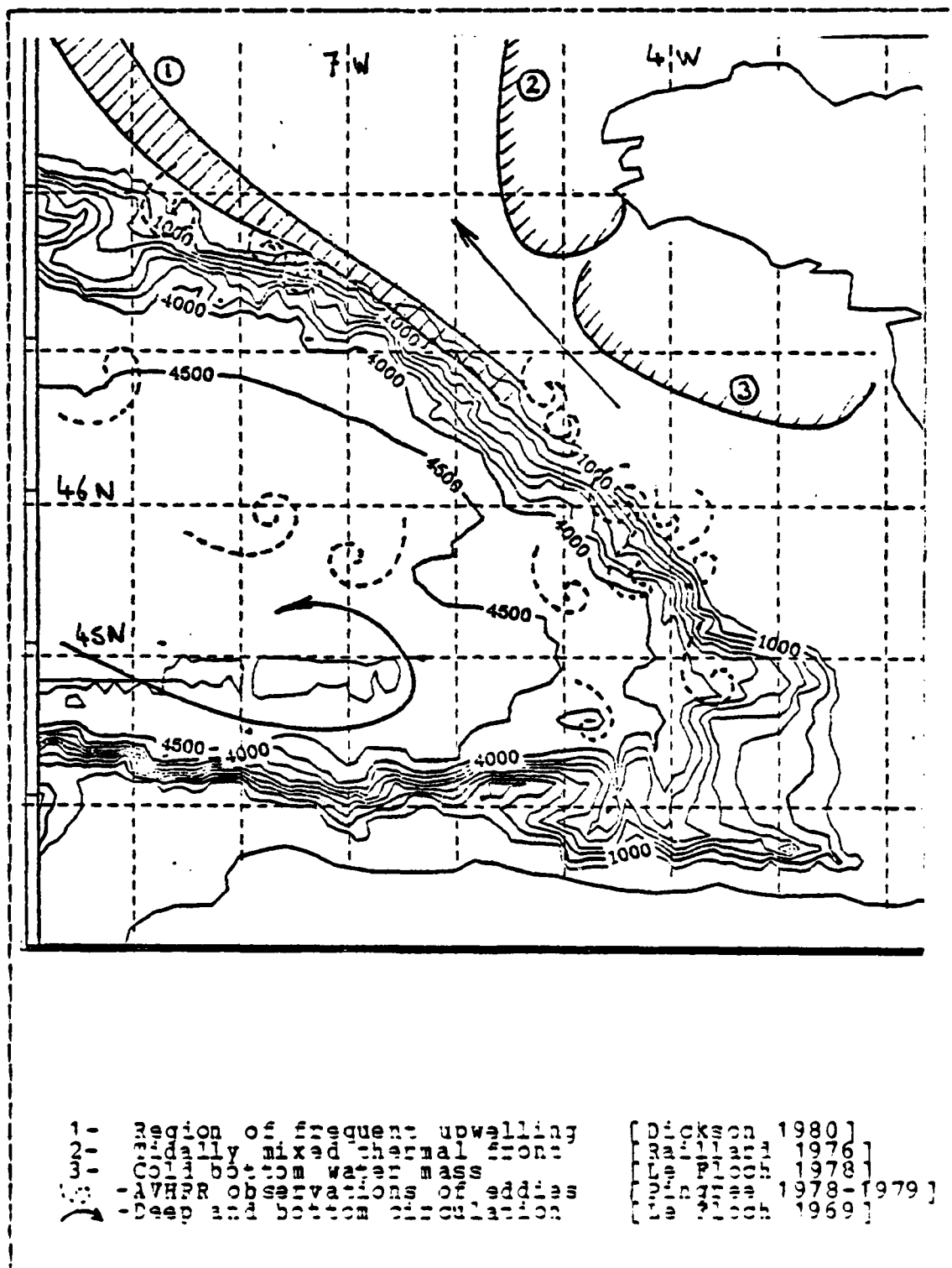
Figure 3.4   GENERAL OCEAN CIRCULATION.

Figure 3.5   T-S DIAGRAM.

48

Cophase(^{o}g) and coamplitude (M) lines for M2 tide.

Vertically integrated M2 tidal currents from a
numerical model

from Pingree [1981]

Figure 2.5   COTIDAL MAP.
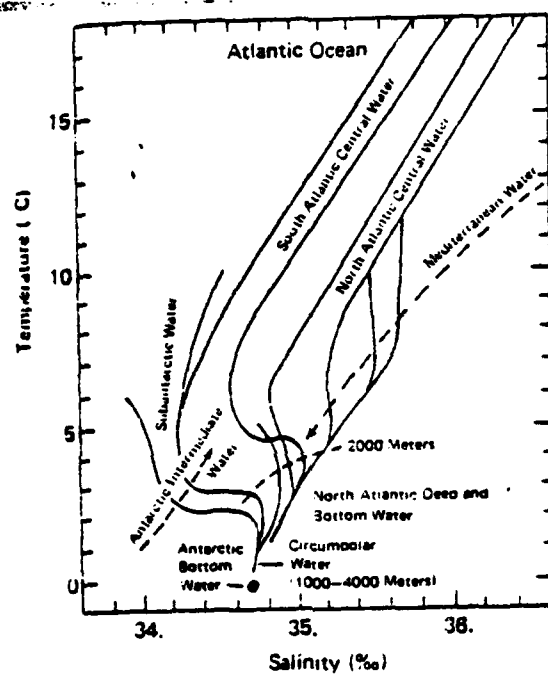
IV. GEOPHYSICAL SITUATION ON AUGUST 20 1978

A. METEOROLOGY AND WIND STRESS

On the 20th of August 1978, a high pressure ridge
extended from the Azores to Western Europe. The average
surface pressure over the Bay of Biscay was 1023MB (Fig.
4.1). A strong storm generated on the 15th of August
offshore Labrador was dying over Iceland (Fig. 4.3). A weak
cold front was 300NM west of the Bay of Biscay on the 19th
at 1200 GMT and probably underwent frontolysis in the area
of interest.

From ship reports, the evolution of the in-situ atmos-
pheric situation (ca. 47°N,005°W) can be analysed (Table
IV). Between 200300Z and 200600Z the cold front was present
near the location of observations at 46°40N, 004°30W.

TABLE IV
METEOROLOGICAL OBSERVATIONS ca.47N,005W

Day-Hour GMT	Surface pressure	Wind from Speed M/S	Dry air temp.°C	Moist air temp.°C	Clouds octants
191200	1018.2	250/5	21.0	18.5	4
191500					
191800					
192100	1018.0	250/4.5	20.2	18.8	5
200000	1020.0	200/3	18.5	17.5	0
200300	1019.0	270/2.5	17.4	17.0	7
200600	1020.0	000/5	18.5	17.0	8
200900					
201200	1022.0	030/6	19.5	17.2	6
201500	1023.0	000/2.5	18.7	16.1	5
201800	1022.0	000/6	18.2	16.0	2
202100	1021.0	010/7.5	17.3	16.1	3
210000	1021.0	010/7	17.5	15.4	4
210300					
210600	1023.0	040/5	17.5	17.5	2

From synoptic charts and these ship reports a comparison
can be made to select the SEASAT scatterometer winds at the
time of the SAR image (fig. 4.2). At 202142Z, a local high
pressure center was in the vicinity of 48°N, 010° W, thus
establishing an anticyclonic surface flow decreasing from
ca. 10M/S south of Penmarc'h (north of the SAR image) to
ca. 5 M/S at 45°N 006°W (south of the SAR image). The best
estimate for the direction is a flow towards 200°T (winds
north-northeast).

B. SWELL

A heavy (mean significant wave height of 2.5M), and long
(mean wavelength of 230M) swell had originated 2000KM away
(Fig. 4.4) and was currently prevailing over the sea state.
It was propagating roughly 130°T (from shipboard meteorolo-
gical reports). The generation areas were estimated by
atmospheric charts (Fig. 4.3) to be in the southwest quad-
rant of the surface pressure low. Distances and time of
propagation with respect to the SAR image location and time
yielded estimates of the wavelengths that could be expected
in the Bay of Biscay, August 20, as a function of mean
direction. The deep water surface gravity waves equations
used are the following:

the period is expressed as $\quad T = \sqrt{\dfrac{2\pi\lambda}{g}}$

the group speed is given by $\quad C_g = \dfrac{1}{2}\sqrt{\dfrac{g\lambda}{2\pi}}$

thus yielding $\quad \lambda = \dfrac{8\pi}{g}\dfrac{D^2}{\tau^2}$

with "D", distance from the generation area and "τ", time
elapsed since the original wind generation.

No swell spectra were available to compare with the
patterns visible on the SAR image, but a correlation with
significant wave heights as measured by the altimeter of
SEASAT was possible. The most interesting feature in the

51

altimeter pass of 210721Z (ascending node passing by 46°N, 005°W) was a sudden increase in significant wave height from an average of 2M to more than 4M over a short distance (15KM) at position 47°15'N, 006°00'W (Fig. 4.5), i.e. near the shelfbreak. This astonishingly abrupt variation could hardly be related to any atmospheric mesoscale process. It will be shown (Cf VI-E) that it may be the consequence of a strong interaction with current shear occurring at the shelfbreak. According to sailors experienced with this area [Chiari 1982], crossing the 200M isobath is often accompanied by a characteristic change in sea-state. An historical reference is given by Le Danois [1948], who attributes the denomination of La Chapelle Bank to an observation made by the "Sieur de La Chapelle" in 1695 of surface turbulence wrongly associated with extreme shoaling. This apparent shoal was resighted in 1764 and a rock was marked on the charts for the following decades. A well known example of such a current-swell interaction is the occurrence of "giant" waves [Huthnance 1980] near the shelf edge off the East coast of South Africa. These are thought to arise at a caustic associated with the refraction of surface waves by the Agulhas Current. In the same way, an alongshore current at the shelfbreak in the Celtic shelf could explain the increase in wave height observed there.

C. MEAN AND TIDAL CURRENTS

Data available for direct estimation of the mean current and its variations over the area, are provided by the deep water subsurface mooring at 46°57'N, 009°57'1W with current meters at 1524, 3032 and 3976M (350KM off the SAR ground track and 180KM offshore of the shelfbreak) (Cf 1-B). Low frequency currents at the three levels do not exhibit any obvious correlation and vary over all directions with a

52

time-scale of three months.   The mean currents in the last
10 days before the 20th of August are respectively:

at 1524M toward 010°T at 0.06M/S

at 3032M toward 270°T at 0.004M/S

(veering 330°T in last 3 days)

at 3976M toward 315°T at 0.001M/S

On a shorter time scale, progressive vector diagrams show a
semidiurnal periodicity at each of the three levels (Fig.
4.6): the mean speeds are :

at 1524M 0.08M/S

at 3032M 0.05M/S

at 3976M 0.0015M/S

At 20 21 40, time of the SEASAT passage, the instantaneous
current vectors were :

at 1524M toward 315°T at 0.08M/S

at 3032M toward 185°T at 0.06M/S

at 3976M toward 270°T at 0.0015M/S

The passage of SEASAT on 20 August followed a spring tide
ranging 110 on the French coefficient scale [SHOM 1968]
(i.e., amplitudes 15% greater than the average spring tides
of coefficient 95).   At the time of the image, the surface
tide at the shelfbreak was at high tide plus four and a half
hours (Table V).   The surface currents were estimated
towards 230 °T at 0.85M/S (Table 4.5), [SHOM 1968].

D.   SPATIAL THERMAL STRUCTURE

The thermal structure over the area was established from
a set of 69 XBT'S (Cf 1-B).   The time span of this tempera-
ture sampling was from 0900 17 August to 0500 24 August.
The spatial limits are between 43° and 48°North, and 10°
West and the coastline.   The distribution of this sampling
is conveniently centered around the radar image, in partic-
ular in the vicinity of the continental slope and with a

53

TABLE V
COEFFICIENTS AND TIMES OF HIGH TIDES

Days of August	In BREST GMT Hour	At Shelf break	Coeff	Amplitude in Brest	Amplitude at Break
15	00 33	00 13	60	1.93M	1.25M
	13 09	12 49	65	2.12	1.38
16	01 42	01 22	73	2.34	1.52
	14 12	13 52	30	2.57	1.67
17	02 40	02 20	87	2.79	1.81
	15 06	14 46	94	3.04	1.97
18	03 32	03 12	100	3.20	2.08
	15 56	15 36	104	3.33	2.16
19	04 19	03 59	103	3.46	2.25
	16 42	16 22	110	3.50	2.28
20	05 05	04 45	110	3.50	2.29
	17 26	17 06	109	3.48	2.26
SAR image: at 2142Z and at the shelfbreak High Tide +4.5H					
21	05 47	05 27	105	3.41	2.21
	18 08	17 48	102	3.26	2.11
22	06 28	06 08	97	3.12	2.02
	18 49	18 29	90	2.90	1.88
23	07 09	06 49	83	2.60	1.69
	19 30	19 10	76	2.45	1.59

maximum density on the eastern half of the ground coverage, as shown by a plot of the spatial-temporal distribution (Fig. 4.7) with respect to the distance from the shelfbreak (y-coordinate defined in 1-C and Fig. 1.1).

1. Analysis of the Mean

A smoothed transect was established by averaging along the x-axis with a "y" step increment of 20KM (Fig. 4.8). The isotherms generally sloped down from the shelf region to the open sea (on the average 10M over 100KM). A marked mixing was apparent in the region of the shelfbreak (-10<Y<10) with shoaling of the isothermal layers above the thermocline (14°C) and sinking below it. Dynamic heights relative to the smoothed transect yield a mean surface geostrophic flow relative to 150M of the order of .2M/S and about 20KM wide, towards the northwest at the shelfbreak.

TABLE VI

SURFACE TIDAL CURRENTS AT 47°24'N 006°05'W

Hour	Direction	Speeds M/S		
GMT	°T	Spring	Neap	AUGUST 20
04 45	....			High Tide
05 05	120	0.25	0.15	0.3
06 05	190	0.4	0.2	0.45
07 05	200	0.5	0.25	0.55
08 05	210	0.6	0.3	0.65
09 05	225	0.75	0.4	0.85
10 05	238	0.75	0.4	0.85
11 05	236	0.5	0.25	0.55
11 26	250	0.4	0.2	0.45
12 26	295	0.2	0.1	0.2
13 26	10	0.3	0.15	0.3
14 26	35	0.5	0.25	0.55
15 26	50	0.5	0.25	0.55
16 26	70	0.45	0.25	0.5
17 06	....			High Tide
17 26	120	0.25	0.15	0.3
18 26	190	0.4	0.2	0.45
19 26	200	0.5	0.25	0.55
20 26	210	0.6	0.3	0.65
21 26	225	0.75	0.4	0.85
SAR image	-- at 2142 -- towards 230° at 0.85 M/S			------
22 26	238	0.75	0.4	0.85
23 26	236	0.5	0.25	0.55
23 47	250	0.4	0.2	0.4

The geometric approximation of the shelf by a straight line in the averaging process, and probable variations in time and space of this mixing region, reduce the more dramatic features that can be seen in particular non-averaged transects. The mean vertical temperature profile is characterized by a mixed layer at 18°C limited by a sharp thermocline (on the average 0.2°C/M). On the shelf, a bottom mixed layer of 12°C was present.

Taking an arbitrary "level of no motion" at 150M, dynamic heights were computed for each XBT soundings and a horizontal smoothed contouring was made (Fig. 4.14). The surface geostrophic speeds corresponding to this analysis are cyclonic around a stretched ellipse with a major axis coinciding with the continental slope. Northwest currents on the upper part of the slope are of .5M/S at their

maximum, vs. a returning southeast flow of .2M/S over the rise.

A vertical modal analysis (Cf. VI-B), yields baroclinic internal Rossby radii of deformation of 4.5KM on the shelf and 25KM in the deep ocean. (Cf VI-B)

2. Analysis of the Variability

The spatial variability of the thermocline depth was computed using a subset of the total XBT data, which was selected to avoid unrepresentative (sparce and dispersed) values. The variance of the depth of a given isotherm was calculated in each rectangular bin of 10KM width. Standard deviations of the 13°C isotherm depth from the above means were computed (Fig. 4.9). The strong increase in the values at the position of the idealized shelf break could either mean a significant increase in the time variability (internal waves), or express the fact that the mixing is taking place over a very short distance compared with the width (10KM) of the bins used for averaging.

3. Selected Representative Transects

Some specific transects were then considered to give a quasi-instantaneous spatial image of this mixing process. One interesting subset of BT's was acquired by a transiting ship sailing towards Ouessant (Ushant Island) and whose track crossed the shelfbreak at 47°30N, 06°W on August 23. A sampling rate of one per hour (i.e. 30KM spacing) enables drawing a quasi-synoptic transect parallel to the SAR swath but 60KM west of it (Fig. 4.10). Other transects were made by selecting BT's close in time and conveniently spaced in the vicinity of a perpendicular to the isobaths. A set of three transects is depicted on a geographic grid (Fig. 4.11) with other non-synoptic transects reproduced from various sources (Fig. 4.12). The scaling adopted is identical for

56

all and based on the "along-track" distance from the shelf-
break. Common characteristics appear to be a narrow pelagic
front anchored on the sea-floor at the upper part of the
shelfbreak (ca. 180M depth), with one or two upwelling zones
adjacent to this narrow intermediate mixed layer. The ther-
mocline is stronger on the shelf than in deep waters (Fig.
4.13). In chapter VII, an idealized 3-layered ocean was
extrapolated from these selected transects and the corre-
sponding geostrophic currents were compared to the observed
circulation.

E. TEMPORAL THERMAL ANALYSIS

Daily averages of the isothermal depths (Fig. 4.15) show
a significant heating in the upper layers on 20 August and a
general broadening of the thermocline between 17 and 24
August. Assuming a propagation offshore from the shelf of
tidally generated waves, diagrams have been established
displaying for a given isotherm, variations of its depth as
a function of time and space (Fig. 4.16). These variations
in depth were obtained by subtracting the mean along the
x-direction to eliminate any permanent trend and enable a
contouring of relative values. The spatial axis is the
along-track (y-coordinate) distance from the shelfbreak; the
time axis in hours has been "folded over" two semidiurnal
(12.4H) periods. Hence all time coordinates are taken
within 24 hours by subtraction (or addition) to the actual
time of observation of an adequate multiple of the semidi-
urnal period.

No contouring algorithm could be applied to such sparse
and greatly contaminated data (by various phenomena: vari-
able wind stress, radiation heat exchange, even high
frequency nonlinear internal waves). A hand-contouring was
attempted under the following principles: one contour line

was drawn for a zero relative depth, another line followed
the maxima and the last one followed the minima. This was
done for three temperatures (12,14,16°C). Each of those
diagrams exhibits a constant pattern obliquely oriented on
the axis, and thus corresponding to a propagation of the
variations. The slope of those patterns (distance of propa-
gation during a given interval of time) was found to be
approximately 1.1M/S (equivalent to 0.9M/S perpendicular to
the shelfbreak). A modal analysis described in VI-B showed
that high frequency internal waves of period 90MIN would
have this same wave speed. Furthermore the phase of this
propagation implied a maximum deepening event at "Y=0" at
about 1900Z, 20 Aug. Conversely, at the time of the SAR
image the crests of these propagating oscillations were
found to be at Y=10 and Y=60. Maximum values of relative
depth excursions show general increasing values with depth:
a. For isotherm 12°C mean depth of 35M with 55M excursions
b. For isotherm 14°C mean depth of 45M with 15M excursions
c. For isotherm 16°C mean depth of 30M with 17M excursions

   At deeper depths, the NEADS mooring temperature data
allows estimation of the vertical isotherm movement by
relating semidiurnal temperature fluctuations at a given
depth to the climatological temperature profiles. Data from
the current meter pressure gauge showed that vertical oscil-
lations of the array itself were negligible.
At 1500M, temperature variations of .3°C in a mean gradient
of $8 \cdot 10^{-3}$ °C/M yield vertical amplitudes of about 20M.
At 3000M, temperature variations of .15°C in a mean gradient
of $2 \cdot 10^{-4}$ °C/M yield vertical amplitudes of more than 40M.
At 3500M, temperature variations are at the limit of
discrimination of the thermal gauge but reveal vertical
movements of at least 20M.

P. SUMMARY

SEASAT flew over the shelfbreak of the Bay of Biscay at 2142Z (after sunset) on 20 August 1978. A high pressure cell had dominated the area since early in the morning, bringing a southward wind of 6M/S. The cloud cover gradually decreased, and the air temperature decreased to 17°C.

A well established swell was entering the Bay from the northwest, nearly tangential to the isobaths in the vicinity of the shelfbreak where a significant increase in wave heights was observed from the SEASAT altimeter.

The tide was a spring tide at high level plus 5 hours at the shelfbreak. The ebbing surface current on the shelf side was at its maximum toward 240°T at 0.85M/S.

The ocean was strongly stratified with sea surface temperatures of 18°C, a thermocline gradient of 0.3°C/M at an average depth of 30M, and a bottom tidally mixed layer on the shelf of 12°C. The first mode internal Rossby radii of deformation were of 4.5KM on the shelf and of 25KM in deep water.

A spatial thermal analysis showed a marked front at the shelf break with intense mixing and upwelling. There was a westward surface geostrophic jet at the shelfbreak.

A temporal thermal analysis gave some evidence of an internal semi-diurnal "disturbance" propagating offshore from the break with a speed of 0.9M/S and with the last crest in the vicinity of "Y=10" at the time of the SAR image. This propagation speed being significantly smaller than the computed phase speed of the internal first modes tides (3.8 and 1.7M/S), either some higher modes are present or high frequency waves are generated by the tide but eventually decoupled from it and trapped in the vicinity of the thermocline (where the largest Brunt-Vaisala frequencies can be found).

Analysis 1200Z 20 Aug 1978

Figure 4.1   SURFACE ATMOSPHERIC PRESSURE CHART.

"Chickentracks" map was accessed on-line from PODS
(Pilot Ocean Data System)
Data time: 730820214055-730820214209
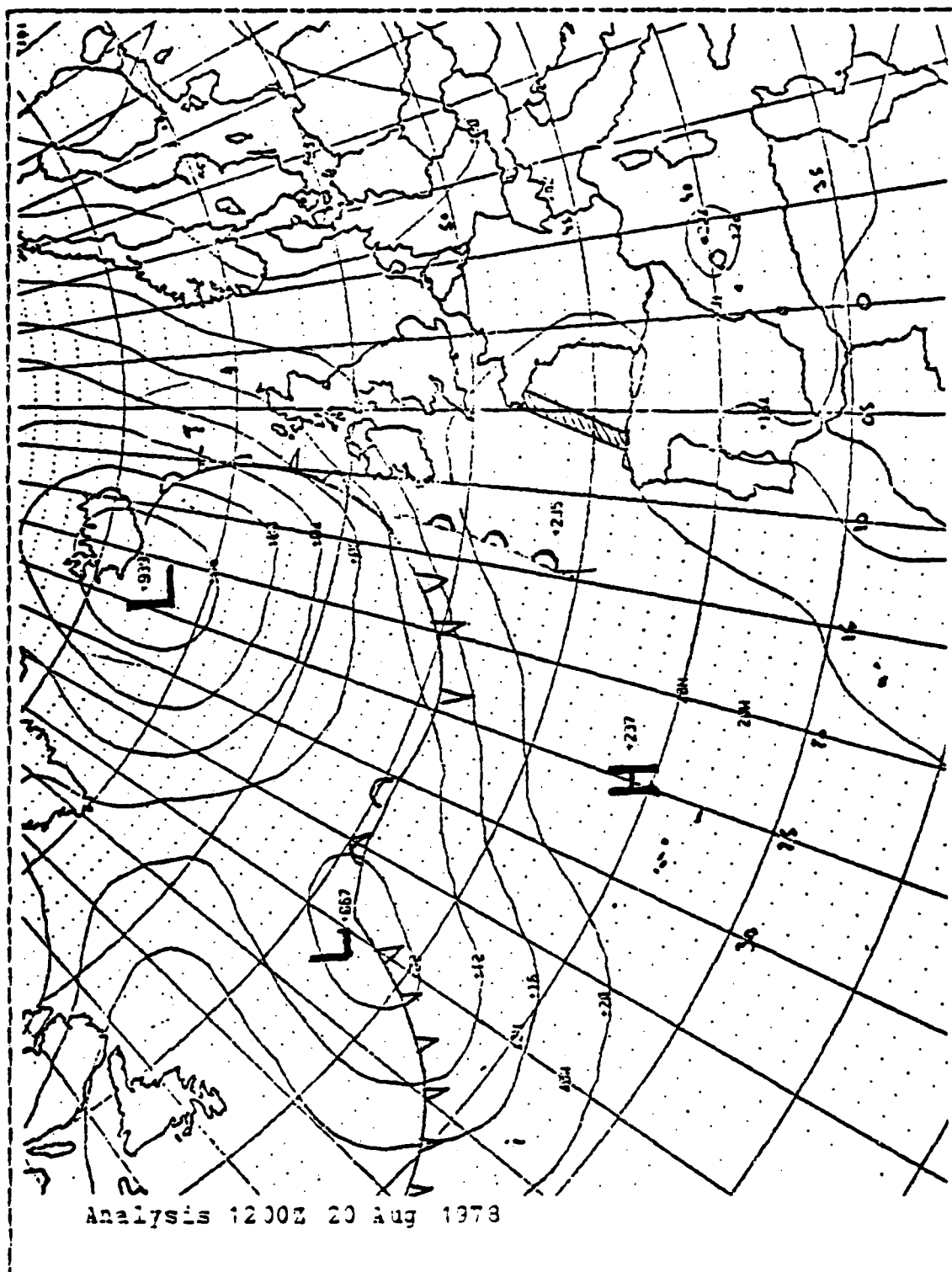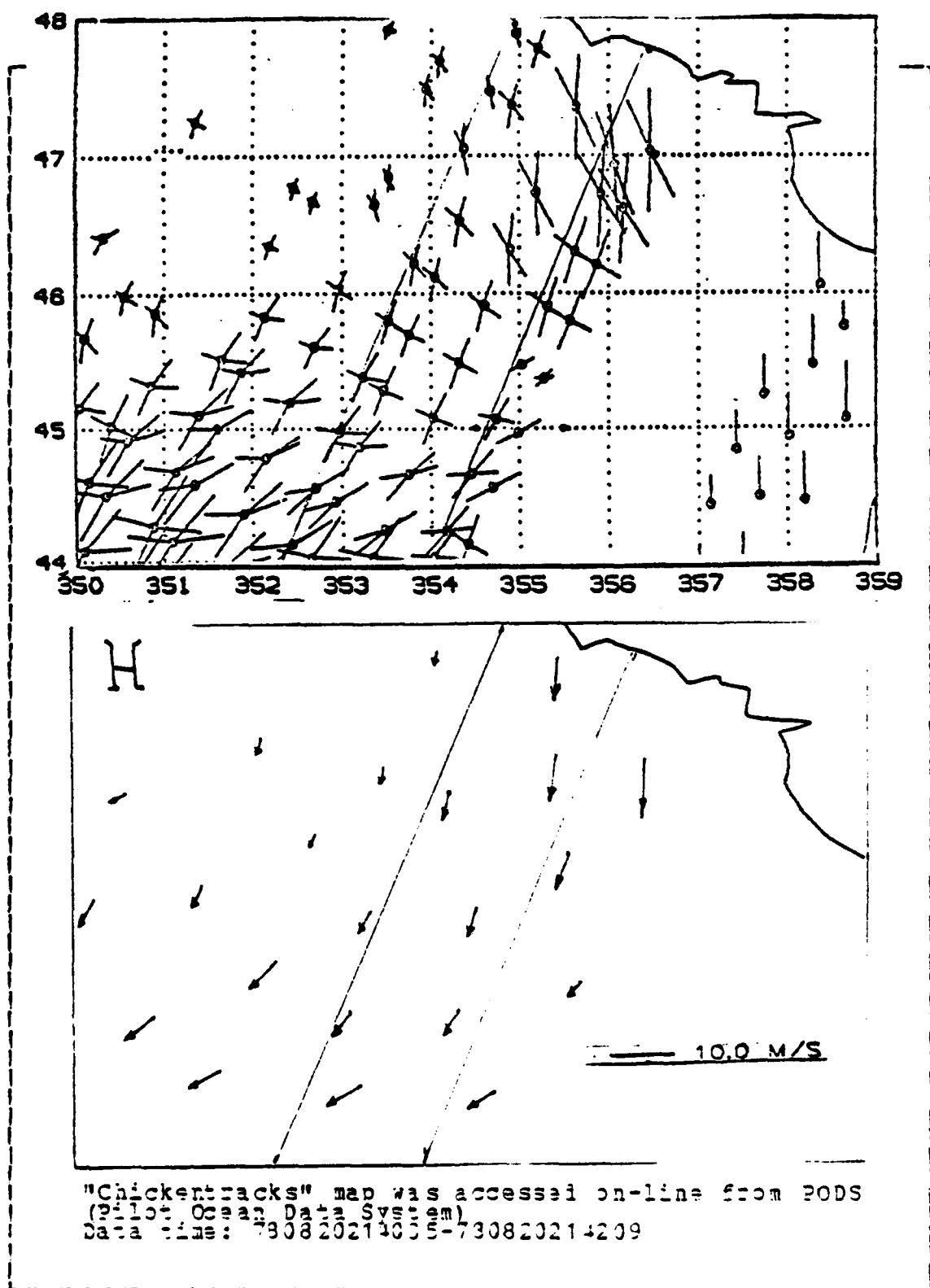
Figure 4.2   SCATTEROMETER WINDS.

61
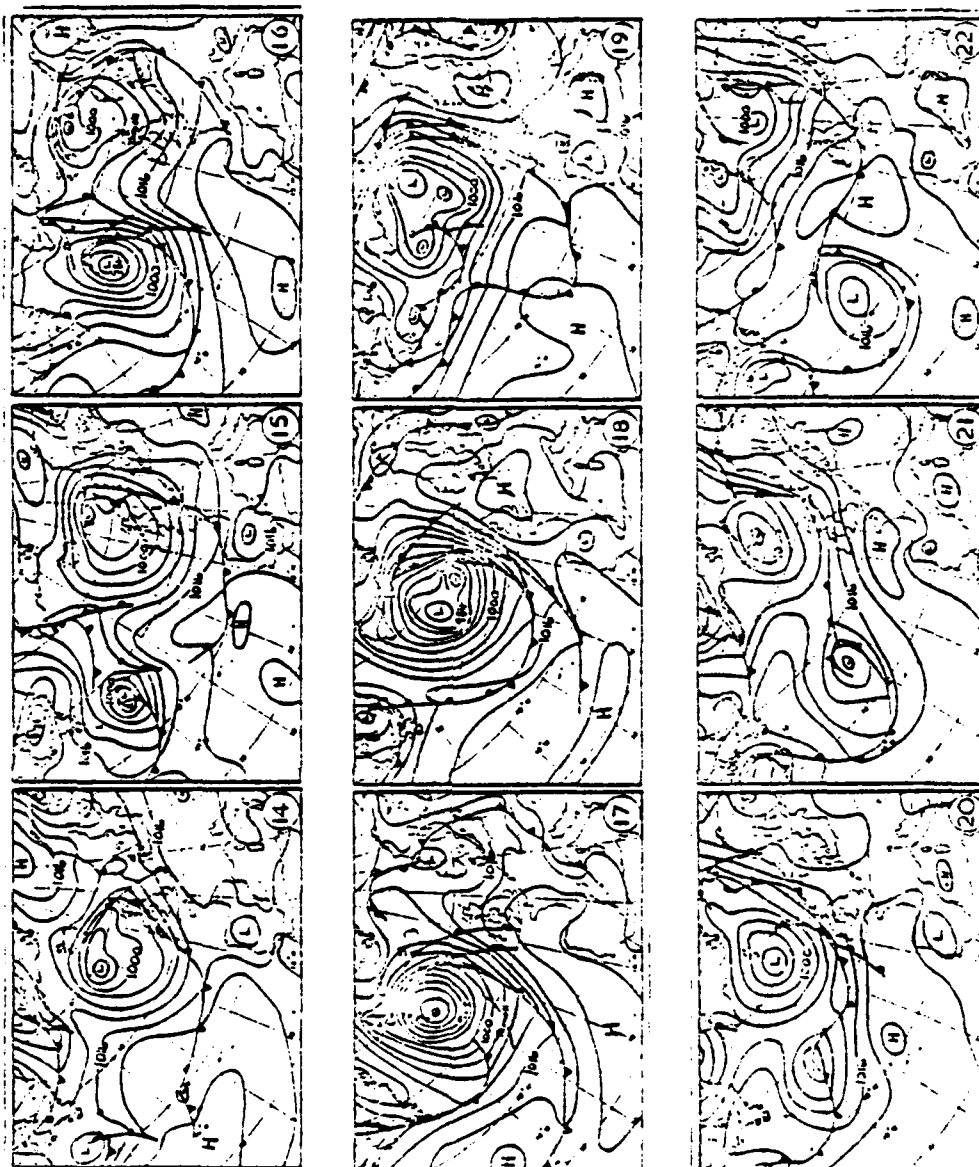
Dates of August at 1200 GMT
Mean sea level isobars are drawn at 4mb intervals

From "Weather", Royal Meteorological Society

Figure 4.3   DAILY SYNOPTIC WEATHER CHARTS.
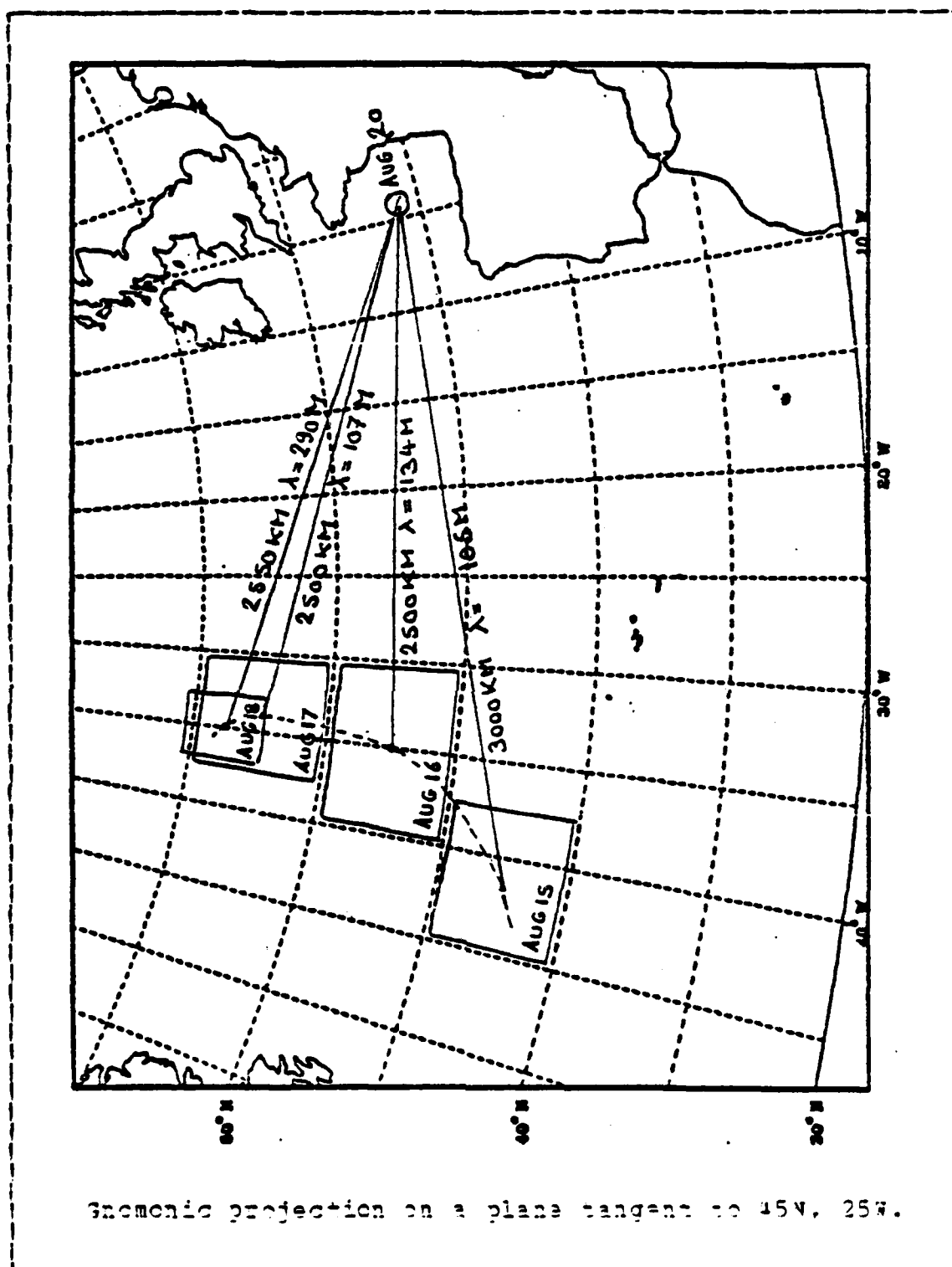
Figure 4.4   PROPAGATION OF THE SWELL.
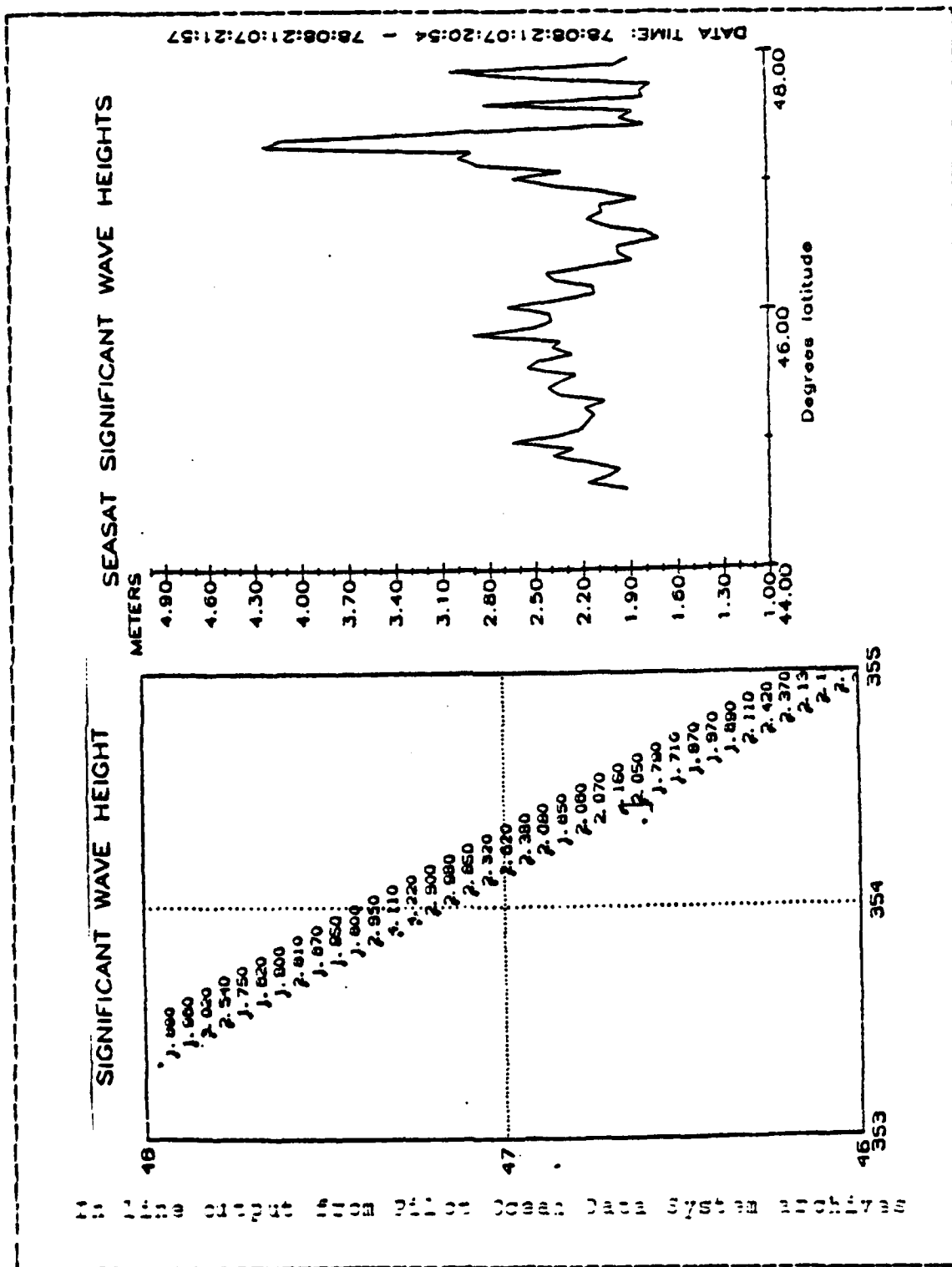
Figure 4.5   SIGNIFICANT WAVE HEIGHTS.
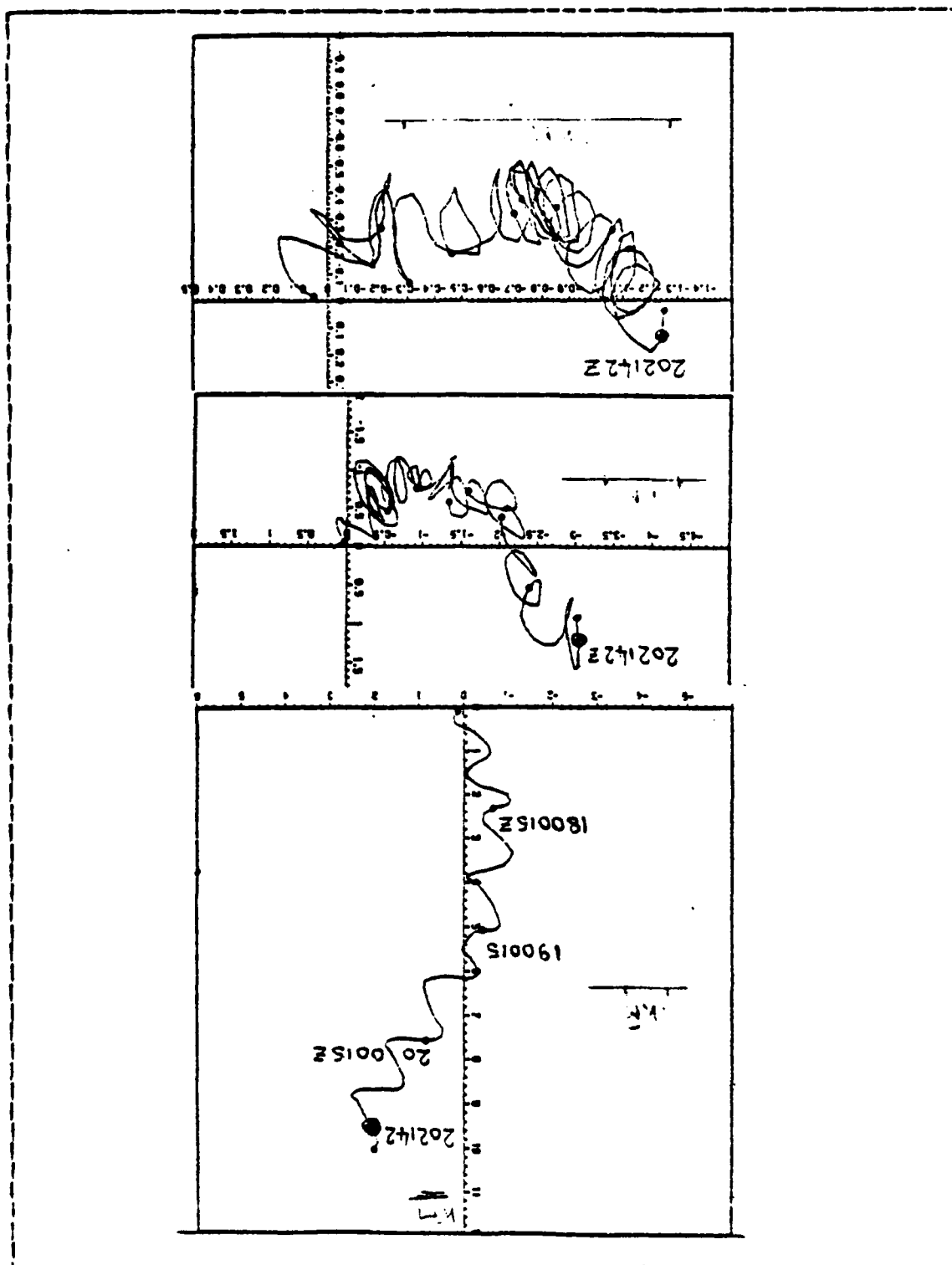
Figure 4.6   PROGRESSIVE CURRENT VECTOR DIAGRAMS.
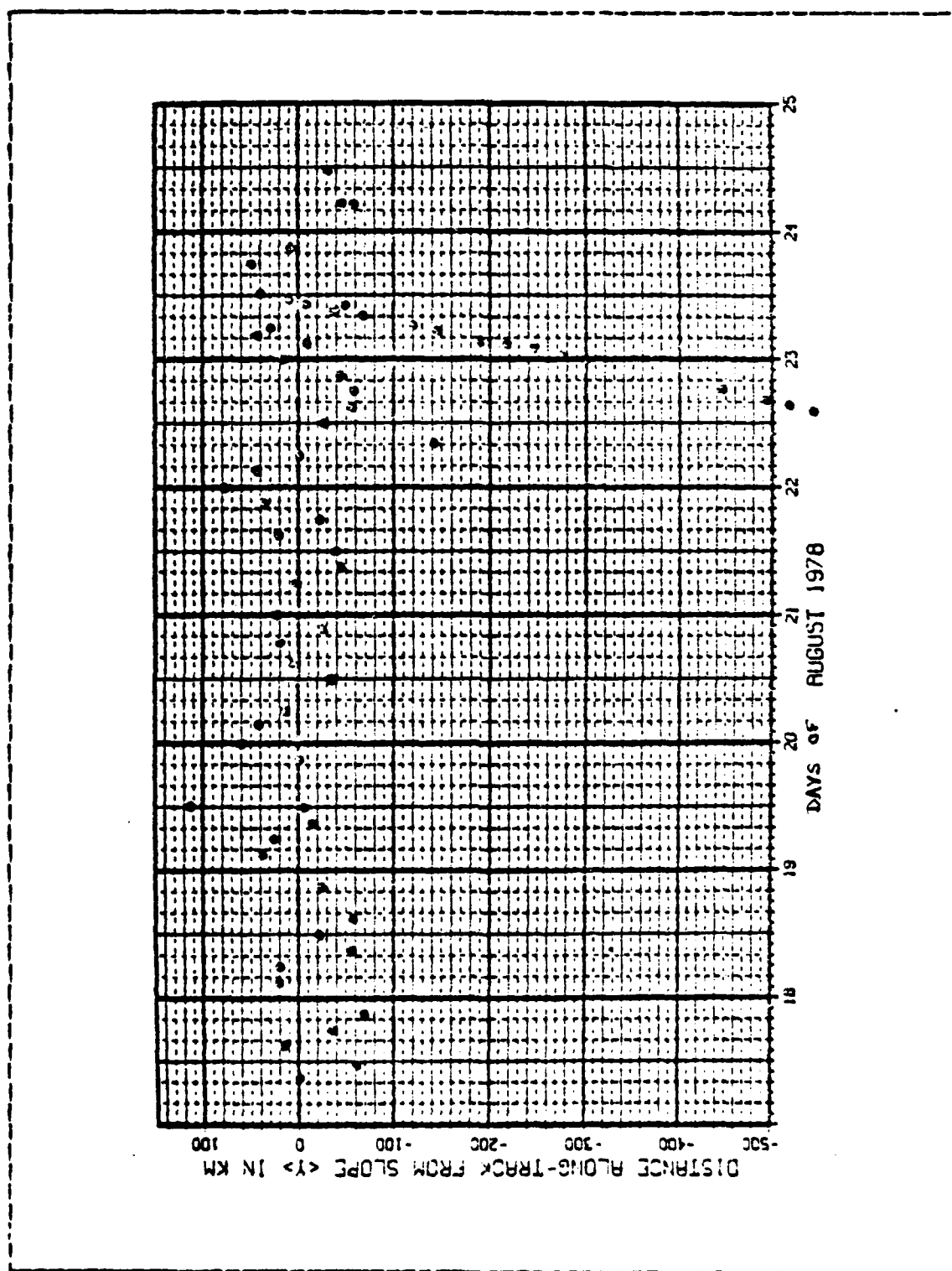
Figure 4.7   DISTRIBUTION OF BT SAMPLINGS IN TIME AND SPACE.

66
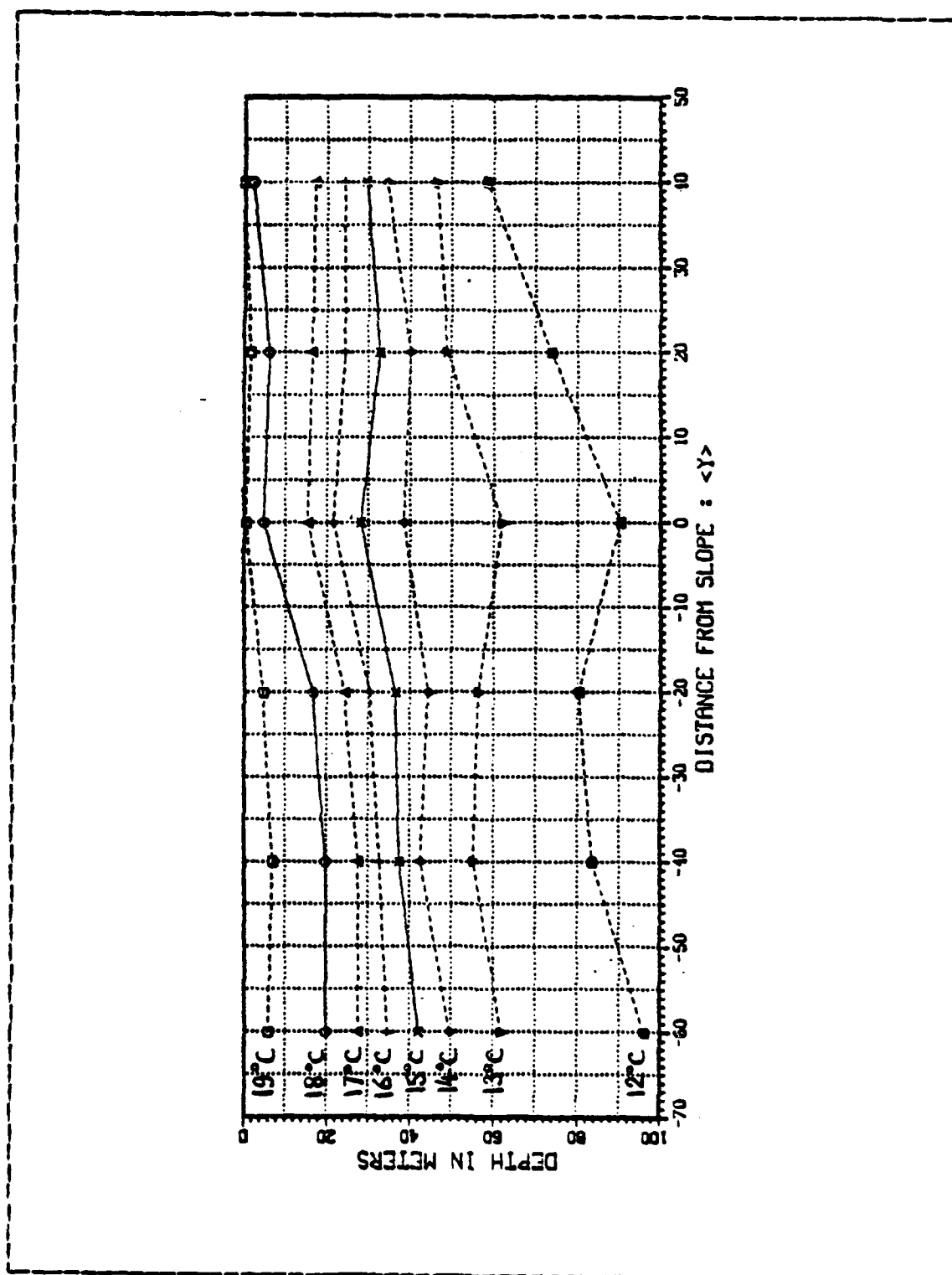
Figure 4.3   ALONG TRACK AVERAGE OF ISOTHERMS.
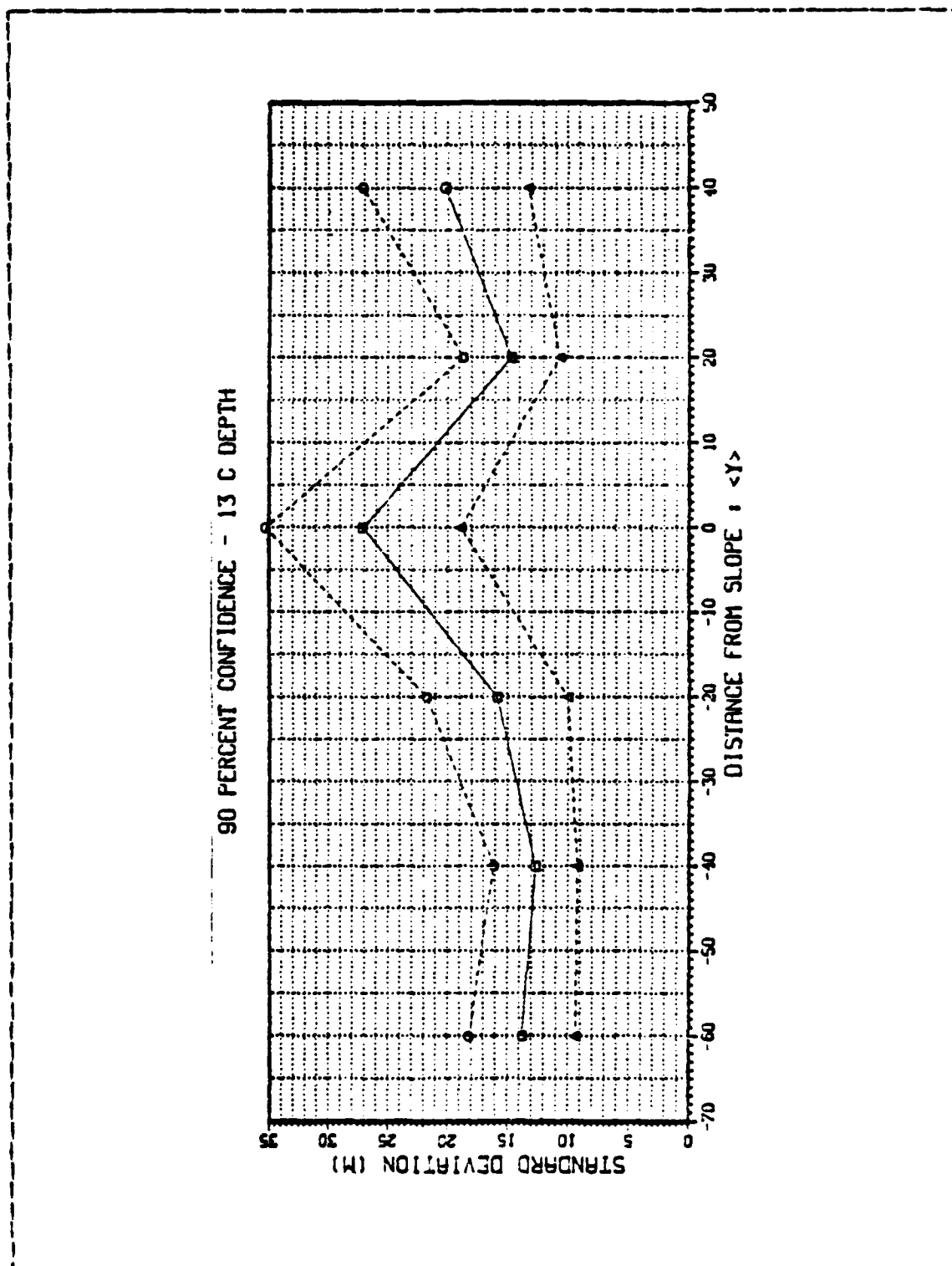
Figure 4.2   ALONG TRACK STANDARD DEVIATION OF ISOTHERMS.
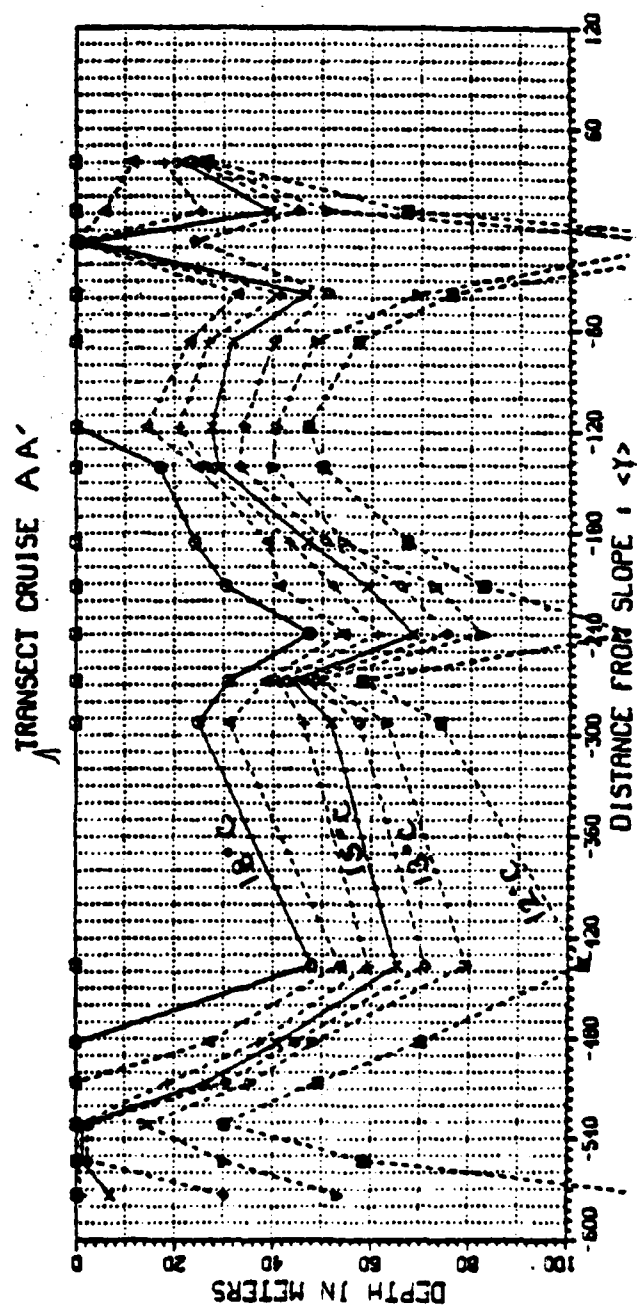
The upwelling at "Y=-540" corresponds to the
Spanish continental shelf.

Figure 4.10   OVERALL TRANSECT OF THE BAY OF BISCAY.

69

1- Pingree 1981
2- Pingree 1981
3- Maillard 1976
4- Maillard 1976
AA'-
BB'- Synoptic data.
CC'-

Figure 4.11   SELECTED REPRESENTATIVE TRANSECTS LOCATIONS.
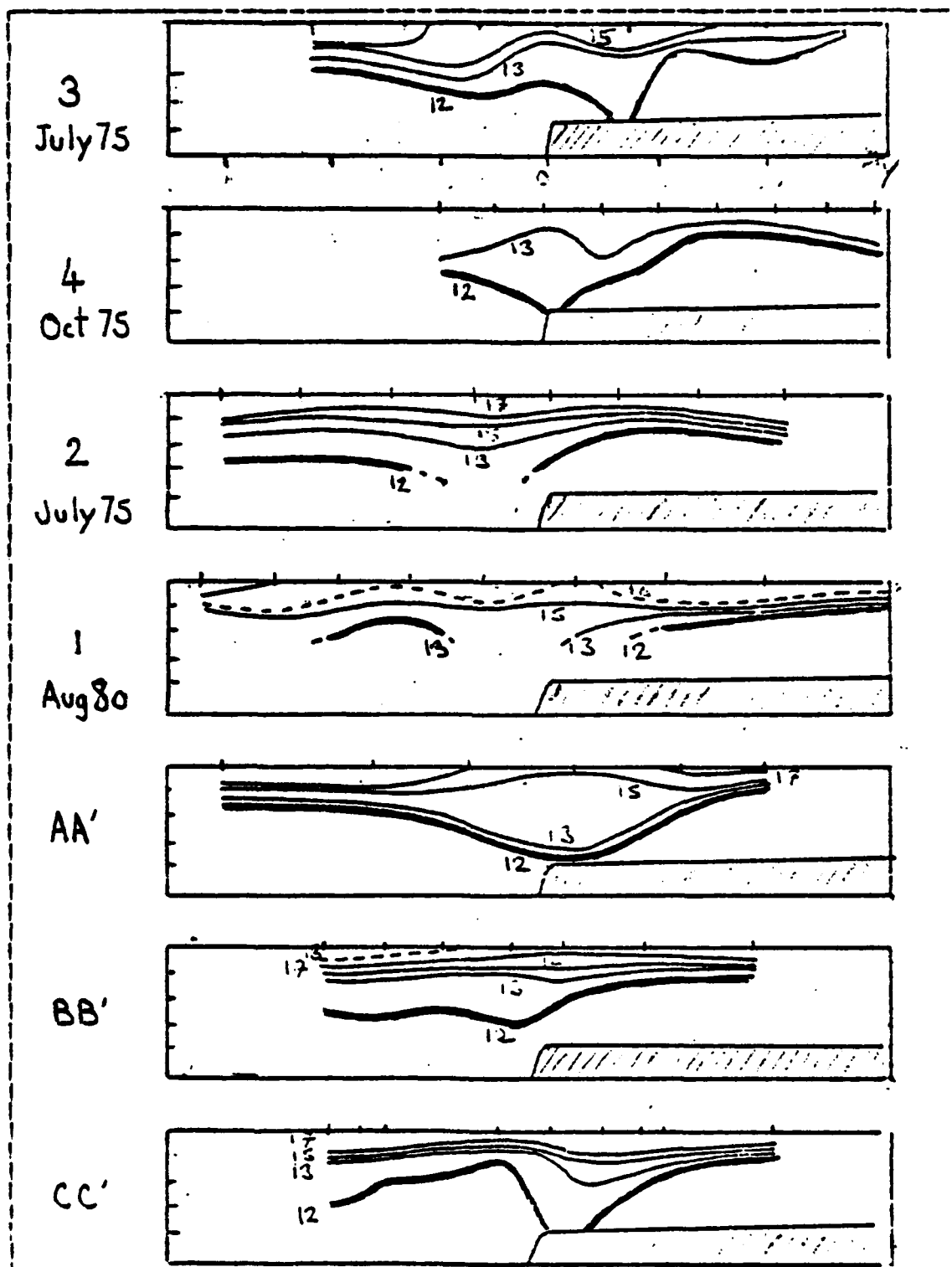
Figure 4.12   SELECTED REPRESENTATIVE TRANSECTS.
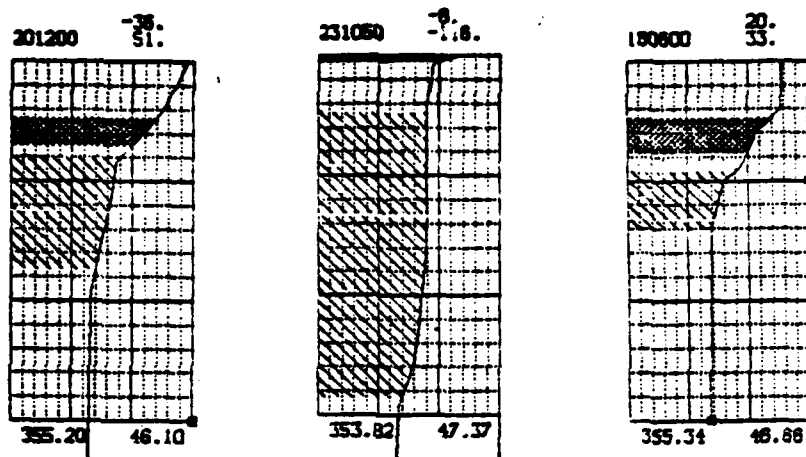
Each XBT profile is displayed on:
    a vertical scale from -150M to the surface
    an horizontal scale from 5 to 20°C

Longitude and latitude are below each sub-plot.

Day-hour groups are given on the higher LHS corner

"Y" and "X" (grid coordinates) values on higher RHS

Dark shading indicates water between 15 and 17°C

Light shading indicates water between 12 and 14°C

Main features of interest are:
    near-surface cooling at the break
    bottom and surface mixing at the shelf
    thermocline stretching and mixing at the break

Figure 4.13   TYPICAL THERMAL STRUCTURE VARIABILITY.
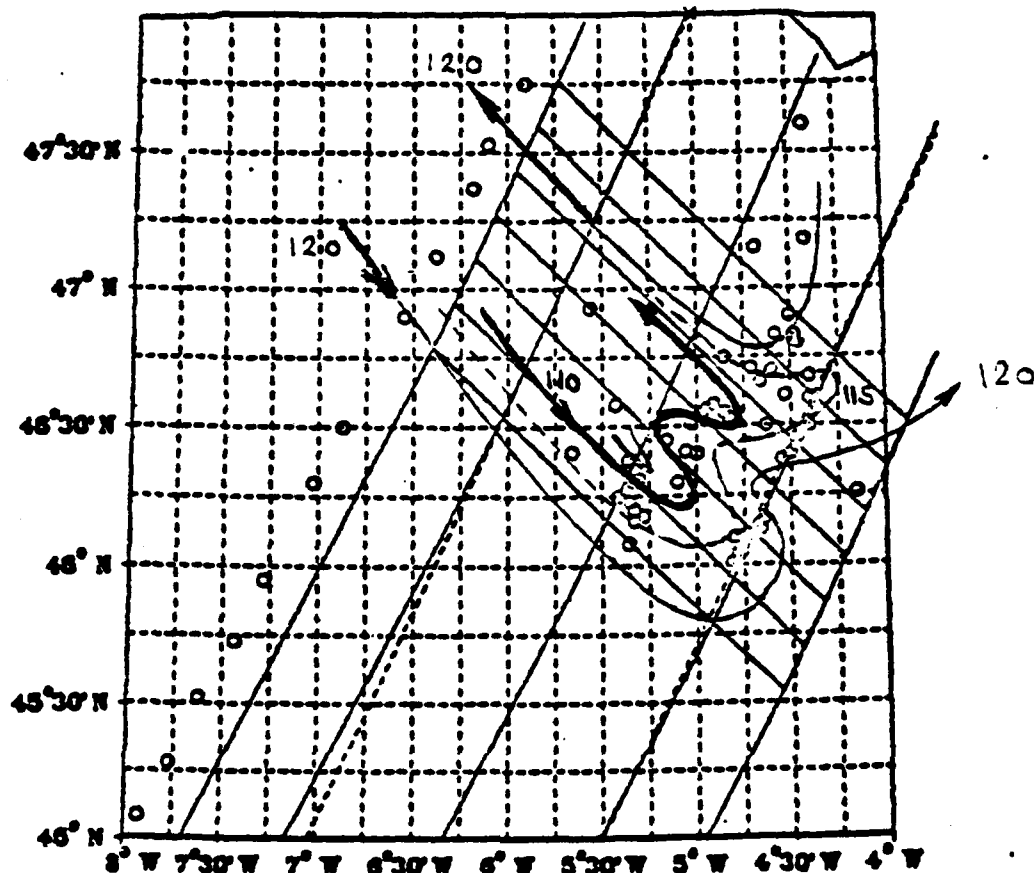
Dynamic heights are taken from a reference level
of no motion at 150M

The associated geostrophic flow is drawn along the
isolines and shows a general cyclonic circulation
to the eastern limit of strong tidal currents (Fig. 3.6)

The presence of an intermediate ridge is suggested
at Y=-20

Figure 4.14   DYNAMIC HEIGHTS AND GEOSTROPHY.

73
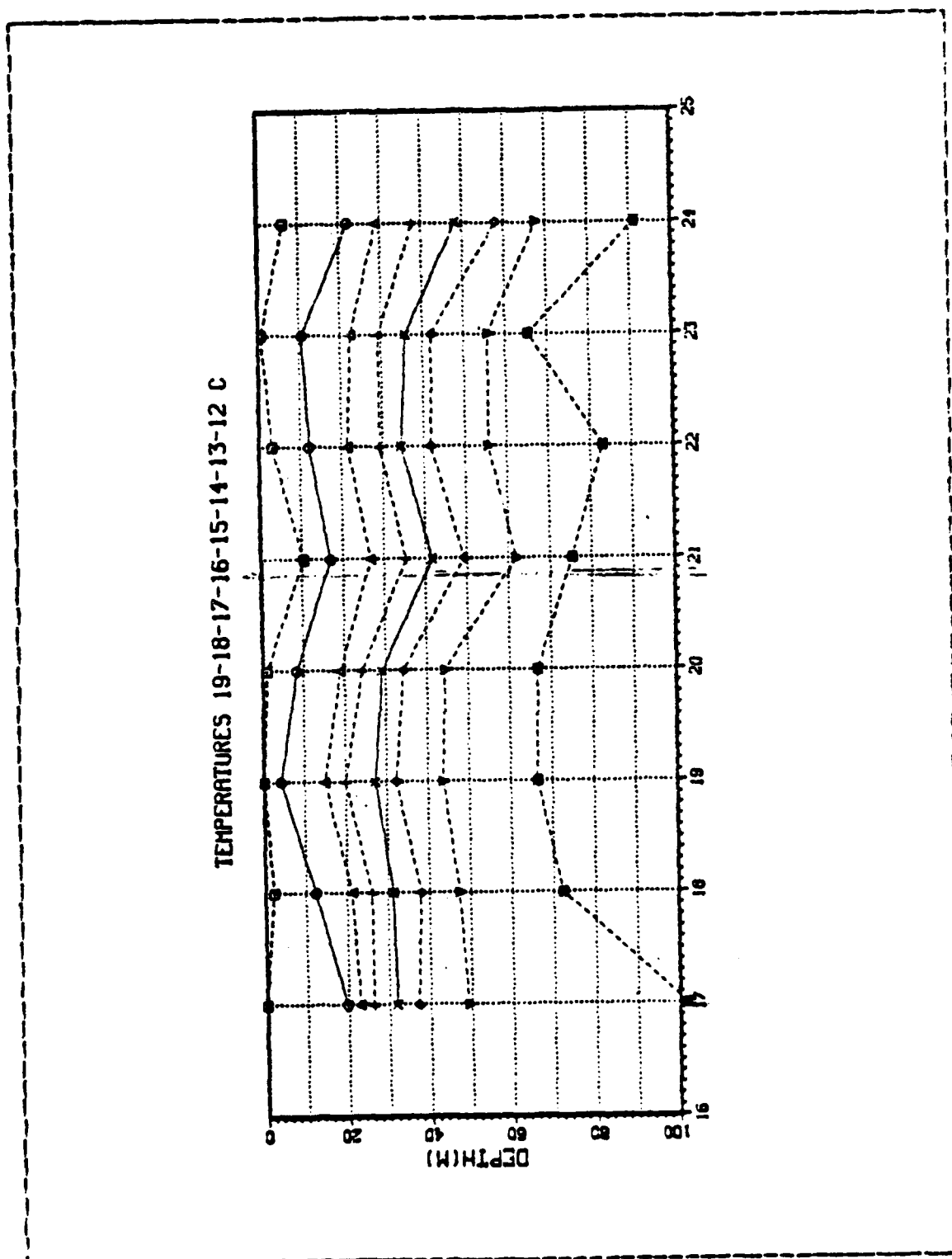
Figure 4.15   DAILY AVERAGE OF ISOTHERMS.

74

Figure 3.16 T-T DIAGRAMS.

75
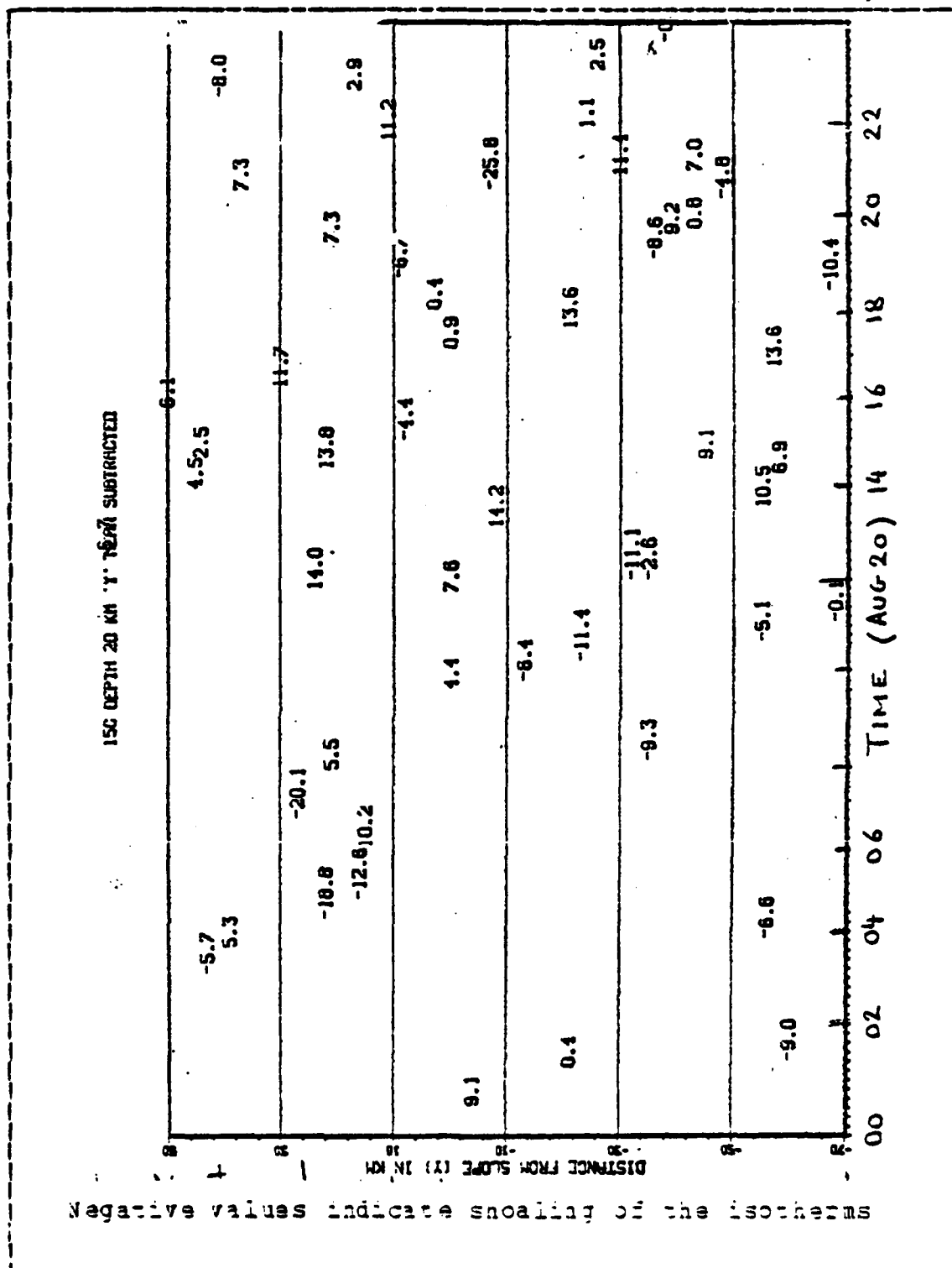
V. SAR IMAGE ANALYSIS

A. ORBIT PARAMETERS AND GEOGRAPHIC REFERENCES

The auxiliary grid introduced previously (I,4) will be used to conveniently locate features with respect to the SAR image and to the average shelfbreak contour. The geographic fit of the SAR image is estimated to be accurate to at least +/- 5KM in the vicinity of the shelf-break.

At 2142Z Aug 20, SEASAT was on a descending node over France with the SAR antenna oriented to the northwest. Consequently, a positive (northward) shear of eastward current would appear on the image as artificially compressed with enhanced Bragg-scatter (Cf Fig. 2.3) In other words, a current directed toward the northwest would appear on the SAR image with a bright northeastern boundary and a dark southwestern one.

TABLE VII
SEASAT ORBIT 785 PARAMETERS

Orbit 785 on August 20 1978 (Julian Day 232)	
Ascending node at	2103.56Z
East Longitude	168.43 02 (decimal degrees)
Descending node at	2154.14Z
East Longitude	335.89 58 (decimal degrees)
Argument of Perigee	w=140
Eccentricity	e=0.0016

B. HEURISTIC ANALYSIS OF THE SAR IMAGE

The patterns visible in the optically processed SAR image may be grouped in four distinct categories according to their geographic location and to their geometric characteristics. They are discussed separately under the titles: "inner shelf", "outer shelf", "generation area", and "propagation area". The image discussed being a positive print, the lowest backscatter radar response will be referred to as dark areas and, conversely, the enhanced signal returns will be referred to as bright or light areas.

A correlation between image characteristics and bathymetric features is made and must take into account two inaccuracies. First the error in mapping the SAR image is estimated as 5KM at most. Secondly the bathymetric chart used here (Fig. 5.5) was constructed by interpolating soundings of different sources, with gaps of ca. 10KM in some places of the continental slope. Hence, the relative positions and shapes of the canyons drawn are subject to caution within the same order of magnitude as the SAR feature locations. Nevertheless, in the case of several assumed correlations between well-defined image and bathymetric features, the confidence may be increased by the perfect relative fit of each of the points (Fig. 5.4).

1. Inner Shelf

(Y>40) - In this area, manifestations of internal activity are of low contrast and lack any obvious organisation. Separated curved lines can nevertheless be identified with an average radius of curvature of 12 KM. Patterns of similar shapes can be associated at spacings of 28KM (Fig. 5.2), but their relation to any kind of periodic phenomena is not proven. They could be due to mesoscale atmospheric variability, or linear slicks associated with a localized convergence (Cf para II-C-2).

77

The lowest limits of wind speeds sufficient for a radar return are attained in the northern part of this area, particularly south of the "Chaussee of Sein" and leeward of the Britanny Coast where mesoscale land-sea breeze may well have been predominant. (A ship sailing 100°T can clearly be seen with its wake virtually displaced according to the Doppler effect described in II-B-1).

2. Outer Shelf

(10<Y<40)- Internal wave group patterns are apparent in this region. They appear as arcs of circles, concave to the west with a variable radius of curvature of minimum value 15KM. They are limited to the north by a caustic in which they merge; this line is brighter, i.e., of greater backscatter. They are broken to the south by another line of brighter characteristics still. These patterns seem to exist over the entire width of the SAR image, but they appear with more contrast on the western part of it. Some periodicity, of about 28KM length on the x-axis, can be detected.

The wavelength of these patterns is variable in two directions. (1) toward the so-called caustic to the north, the wavelengths decrease to zero, starting at a maximum value on the southern boundary. (2) toward the southeast (increasing x-direction), which is their apparent direction of propagation, the average wavelengths, measured at mid-distance between the two boundaries, is of the order of 1KM on the western side, increasing to 2KM in the middle of the swath.

The most conspicuous wavecrests are located at x=-25, where a high level contrast particularly enhances those curved lines. Each of these arcs appears as two narrow contiguous stripes: a dark (low backscatter) one on the concavity and a bright (high backscatter) one on the

convexity. Hence, over one wavelength on a direction perpendicular to the crests and following the assumed direction of propagation (from the interior to the exterior of the arcs), the backscatter varies approximately in the following way: 70% of the length at a uniform level, 20% at low backscatter level and 10% at a high level on the leading edge. According to the hydrodynamical theory of SAR imaging, this result means that the internal waves responsible for these patterns are long-crested with deep narrow troughs (Fig. 2.4).

The southern boundary is a general line brighter than the northern caustic particularly on the western part of the image, where it is conspicuous both by its brighter characteristics and by the obvious discontinuity it creates in the general patterns. This boundary is located approximately (+/- 5KM) over the 180M isobath, thus corresponding to the upper break in the continental slope.

3. Continental Slope or Generation Area

(0<Y<10) - This area covers the upper part of the slope between the 150 and 1000M isobaths. Once again the mesoscale features are concentrated on the western side of the image. The average backscatter is weaker (darker shading) than on both adjacent areas (shelf and deep ocean). The northern limit is the band of lighter characteristics described above.

The limit to the south is (conversely) a discontinuous band of very low backscatter about 1500M wide, which is clearly visible from x=-60 to x=-20 and from x=-5 to x=15. The straightness of this line (vs. the other patterns) and the fact that it is not bordered by any alternating clearer stripes, seem to indicate that it is due, not to a propagating phenomenon, but to a stationary (if not steady) internal feature. These could be symptoms of a surface

divergence according to the kinematical theory of SAR imaging.

In this area, well-organised coherent circular patterns suggest cylindrical spreading of internal waves from several distinct point sources. Assuming that the direction of propagation of a given wavepacket can be estimated both by the curvature of the crests and by the relative wavelength dispersion sense, the following main point souces can be identified and given names for further reference.

P1 centered at $\quad$ X=-42 $\qquad$ = 47°00N

$\qquad\qquad\qquad\qquad$ Y=0 $\qquad$ =005°30W

P2 centered at $\quad$ X=-25 $\qquad$ = 46°52N

$\qquad\qquad\qquad\qquad$ Y=0 $\qquad$ =005°18W

P3 centered at $\quad$ X=0 $\qquad$ = 46°45N

$\qquad\qquad\qquad\qquad$ Y=5 $\qquad$ =005°02W

P4 centered at $\quad$ X=45 $\qquad$ = 46°25N

$\qquad\qquad\qquad\qquad$ Y=0 $\qquad$ =004°42W

Point P1 is at the head of Penmarc'h Canyon at 800M depth.

Point P2 is at the head of a narrow and oblique but deep, unnamed canyon.

Point P3 is at the head of Guilvinec Canyon at 800M depth.

Point P4 is at the head of Blavet Canyon at 800M depth.

It is observed that, at the Odet canyon there is no evident corresponding internal wave pattern; a plausible reason for this could be that this canyon though steep, does not go up to the shelfbreak itself (Fig. 5.5).

At P1 the leading wave of the nearest group is 15KM from the center. Wavelengths from the leading trough decrease from 2KM to 0.7KM with a range of +/- 50°. Some interference can be seen with a second circular pattern of poorer definition centered around P'1 (X=-44, Y=-10).

At P2, two wave groups propagate in two distinct directions. The first group propagates toward 130°T along the X-axis with its leading wave at 10KM from the center. The second group propagates with a 30° inclination offshore (160°T), its leading wave being at 18KM from the center and having the greater wavelength in the group as above.

At P3, no obvious group can be identified but the pattern appears as a superposition of faint ellipses with their major axis oriented 130°T along the X-axis.

In the vicinity of P4, patterns are still more confused, but a quasi-circular group extends around it at a distance of 17KM.

4. Continental Rise or Propagation Area

(-90<Y<0) The surface patterns here are more blurred than in the three areas described above. Features are on a larger scale and do not present the same east-west variability. The brightness is uniform over the whole area. The general geometric organization is that of arcs of circles roughly centered on the point sources defined above, or more generally, on the 1000M isobath. Some alternating black and white bands may be identified, but are larger and do not contrast sharply on a grey backdrop (in contrast to the so-called generation area). The distribution of those circular bands is not always clear, but some particular patterns with similar shapes can be found at a spacing of ca. 23 KM.

81

C. ANALYSIS OF THE SWELL

The remotely generated swell is long and well organized, thus giving generally well identified patterns on the SAR image. Some apparent geographic variability in direction and crest length can be observed and could be indicative either of variations in the nonlinear imaging mechanism, or of real deformations in the swell field by interaction with surface currents or mesoscale winds. The wavelength of the swell is 237M (at 47°N,0040.30'W) +/- 30M. This corresponds to a period of 12.3 seconds, a phase speed of 19.2 M/S, and a group speed of 9.6 M/S. The direction of propagation is well defined and easily measurable on the shelf and offshore Spain on the southern part of the SAR image. In the vicinity of the Armorican shelfbreak, the patterns are more confused and mix with the internal wave field. On the shelf, the general orientation is 115°T (at 47°N,0040W). In the open ocean (46°N,006°W), it is 135°T. South of the shelfbreak it seems to drastically bend towards the south as if refracted by an opposing current. This particular feature will be discussed further in section VI-E.

D. SUMMARY

On the shelf, and, particularly in the first 30 KM inshore of the shelfbreak, the general orientation of the surface patterns suggest an internal motion propagating along the isobaths and toward the east. A strong and localized divergence follows the shelfbreak at 180m of depth, clearly limiting to the north a generation area on the slope where several point-sources can be identified at the heads of sharp canyons. Internal waves are generated in packets which are clearly visible at short distances from their generation points. Wavelengths of the internal waves, as well as the spacing between packets, are highly variable,

82

but both increase with the distance offshore from the slope. The general intensity and contrast of all patterns decrease from the northwest to the southeast (with decreasing range from the SAR antenna).
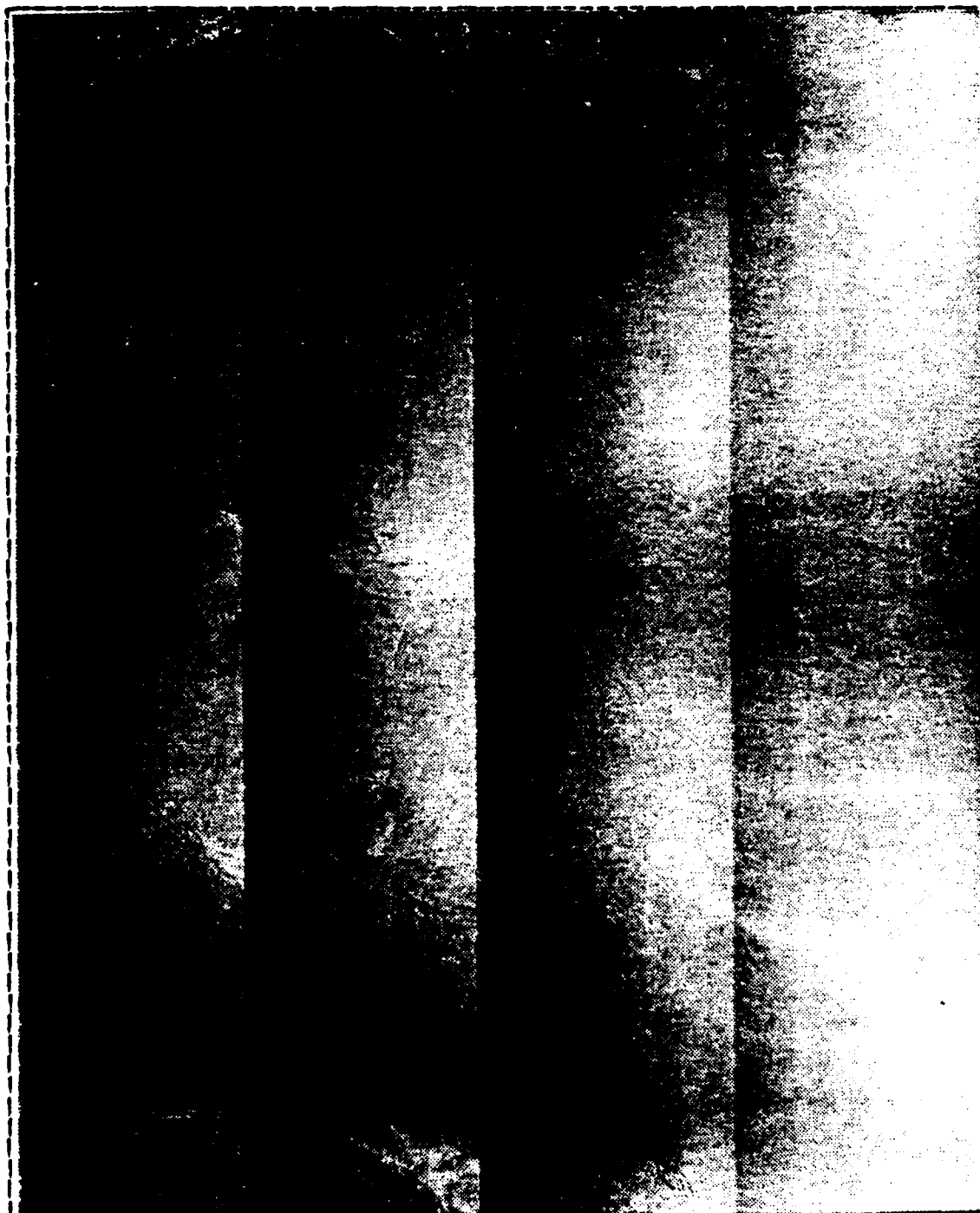
A ship on southeast course appears with its wake
between the two left subswaths at 40KM from the coast

Figure 5.1   SAR IMAGE OF THE CONTINENTAL SHELF.
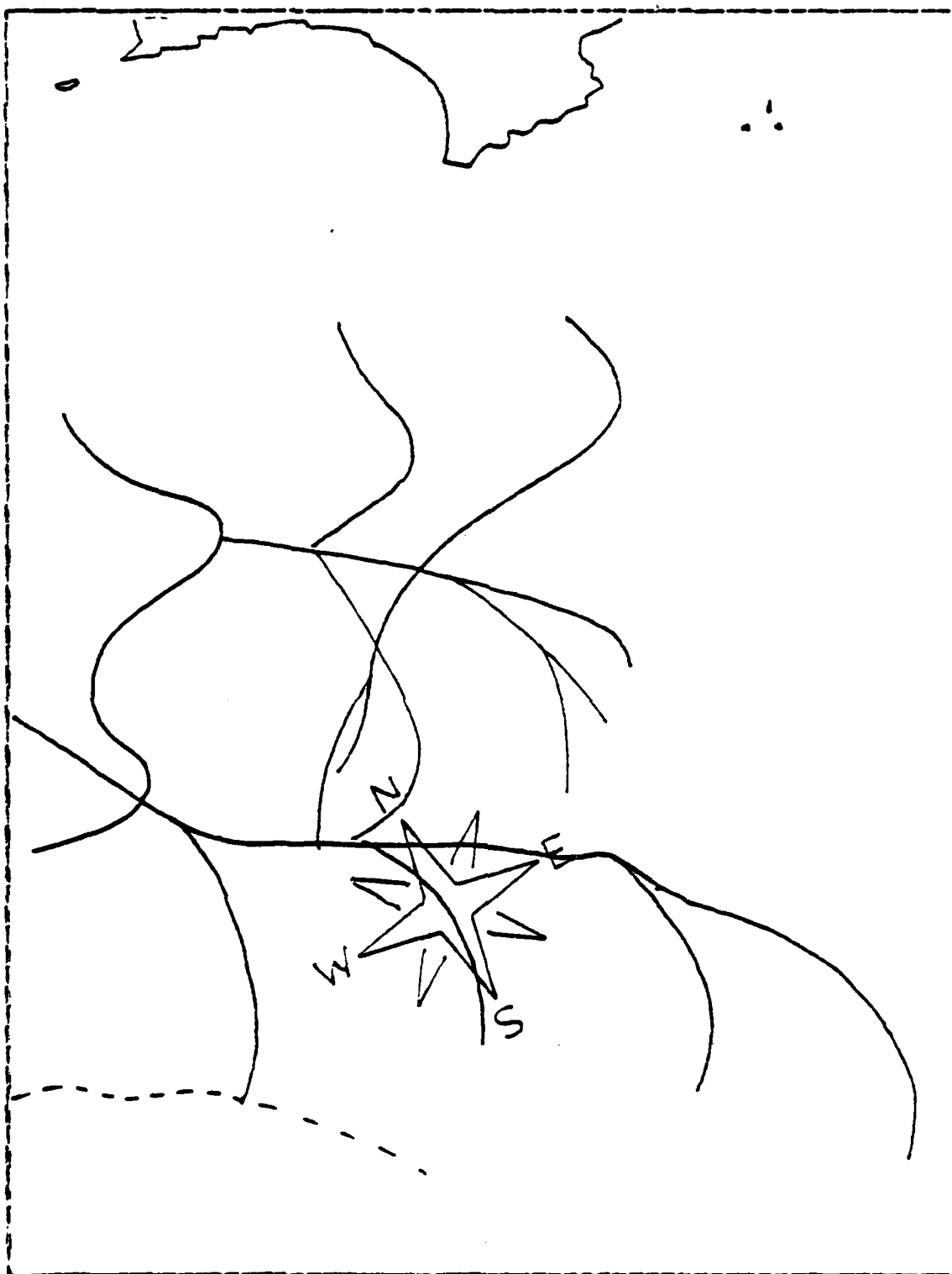
Figure 5.2   LINE DRAWING OF SURFACE PATTERNS.
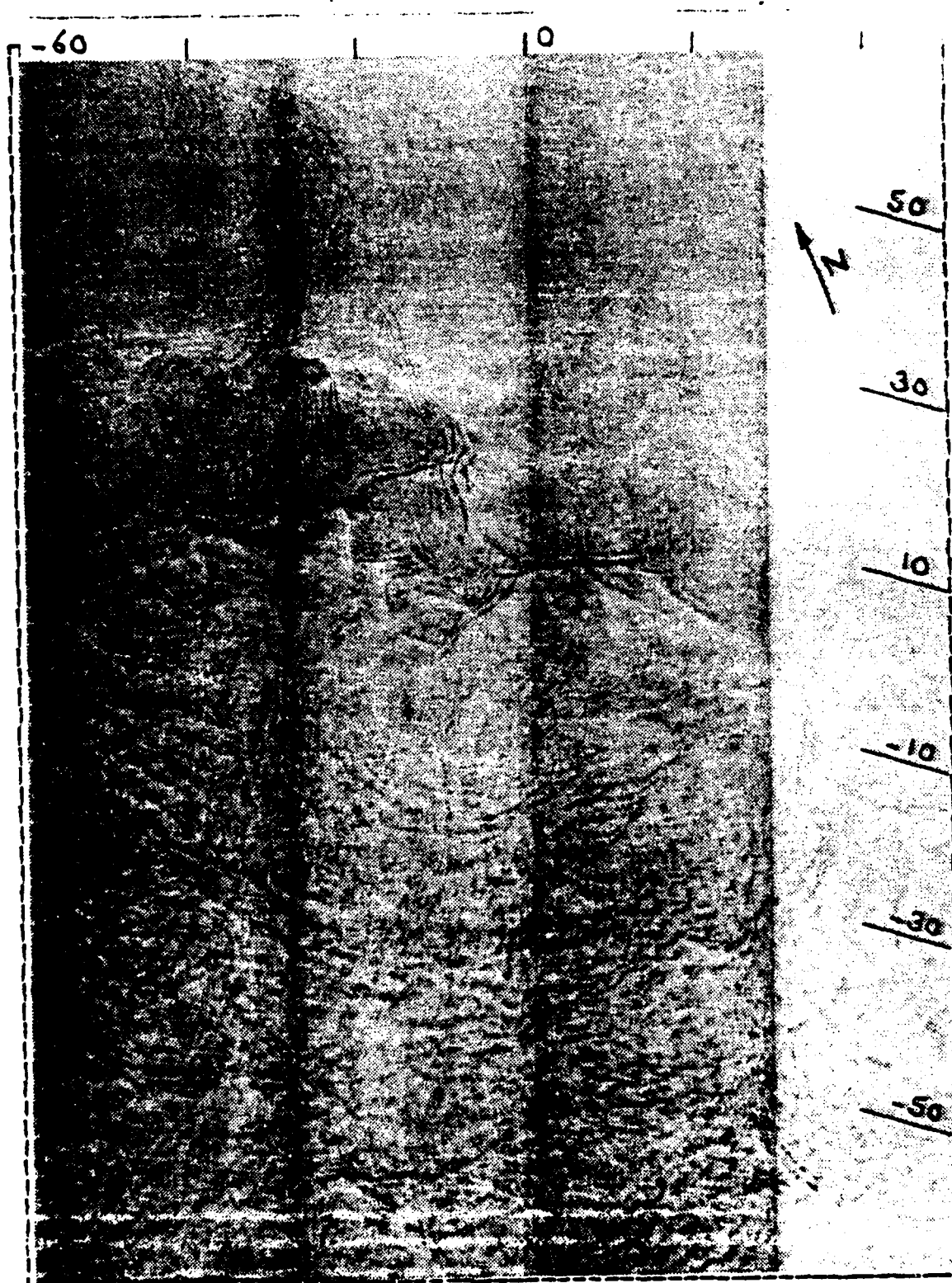
Figure 5.3   SAR IMAGE OF THE SHELF BREAK AND SLOPE.

86
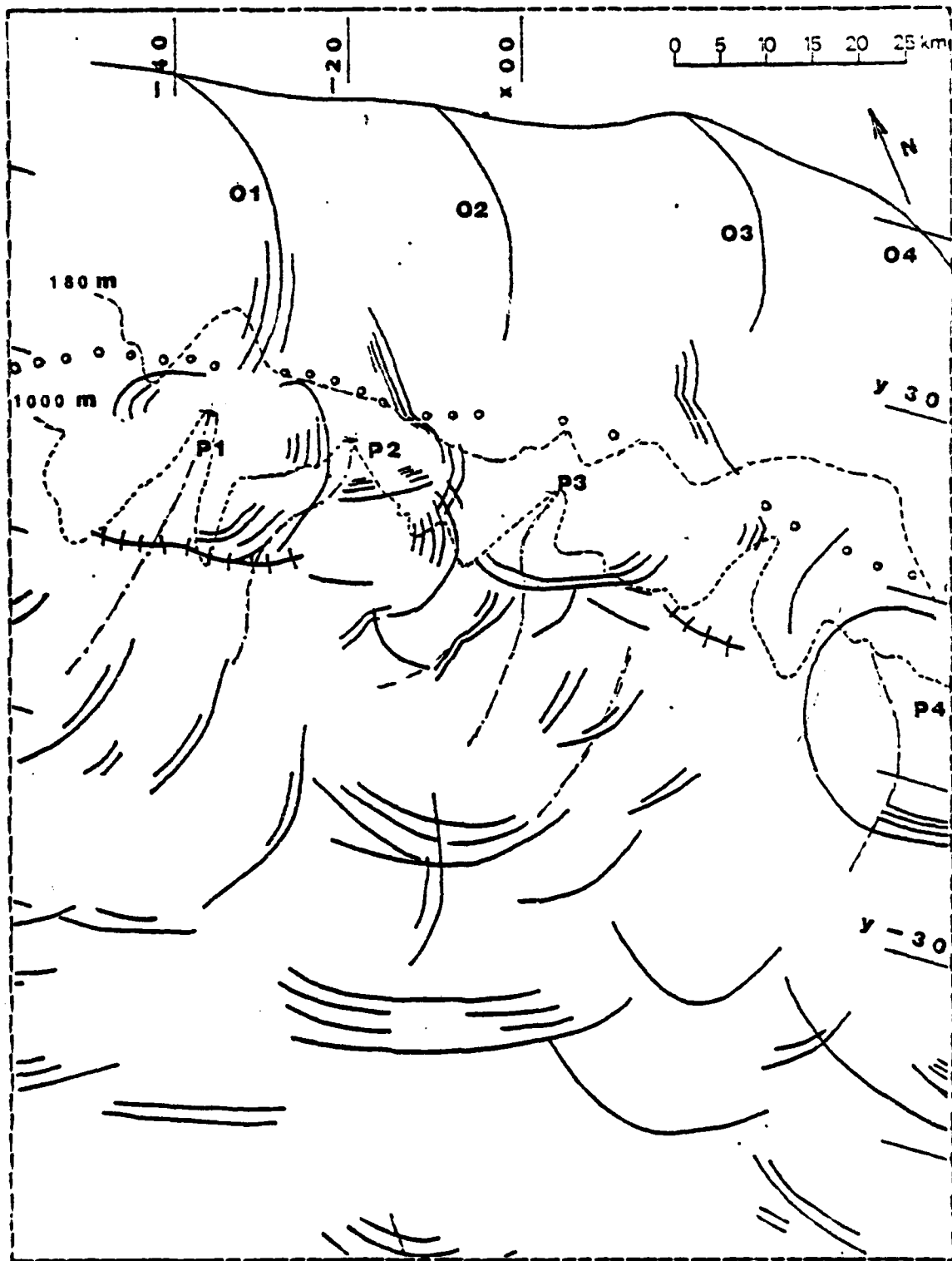
Figure 5.4 LINE DRAWING OF SHELFBREAK AND SLOPE AREAS.

Same scale as two previous figures.

Figure 6.5   BATHYMETRY OF THE SHELFBREAK.

VI. CORRELATIVE INTERPRETATION OF THE SAR IMAGE

The entire area of the continental slope imaged by SAR is dominated by surface manifestations of short internal waves. These internal waves appear in groups which are probably generated at the shelfbreak in association with a semidiurnal internal tide, but eventually decouple from it as both perturbations propagate offshore. Two different fields of internal waves have to be considered; (1) the internal tidal wave with a semidiurnal period of 12.4 hours, and (2) the higher frequency waves generated in packets as forced by the internal tide interacting with shelf bathymetry, or by dissipating energy at higher wavenumber by breaking processes. The characteristics of these internal waves are derived from their surface manifestations (Cf chapter V). Comparing the results with a synoptic conventional analysis (Cf chapter IV) of thermal structure and Eulerian current measurements, gives a notion of the validity of an operational approach where a SAR image could be the basis for hindcasting the actual internal motions.

A. TWO LAYER MODEL ON THE SHELF

The sharpness of the thermocline on the continental shelf allows the assumption, in a first step, of a two-layer ocean and use of the corresponding dispersion relation to compute phase speeds for given observed wavelengths. The dispersion equation is:

$$c_p^2 = \frac{g}{k} \frac{\Delta \rho}{\rho_0 \coth kh_0 + \rho_1 \coth kh_1}$$

On the outer shelf, for a given internal wave crest, the observed increase of wavelength from the "caustics" (Cf V-B-2) to the leading middle point averages 25%. Working by logarithmic differentiation on the simplified form of the dispersion equation

$$c^2 = g \frac{\Delta \rho}{\rho} \frac{h(H-h)}{H} ,$$

gives an approximate relation between this wavelength relative variations and the increase in mixed layer depth:

$$2 \frac{\delta c}{c} = 2 \frac{\delta \lambda}{\lambda} = \frac{\delta h}{h} - \frac{\delta h}{H-h} ,$$

and

$$\delta h = 2 \frac{\delta \lambda}{\lambda} \frac{h(H-h)}{H-2h} .$$

According to the observed variations and to the mean thermocline depth derived from XBT data, the thermocline depth is estimated to vary on the outer shelf from 25M on the boundaries to 55M at mid-distance from each of them.

On the continental slope, a linear interfacial wave of wavelength 1KM yields a phase speed of 0.48M/S whereas for 700M the phase speed decreases to 0.47M/S. Applying these results to the distance separating the wave packets generated on the shelf, and assuming the generation points are those bathymetric features described above (Cf.III-B), the travel time would be 9 hours for the leading waves, thus implying a generation at low tide with maximum ebbing surface currents (Cf Table 4.6).

Conversely, and if the generation time was known with better precision relative to the tide phase, observation of the position of similar groups together with density

gradient data could give an estimate of the thermocline depth.

This two-layer approximation would hold if the thermocline was sharp enough or equivalently if, at its level, the Brunt-Vaisala frequency profile exhibited a strong peak, thus trapping the energy of high frequency internal waves in an horizontal channel. But indeed, the actual ocean has not such a simplified structure , particularly in the "generation area", where dramatic mixing processes are taking place. Furthermore, at low frequencies such as semidiurnal, the vertical movements extend to the whole water column and cannot be described without a vertical modal analysis.

B. NORMAL MODES OF THE BAROCLINIC INTERNAL TIDE

Internal baroclinic modes of the ocean were computed from the density profiles extracted from observed temperature soundings and climatological salinity data (see Table VIII). The Brunt-Vaisala frequency is the free oscillation frequency for a given density gradient :

$$N^2 = -\frac{g}{\rho}\left(\frac{d\rho}{dz} - \frac{g}{c^2}\right) .$$

Density gradients were calculated by the equation of state from the observed temperature profiles sampled by XBT data, and assuming a constant vertical salinity profile of 35.6‰ in the deep water and of 35.4‰ on the continental slope from climatological data. Brunt-Vaisala frequencies were then computed in the first 300M and eventually blended to a deep mean climatological profile found in Gould [1973].

The eigenfunctions solving the Sturm Liouville problem of vertical modes give the vertical dependence of the velocity fields for any frequency of internal-inertial oscillation. An infinite number of solutions exist yielding

91

vertical distributions characterized by one or more phase reversals in horizontal speeds with depths (Fig 6.1 and 6.2). For each of these modes internal wavelengths and phase speeds can be found as a function of the forcing frequency.

Computations were accomplished using a numerical solution [Mooers 1971] to the eigenvalue problem. Starting with the boundary condition at the surface, successive corrections of the eigenvalue are made at each iteration to satisfy the bottom boundary condition.

The solutions are defined within a multiplicative factor. An estimate of the vertical distribution of amplitudes values is then necessary to resolve this incertitude. A simple best fit of the amplitude values from available data was made to the first baroclinic mode. Vertical amplitudes at the semidiurnal frequency were extracted from the current meter data (Cf IV-C) : temperature fluctuations as related to the mean vertical thermal gradient at the corresponding depth gave an estimate of the vertical excursions of the isotherms (as shown in IV-E). (The variations of the current meter pressure gauge showed that vertical oscillations of the array itself were negligible)

The second mode vertical profile is coherent with those observations and is consequently assumed to be the mean component of internal energy at the semi-diurnal frequency (Fig. 6.3). Maximum vertical amplitudes are inferred to be at 2000M and of the order of 50M, a level of no vertical movement (modal node) existing at 1300M.

The analysis of the BT soundings exhibits an offshore spacing of perturbations of 45KM corresponding to phase speeds of 1M/S for a semidiurnal generation and wavelengths of 7.2KM in the open sea (90MIN period) from the first mode dispersion analysis.

In conclusion, the internal tide, at least in its first mode, does not appear on the SAR image, neither in the spatial analysis of the thermostructure. Nevertheless, periodic disturbances could be generated at a semi-diurnal rate, consisting of high frequency waves which are discussed now.

TABLE VIII
INTERNAL WAVELENGTHS

WAVELENGTH (KM)						
	PERIODS (Hours)	MODE0 tropic	MODE1	MODE2	MODE3	MODE4
			vs.	Baroclinic	modes	
SHALLOW WATER 150M	12.4	2570.	27.00	10.00	5.60	3.50
	6.0	888.	9.30	3.50	1.90	1.20
	1.2	166.	1.73	0.63	0.35	0.22
	0.4	55.	0.53	0.19	0.12	0.08
MIXING AREA 220M	12.4	3110.	43.0	18.00	12.07	8.98
	6.0	1076.	14.9	6.22	4.17	3.10
	1.2	201.	2.7	1.10	0.76	0.57
	0.4	67.	0.8	0.30	0.21	0.16
DEEP WATER 3500M	12.4	14080.	170.0	76.0	44.00	29.00
	6.0	4870.	58.4	25.8	15.30	9.70
	1.2	382.	2.8	1.8	0.95	0.61
PHASE SPEED (M/S)						
	PERIODS (Hours)	MODE0 tropic	MODE1	MODE2	MODE3	MODE4
			vs.	Baroclinic	modes	
SHALLOW WATER 150M	12.4	57.5	0.60	0.22	0.12	0.08
	6.0	41.1	0.43	0.16	0.09	0.06
	1.2	38.5	0.40	0.15	0.08	0.05
	0.4	38.4	0.37	0.13	0.08	0.05
MIXING AREA 220M	12.4	69.6	0.95	0.40	0.27	0.20
	6.0	49.8	0.59	0.29	0.19	0.14
	1.2	46.5	0.54	0.27	0.18	0.13
	0.4	46.4	0.53	0.23	0.14	0.11
DEEP WATER 3500M	12.4	315.0	3.32	1.70	0.98	0.64
	6.0	225.0	2.70	1.19	0.71	0.45
	1.2	88.4	0.66	0.42	0.22	0.14

C. HIGH FREQUENCY INTERNAL WAVES

The wavelengths in the internal wave packets are of the order of 3KM, yielding frequencies of the order of 70MIN which are consistent with the internal wave climatology (Cf III-F). The spacing of the high frequency wave packets as seen in the propagation area of the SAR image is approximately 23KM.

On the continental shelf, the periodic spacing in the patterns is about 28KM, which is close to the semidiurnal internal wavelength computed for shallow water.

1. Estimation of the Mixed Layer Depth

It is assumed that the climatological density structure of the Bay of Biscay is known, and that frequent XBT surveys as well as remote sensing of the sea surface temperature, allow estimation at any time of the mean density jump at the thermocline. Starting with only this hypothetical element and making abstraction of the actual in-situ data available, it is attempted to compute the thermocline depth as a function of the geonet characteristics of internal waves as derived from the SAR image.

Assuming a climatological density jump of 1.5×10^3 at the thermocline, and observing separation between wave packets of 23KM in the open sea area of the SAR image yields an estimate of the mixed layer depth of 20M. A variation of 10% in the assumed density jump would result in 10% differences in this estimate, whereas changes of 10% in the interpacket distances would result in 20% changes in this derived mixed layer depth. Consequently, if the absolute estimate of the thermocline depth is uncertain, comparison between interpacket distances would be a very sensitive way of estimating time variations.

94

2. Estimation of the Internal Waves Amplitude

Amplitudes of the nonlinear short internal waves were computed by a method described and applied on a similar SAR image by Apel and Gonzalez [1983]. The first assumption made was that in the "generation area" (continental slope), the internal waves visible on the SAR image could reasonably be considered as solitons. By definition, a soliton is a perturbation conserving its shape and general characteristics (except phase), even after collision with another one. This characteristic is apparent in the vicinity of point P1 for example (Fig. 5.3), where several wave packets are superimposed without any notable mutual interference.

This conservative nature of solitons is linked to the fact that the linear phase speed dispersion is counteracted by a nonlinear acceleration dependent on the amplitude itself. This balance is expressed in the last two terms of the Kortweg - de Vries equation:

$$\eta_t + c_0 \eta_x + \alpha \eta \eta_x + \gamma \eta_{xxx} = 0 ,$$

where "η" is the amplitude of the solitary wave propagating with time "t" in the "x" direction, "γ" is the coefficient representing the linear dispersion and "α" is the nonlinear coefficient and is given by

$$\alpha = \frac{3}{2} \int_0^H \rho(z) W^3(z) dz \simeq \frac{3}{2} \frac{h_2 - h_1}{h_2 h_1} ,$$

where "W" is the vertical eigenfunction or structure function, "h_1" and "h_2" are the depths of the layers in a simplified discrete model.

From the mean density stratification observed at the time of the SAR image, and using the vertical modal analysis described above, linear phase speeds "C" for each observed

95

END
FILMED
1-84
DTIC
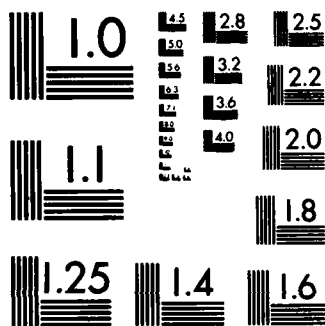
MICROCOPY RESOLUTION TEST CHART
NATIONAL BUREAU OF STANDARDS-1963-A

wavelength, and a phase speed limit "C " for infinitely long
internal waves in a non rotating ocean (steady-state solu-
tion to the Sturm-Liouville problem) were computed.

In one given packet, the wavelength stretch, ("$\int$"),
was defined as the ratio of the observed wavelength to the
linear theoretical one. From the theory [Apel and Gonzales
1983], this ratio is equal to "2K(m²)", twice the complete
elliptic integral of the first kind with argument m²; the
argument m² being itself a function of the soliton's ampli-
tude A:

$$m^2 = \frac{C_0 \alpha}{C_0 - C_p} \frac{A}{3}$$

For any wavelength it is then possible to extract
the nonlinearity due to a given amplitude. Or, conversely,
observing a nonlinear dispersion in the patterns of the
internal waves (by measuring the variation of wavelength in
a given packet), it is possible to derive an estimated
amplitude of the waves.
"α" was taken to be of the order of 5×10^{-2} m¹, ("α^{-1}"=20M).
"C_0" was found to be 0.55M/S.
For each observed wavelength in a given packet, the corre-
sponding phase speed can be computed, and the wavelength
stretch can be measured. A value for "m²" is derived from
which wave amplitude is calculated as

$$A = \frac{C_0 - C_p}{C_0} \frac{3 m^2}{\alpha}$$

For an average stretching, taken from the wavegroups
visible in the generation area, amplitudes of 15M for the
leading waves were found.

D. INTERNAL WAVE INTERACTION WITH SHELFBREAK STUCTURE

Two different kinds of geographic changes in the internal wave group characteristics are apparent (Cf V-B-3). The general shortening in wavelength will be assumed here to be either a Doppler shift due to a current shear or a phase speed compression due to a horizontal density gradient (e.g. as in a front or a mixing area). Refraction of the crests resulting in a deformation from their original cylindrical spreading as in groups northeast of P1 and P2, can, on the other hand, be more surely associated with a strong near surface current. Estimates of the direction of a shear surface current as given by characteristic refraction patterns are indicated on figure 6.4 They give some indication of a general southwestward alongshore flow to the south of the generation area (on the continental slope), opposite to the more localized currents at the shelf break, and to those south of the slope (Fig. 6.4).

E. SWELL REFRACTION AND SHELFBREAK CURRENT

A subjective analysis of the swell refraction was attempted. No Fourier Transforms were made of the SAR image, but in most parts of it, the clarity of the swell field is such that visual estimation of its direction and (with less precision) of its length can be made. It was thought interesting to try to apply recent theories on wave/current interaction to this particular case, where some severe refraction is obvious and the presence of an interacting jet probable. The theory initially developed by Phillips [1981], has been applied to a SAR image of the Gulf Stream by Meadows [1983]; it was transposed with drastic simplifications to this case.

97

In the same way that the Snell's law (loi de Descartes), describes the refraction of a ray encountering a gradient of propagation in a medium, the following equation describes the refraction of swell of a given period, propagating with a phase velocity "c" through an interface between two sea surface areas with surface currents of "u_0" and "u_1"; "α_0" and "α_1" are the angle of incidence and of refraction of a swell "ray" (Fig. 6.5).

$$\cos \alpha_1 = \frac{\cos \alpha_0}{\left[1 - \frac{u_1 - u_0}{c_0} \cos \alpha_c\right]^2} \ .$$

Assuming that the cause of the observed refraction is a shear current directed along the shelfbreak (or at least parallel to the isobaths), the angle of incidence and the angle of refraction (just after the first visible break in the wave crests) were measured. The current speed (equivalently the jet velocity) was estimated to be 0.6M/S. The accuracy obtained cannot be more than 50%, but the basic observation seems reliable enough , at least, to suggest the presence of a jet and to localize the position of the maximum speed at the continental break.
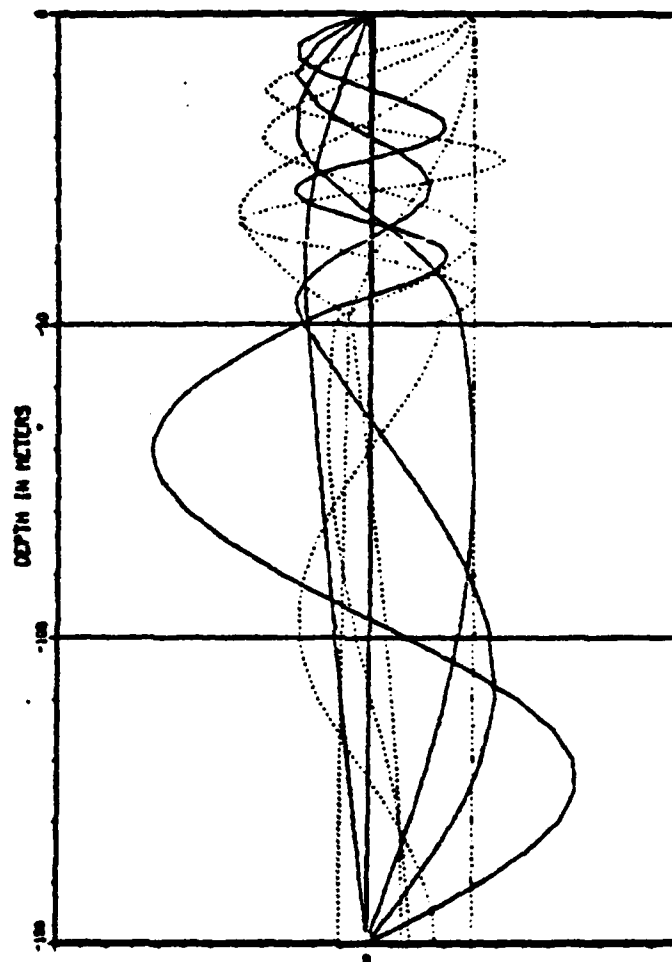
Dashed lines are horiz. speeds normalized to one at Z=0
Full lines are vertical speeds
Mode 1 is the 1(0) zero-crossing horiz.(vert.) profile
Mode n is the n(n-1) zero-crossing horiz.(vert.) profile

Figure 5.1   VERTICAL MODES ON THE SHELF.
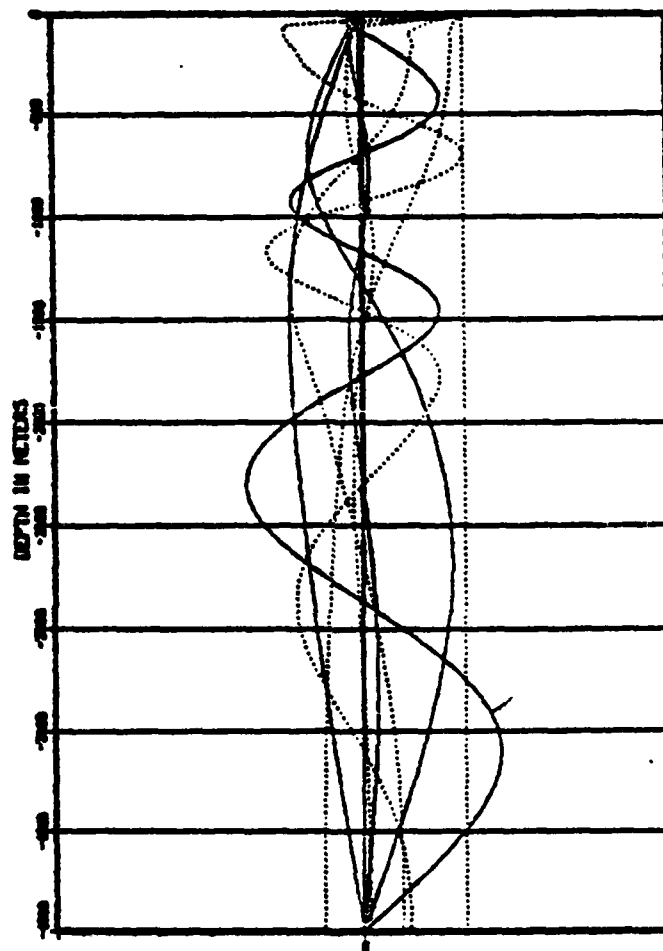
99

Dashed lines are horiz. speeds normalized to one at Z=0
Full lines are vertical speeds
Mode 1 is the 1(0) zero-crossing horiz.(vert.) profile
Mode n is the n(n-1) zero-crossing horiz.(vert.) profile

Figure 5.2   VERTICAL MODES IN THE OPEN SEA.

100
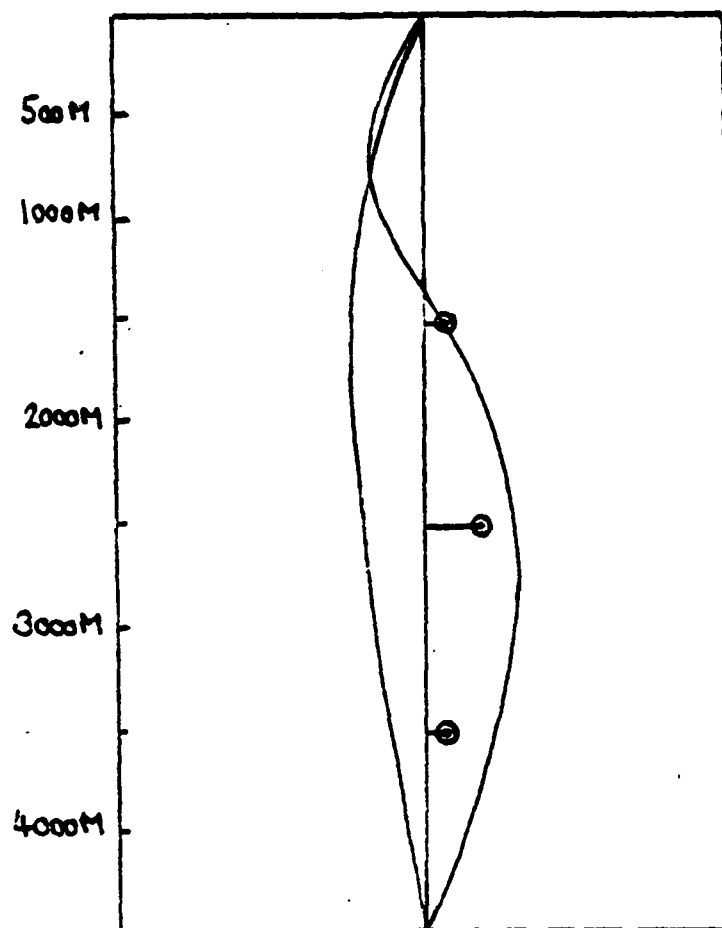
Amplitudes of vertical displacements
as inferred from NBADS mooring (Cf. 17-5).
A least squares fit of these observations to the two
first modes yields a 90% coefficient to the 2nd mode.

Figure 6.3   FIRST MODES ADJUSTMENT TO OPEN SEA DATA.

Current shear estimated from internal wave refraction
Geostrophic flow (Cf. Fig. 4.14)
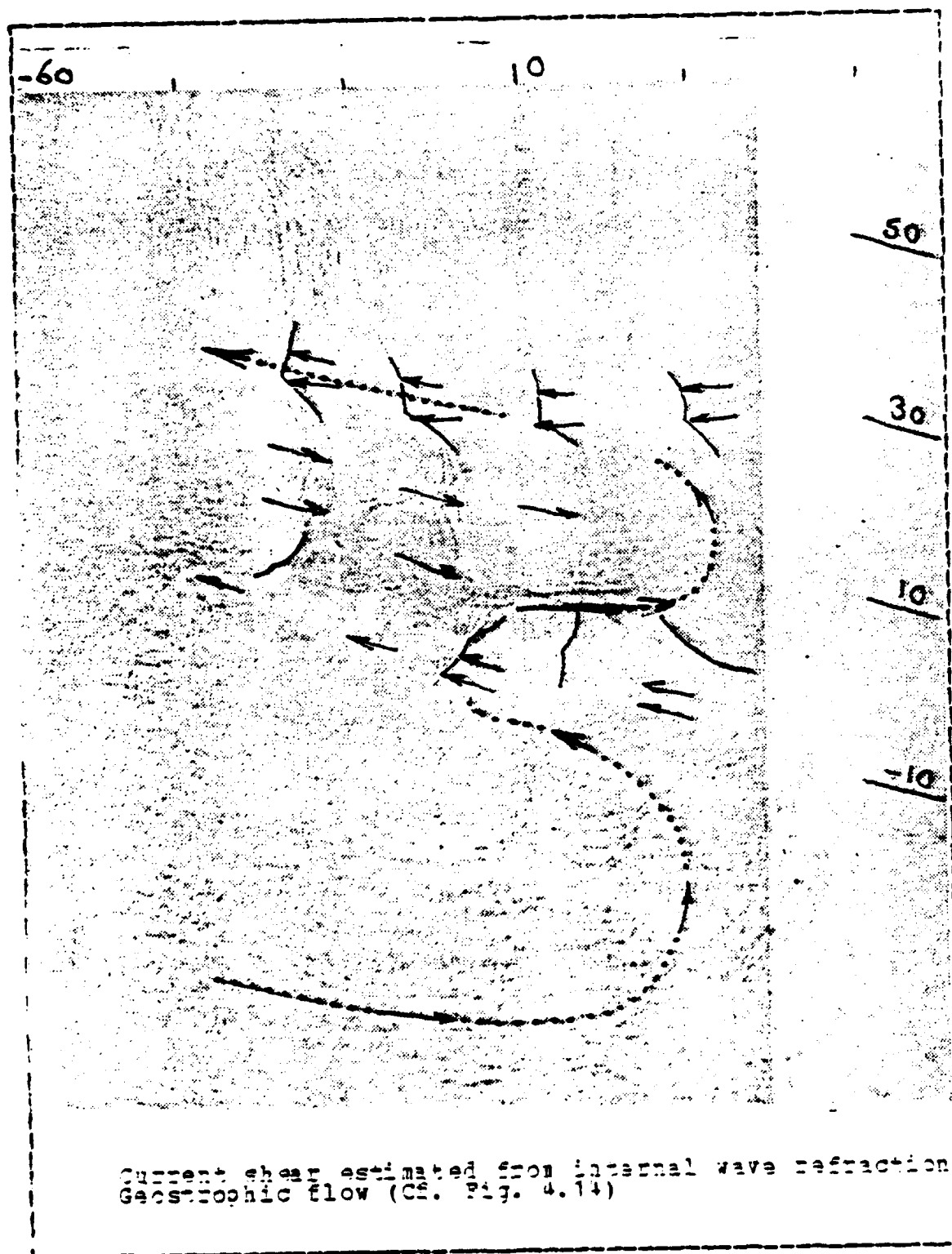
Figure 5.4   ESTIMATION OF SURFACE CURRENT SHEAR.

Parallel lines are swell crests (extrapolated and dashed when out of the SAR image's limits).

⊕: Localization of the observed (SEASAT altimeter) increase in waveheight.
Shown isobath is 1000M.
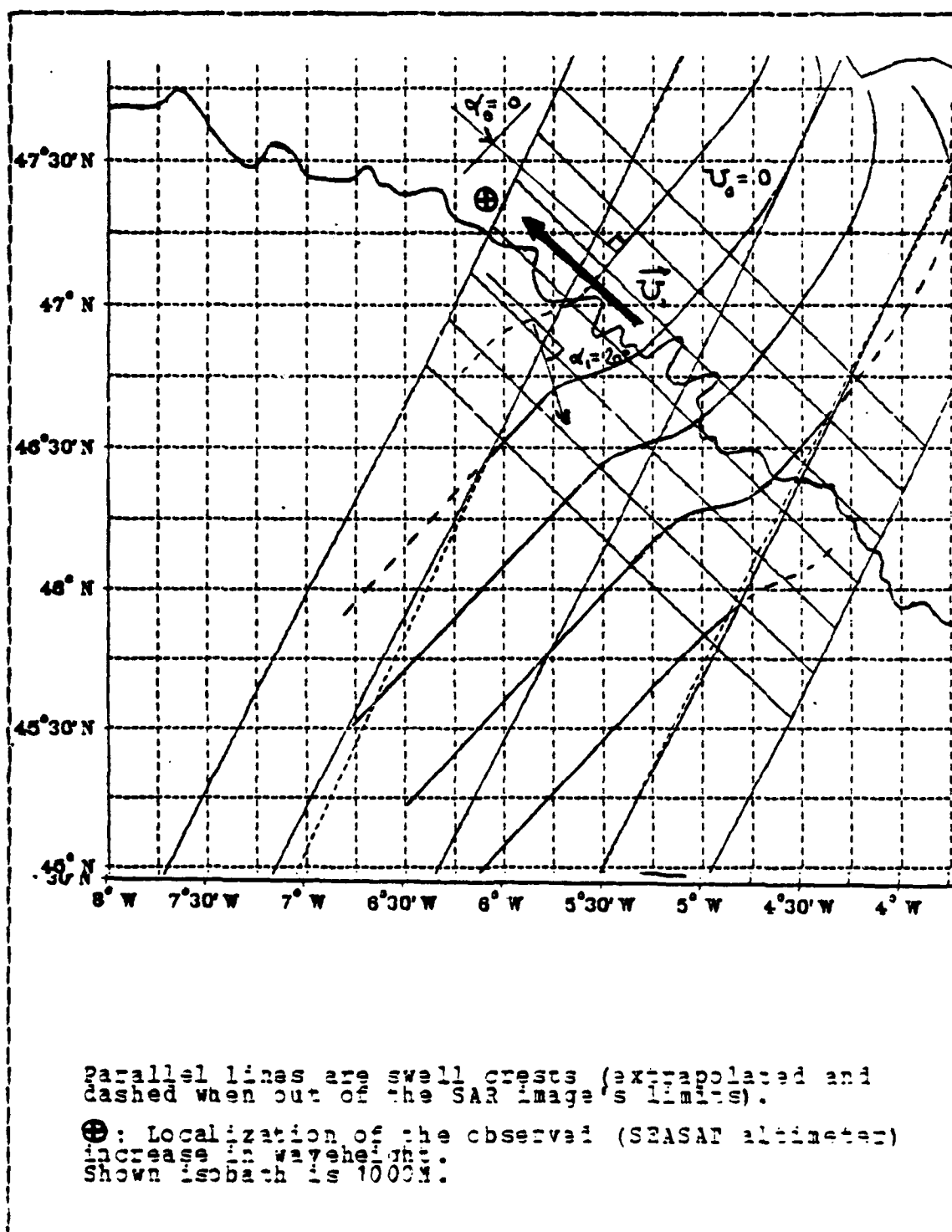
Figure 6.5   CURRENT SWELL REFRACTION HYPOTHESIS.

VII. TENTATIVE EXTRAPOLATION TO GENERAL OCEANIC FEATURES

A. INTERNAL WAVE GENERATION

"In the coastal region internal tides generated on a continental slope are standing waves" [Rattray 1959]. The modal analysis relative to the density structure observed at the time of the SAR image shows wavelengths of the order of 27KM for the semidiurnal first mode internal tide on the shelf. This wavelength is comparable with the spacing of patterns visible on the SAR image north of the shelfbreak. It can therefore be assumed that these patterns correspond to the interaction of another internal perturbation periodically modulated in phase with ridges and troughs in an internal tide. Obviously, the assumption of a perfect standing internal tide would only be true if the boundaries of the shelf sea acted as perfect reflectors.

Wavelengths of the first internal baroclinic modes in deep water are 170KM for mode one, 76KM for mode two and 44KM for mode three. No direct manifestation at these length scales is visible on the SAR image. Nevertheless, the high frequency internal wave packets give an indirect demonstration of the high energy loss encountered by the internal tide at the irregularities in the shelfbreak. Located at the heads of the narrow canyons, oscillations in the water column are estimated (for this specific case of the spring tide) to be of the order of 15M which are assumed to be lee waves forced by the ebbing tidal current. The internal wave packets generated by this mechanism are localized at the canyons extending toward the top of slope to at least the 1000M isobath and occur in bursts. They eventually develop anisotropically due to the presence of a shelfbreak front to

the north. The general direction of propagation is toward
the south-west perpendicular to the continental slope. A
thorough discussion of the possible generation mechanisms is
given by Pingree [1981]. The specific influence of narrow
canyons has been recently enlightened by a laboratory experi-
ment [Baines 1983].

B. TIDAL MIXING ON THE CONTINENTAL SLOPE

Tidal mixing on the continental slope is demonstrated by
the divergence in isotherms in the quasi-synoptic XBT anal-
ysis, (Fig. 4.10 and 4.13). and is in good agreement with
other measurements made in summer and fall at the same loca-
tion. In Pingree (1981), the various hypothesis related to
this mixing are developed.

C. SHELFBREAK FRONTS AND JETS

A new insight on the shelfbreak circulation is given by
the SAR image. Parallel bands of divergence-convergence
which compress internal waves, can be associated with the
thermal structure inferred from BT data and illustrated by
the following simplified scheme of circulation (Fig. 7.1).
Over the shelfbreak, the dynamic heights tend to be lower
than on either side as a consequence of the tidal mixing.
Therefore, a strong geostrophic flow extends to the thermo-
cline, follows the isobaths, and is confined to the shallow
part of the continental slope. The flow is consequently
toward the northwest on the upper part of the slope and
toward the southeast in the offshore half. The idealized
transect (Fig 7.1), accounts for the localized and strong
northwest flow and explains, by stretching of the thermo-
cline offshore, the lower values estimated for the counter-
current. It is nevertheless obvious that any kind of
analytical model based on geostrophy (steady-state) and

alongshore homogeneity cannot be fully appropriate when applied to the Celtic Sea shelfbreak. In this area currents are dominant and limited geographically by the coast of Britanny, bathymetric irregularities are essential in the internal generation processes, and nonlinear effects between the steady-state circulation and the tidal movements may be expected.

The most informative indication of the presence of a strong alongshore jet are the swell refraction and the sudden increase in wave height (IV-B, V-C, VI-E). The coincidence of these phenomena give reliable evidence of a jet which may be related to the poleward eastern boundary current discussed by Swallow [1977].

The barotropic semidiurnal tide propagates onshore,
generates a baroclinic internal tide,
eventually reflected by the steep continental slope.

Another baroclinic tide is generated on the shelf,
and reflected both at the coast and the shelfbreak.

At the canyons, trapping of internal energy induces
large amplitudes vertical movements, generating
high frequency waves, propagating on the thermocline.

Three layers idealized transect.

Surface dynamic heights and geostrophic flow.

Figure 7.1   SCHEMATIC HYPOTHESIS OF SHELFBREAK CIRCULATION.

107

VIII. APPLICATION TO UNDERWATER ACOUSTICS

Of the host of variables affecting sound propagation in the ocean, the temperature profile has the strongest influence. Not only the vertical gradient profiles, but also the horizontal gradient fields, determine the widely varying shapes of the insonification volumes.

Hence temporal and spatial temperature variability should be taken into consideration when forecasting any acoustic quantity, from one single climatic or observed temperature profile. Two approaches are possible in this matter: (1) a deterministic approach would be possible only in the cases where the water-mass's vertical movements are known as functions of time and geographical locations, well enough to allow the forecast of effective variations of the acoustic transmission loss with time, location and orientation of the sound beam, and (2) a probabilistic approach would attempt to model the oscillations without any phase-lock and would only yield estimates of the acoustic propagation variability.

Obviously, in the common case where the geophysical variables vary on a short time scale and without any periodicity, the probabilistic approach is the only one possible. On the other hand, with larger time and space scales, an effort in sampling the actual geophysical environment is eminently beneficial. In the Gulf Stream region, for example, knowledge of the positions of cold and warm eddies has proven instrumental for acoustic forecasts. In the case of shorter scales, but where periodic motions are related to a known generation mechanism (e.g., tides), the same kind of hindcasting may be possible.

It is attempted here to show how the ocean variability observed in the Bay of Biscay may affect sonar detection ranges, and to assess a possibility of analysing the dependence of these ranges on relative positions of source and receiver vs. the internal propagating wave field, as well as on the direction of propagation relative to the internal wave orientation. The internal variability taken as a basic assumption is an idealized extrapolation of the results gathered from the study of the SAR image on August 20 1978. Therefore, it applies only to this given particular situation, and with a wide range of uncertainty.

This approach may prove feasible in similar cases where internal waves can be occasionally sampled, either from space using a SAR, or by adequate in situ sampling techniques based on a thorough knowledge of the internal wave climatology.

The influence of an internal wave field on acoustic propagation is especially critical at high acoustic frequencies, where diffraction and leakage are minimal and where pure geometric ray tracing can be applied. The insonified volume will then drastically vary in the three dimensions. Long internal waves will act as long scale time variations in an observed or predicted SSP (sound speed profile). The effect of short waves can be approached stochastically and lead to establishing statistical conclusions on the range variability. The variation in propagation will be dramatically dependent on (1) the relative position of source (or receiver) with respect to the wave field, (2) the relative direction of sound propagation and wave field orientation, and (3) the mean SSP and its variability in space.

Two cases are to be considered . (1) A long (e.g. tidal) internal wave field for low frequencies (long scales) to evaluate variation on long ranges (of order 20KM) of sound propagation; in this case the Parabolic Equation (PE) Model

has been used.   (2) A short (as seen on the SAR image of the
continental slope) free internal wave field at high frequen-
cies (short scales) to evaluate interaction with a high
frequency acoustic wave. In this case the MEDJSA model was
run.

A.   IDEALIZED WAVE FIELDS

The acoustic model was evaluated assuming that in a
vertical plane the sound speed profile varied from a mean
profile in a periodic way (Fig. 8.1).   This assumed profile
was drawn from the XBT data, and was then idealized and
smoothed to present a perfect surface mixed layer, a sharp
thermocline and a climatological deep profile.   For a
constant SSP two convergence zones are apparent: one due to
the Mediterranean outflow at 1100M,   and another due to the
pressure increase with depth.   The sharp thermocline was
made to vary in depth without any deformation in its thick-
ness or its slope (Fig. 8.1); the shape of this depth varia-
tion was modeled as a periodic curve with wavelengths of 10
and 20KM.

Increasing this internal wavelength by a factor "k" is
equivalent to modeling the ray tracing in a plane oriented
with respect to the wavecrests, at an angle "A" such that

$$\sin (A) = 1/k .$$

It was then possible to calculate transects of the three-
dimensional insonification (or transmission loss) in various
relative directions from the source and draw horizontal
diagrams at one given depth (Fig. 3.3 and 8.4).

110

B. TRANSMISSION LOSS DERIVED FROM THE PE MODEL

The parabolic equation (PE) model developed by NORDA [Brock 1978], modified by NUSC [Lee and Botseas 1982], and adapted (with more modifications) for use at the Naval Postgraduate School, gives a normal mode solution to the wave problem in the form of an elliptic equation. The calculations made with this model must be considered with some caution as the initialization step will affect the near-field results. Principal significance should, therefore, be attached to PE model calculations at the convergence zones (CZ) ranges. In the case where the source was placed over an internal wave crest, no significant directional dependence was observed and the transmission loss was equivalent to that found in a constant SSP environment. Conversely, in the case where the source was placed above an internal wave trough, the convergence zones were found to be enhanced by a varying SSP. Horizontal diagrams of transmission loss were drawn for two levels for the receiver (15 and 45M) by inter-polation between five vertical transmission loss curves at various directions relative to the internal wave field (Fig. 8.4).

C. RAY TRACING WITH MEDUSA

The MEDUSA Range Dependent Ray Model was developed by the Applied Research Laboratories of the University of Texas at Austin under NORDA sponsorship during FY80. MEDUSA uses smooth functions (splines) to interpolate between the discrete SSP's (given as input) and solves the various ray equations numerically for a limited number of characteristic rays (eigenrays). Eigenrays are located by interpolation in range (not in depth as in other ray tracing models) between rays bracketing the receiver in range. The source is assumed to lie on the vertical axis of a cylindrical coordi-

111

nate system, around which the geophysical variables are symmetrical. Eigenrays are located by interpolating between rays bracketing the receiver in range (not in depth). (Hence any direct modeling of horizontal refraction is excluded). The PROFTRP program permits diagnosis of profile artifacts produced in the geophysical interpolation routine. RAYPLT produces ray path plots.

This ray tracing program was used in the same way as the PE model to compute acoustic transmission in vertical planes at various angles with an internal wave field orientation. But here, the features which were investigated were at shorter ranges; the direction dependence exhibited in the horizontal diagrams (Fig. 8.3) relates to an eventual refraction under the mixed layer, thus cancelling (for rays travelling at an angle with the internal wave crests) the "shadow zone". Results are only purely qualitative and would need to be investigated from a transmission loss point of view.

Medusa was used also to input the _horizontal_ sound speed profile as observed in the same idealized internal wave field along an horizontal in the direction of wave propagation and at the mean depth of the thermocline (Fig. 8.2). The result of ray tracing in the horizontal plane will be valid only given the assumption that the rays do not make any depth excursion from the choosen depth of the horizontal SSP. This assumption can be made only because the vertical ray tracing shows that there is a surface sound speed channel, so that a significant part of the acoustic energy will propagate within the range of variation of the mixed layer. Above the the thermocline the sound speed will not exhibit any horizontal gradient and no refraction will occur.

D. GENERAL RESULTS

Transmission losses (TL) in an idealized internal wave field were found to be equivalent to the TL relative to a constant SSP environment if the source was placed over a crest. In the case where the source is above a trough, and for internal wavelengths of 10KM, the transmission loss decreases at the convergence zone by 10dB for an insonification perpendicular to the crests (Fig. 8.4) This anisotropy at long ranges, even if not representative of any real ocean environment, is at least an illustration that passive detection in a long internal wave field will be dramatically direction-dependent and suggest the importance of taking this factor into account in any passive detection scheme.

Ray tracing shows that there is a possibility of insonification of the "shadow zone" beneath the thermocline with a variable SSP structure. This would affect both passive and active search (or escape) tactical patterns at low ranges (of the order of 4000M). Ray tracing in the horizontal suggests the possibility of an horizontal duct (particularly in deep and narrow internal troughs), but the assumptions made here are too drastic to allow any conclusion from the elementary run made with Medusa. Further work in this line should, nonetheless, help to tailor use of any elementary (single SSP) ray trace model to interpret some consequences of a variable SSP on transmission anisotropy.

Figure 8.1   SOUND SPEED BI-DIMENSIONAL PROFILES.

Upper figure: source over an internal wave crest
Lower figure: source in the vicinity of a trough

Perpendicular axis are not at the same scale
Disregard reflection artifacts on upper boundaries
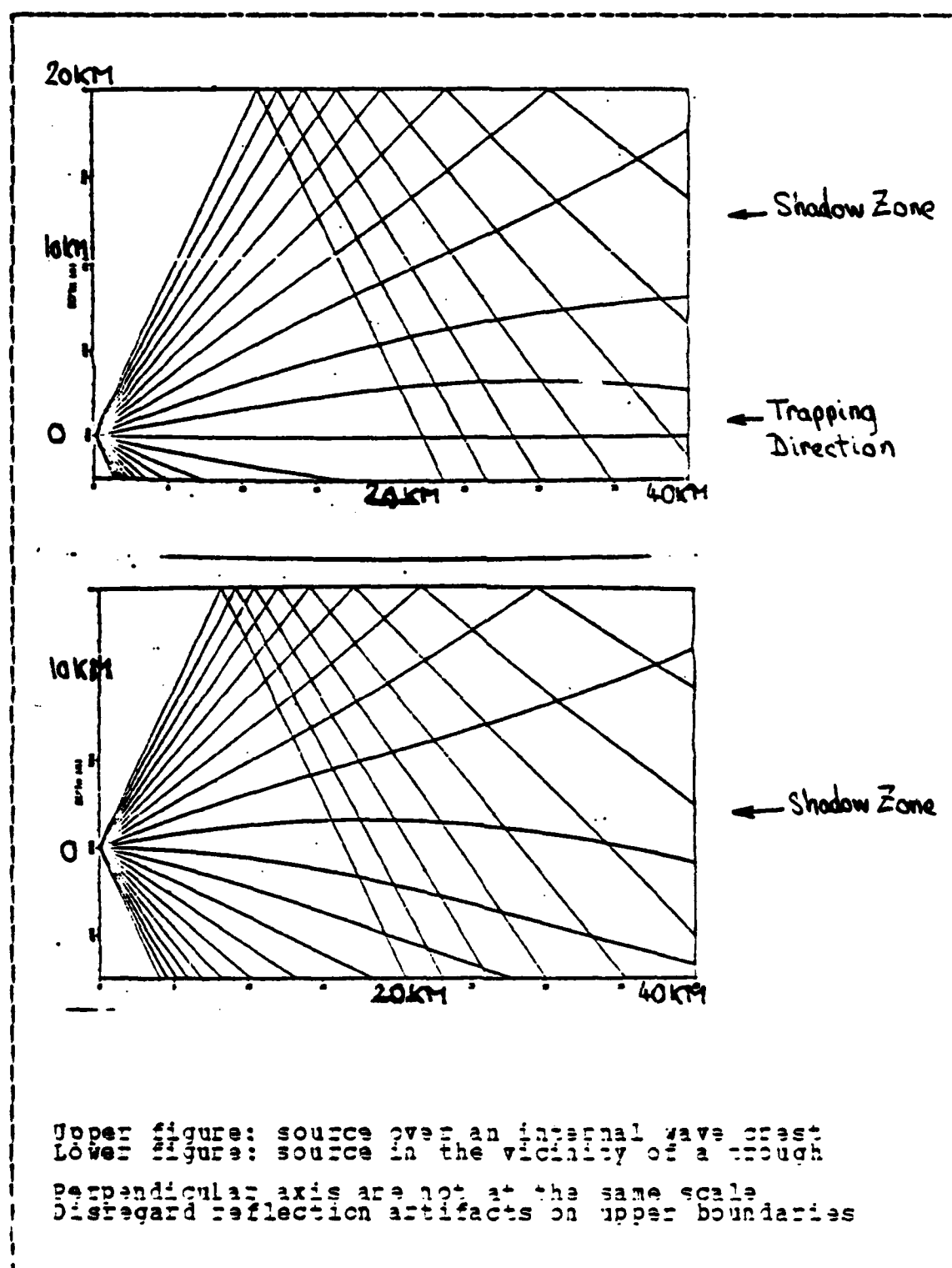
Figure 3.2   HORIZONTAL ACOUSTIC RAY TRACES.
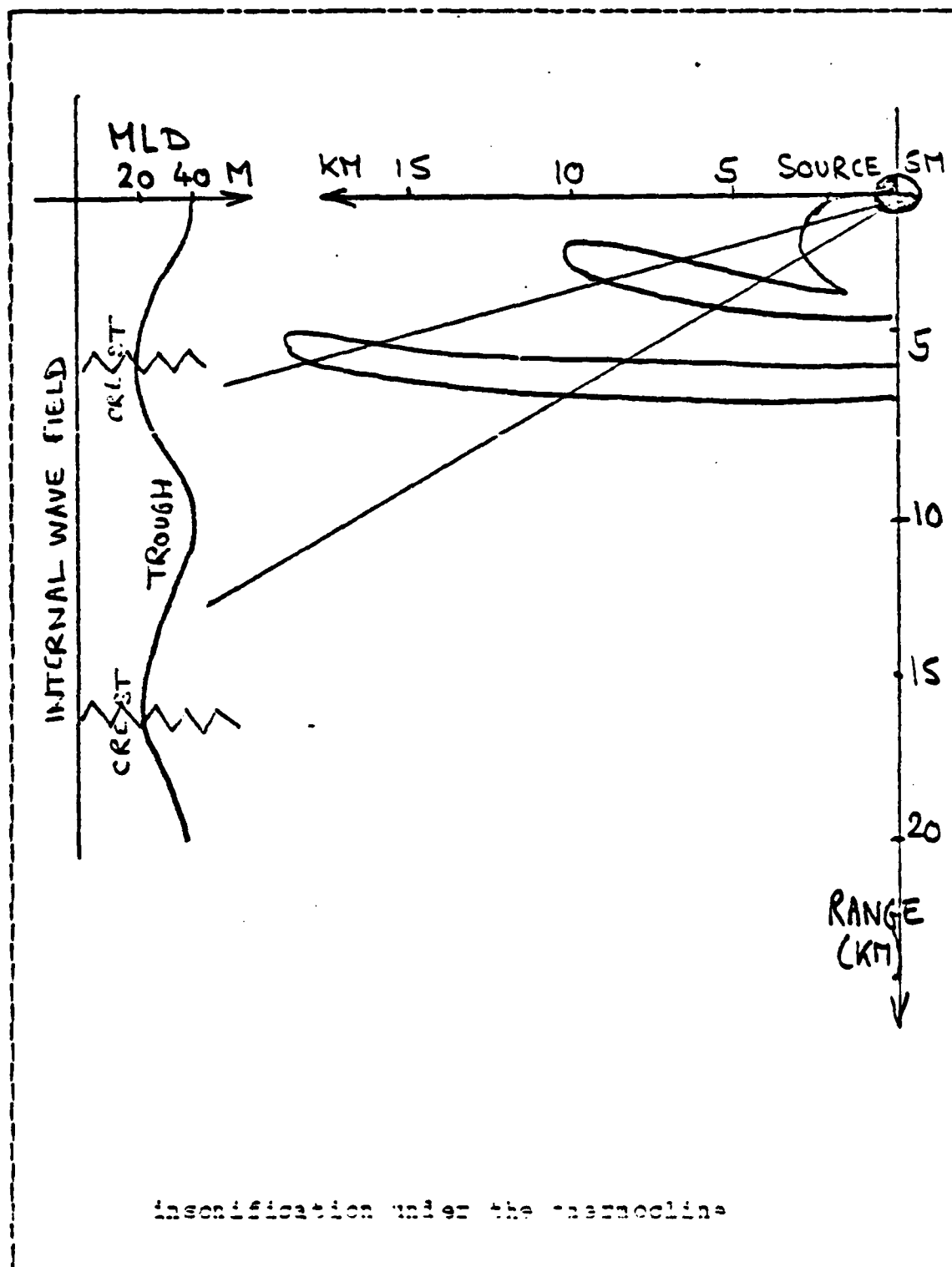
Figure 8.3   INSONIFICATION IN AN HORIZONTAL PLANE.
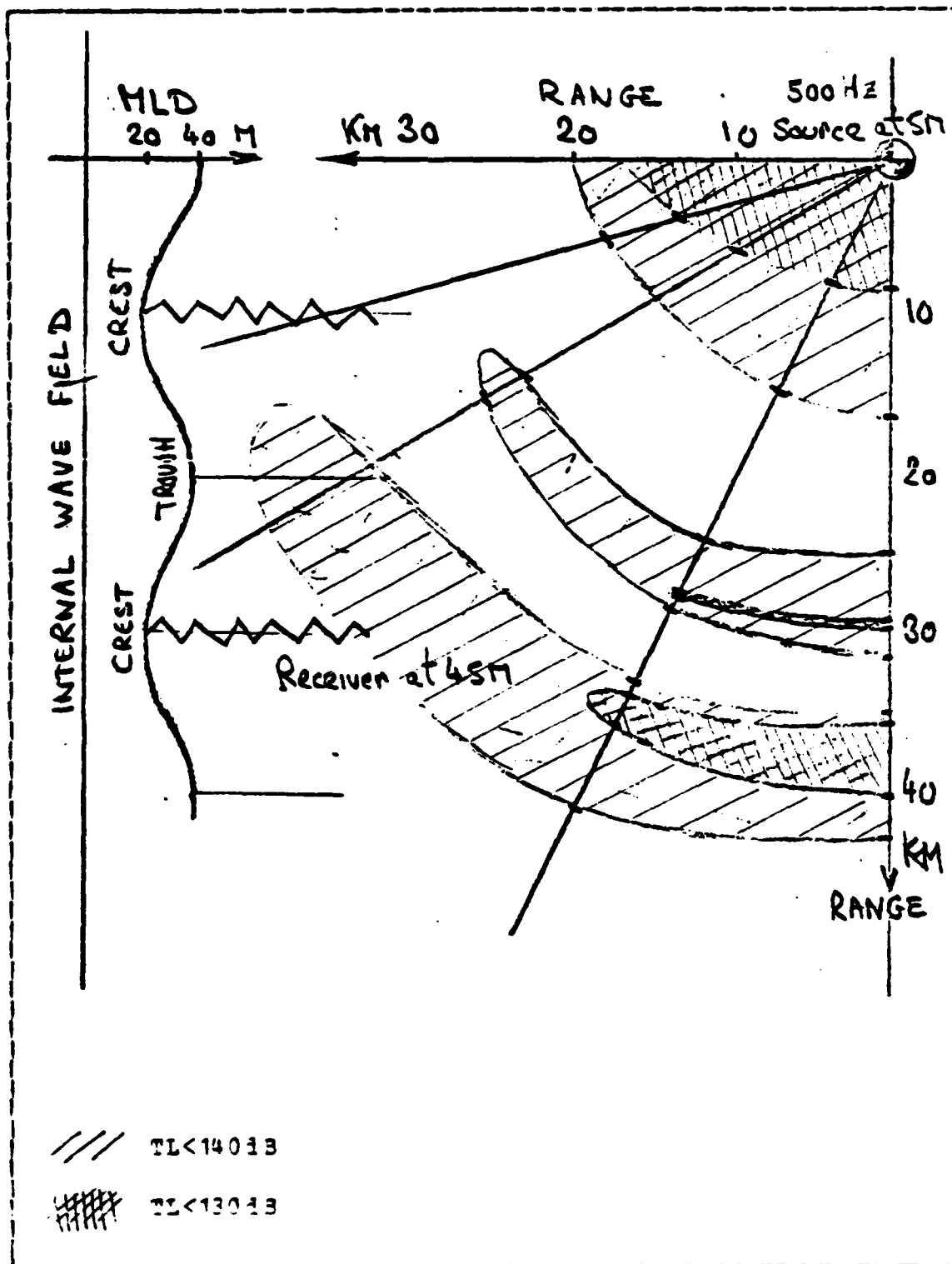
Figure 8.4   TRANSMISSION LOSSES IN AN HORIZONTAL PLANE.

IX. SAR AS AN INTERNAL OCEAN SAMPLING SYSTEM

The SEASAT experiment was the first specific oceanographic use of a SAR from space. Assessments made a priori on its monitoring capabilities have been justified by the large number of oceanic internal processes it observed. In less than 42 hours, it covered an area of 100 million KM² of the Earth's surface (35 of them over the oceans), [Pravdo 1983].

The main specific advantages of a SAR as an ocean remote sensor system are its all-weather capability (in particular with respect to cloud cover, night conditions and sea-state), its high resolution and its sensitivity to the hydrodynamical surface manifestations of internal activity.

The obvious difficulty encountered with an operational use of such a sampling system is the computation time required to process the enormous amount of data (some 10⁶ pixels per second). In the case of an orbiting station (as proven by the SIR-A experiment on the 1982 Shuttle missions), the data may be acquired and exploited on board and/or kept in memory for a further ground-processing. But, for an unmanned satellite, data recording and exploitation require that an earth station be at radio receiving distance from it.

A. GENERAL REQUIREMENTS FOR A SAR OCEAN MONITORING SYSTEM

To possess this particular capability to sample the internal ocean, a SAR system must have some specific characteristics.

B. IN SITU COMPLEMENTARY SIMULTANEOUS PROBING

To analyse characteristics of the internal features displayed by a SAR, the mean density structure must be known. It has been shown (Cf chapter VI) that the mixed layer depth, the amplitudes of high frequency internal waves, and the location of fronts can be inferred from consequent surface patterns. It would therefore be possible to conduct such an analysis in real time if some XBT sampling was made nearly synoptically and could be blended with climatological data.

Obviously time series of temperature structure would be more efficient still by giving synoptic information on the frequency spectrum and vertical modes of the internal motions. A remote, drifting thermistor array as described in [NOSC 1980], if launched in an appropriate position with respect to the a priori internal wave field, could give both an absolute reference to radar remote sensing results and fill in the gaps between two consecutive passages of the satellite. (A radar transpondor could add, at low costs, a geographic reference.)

C. OPERATIONAL PROCESSING AND EXPLOITATION

The analysis of a SAR image may be made on two different levels corresponding to different goals, time constraints and processing facilities (Fig. 9.1).

A heuristic, manual analysis ,similar to the interpretation by meteorologists of a visible or infra-red satellite image of the atmosphere, would probably be effective if other archived images were available. A simple comparison of similar features is capable of giving indications of the relative properties of a given internal wave field, and of the geographic displacement of fronts. Rough quantitative measurements of interpacket separation, wavelengths, and

variation of wavelength, could be used in simple analytical models to compute features of operational interest such as internal wave amplitudes and directions, and location of current jets.

On the other hand, for routine exploitation of SAR images of a given area, the knowledge of climatology could probably help to tailor processing algorithms, eventually using the raw data directly. Once the features of interest are defined by their approximate locations, dimensions and average characteristics, the required data could be extracted as a subset and processed according to specific methods. For example, if a front is known to move parallel to itself and to be characterized on a SAR image by a band of high radar intensity due to convergent enhancement of the surface waves, the mean radar intensity averaged parallel to the front would be enough to locate its position (and intensity). If the presence of high frequency internal waves is assumed, a procedure to extract their mean direction and the distribution of their wavelengths would be to analyse a set of pixels over a limited area by a two-dimensional Fast Fourier Transform technique.
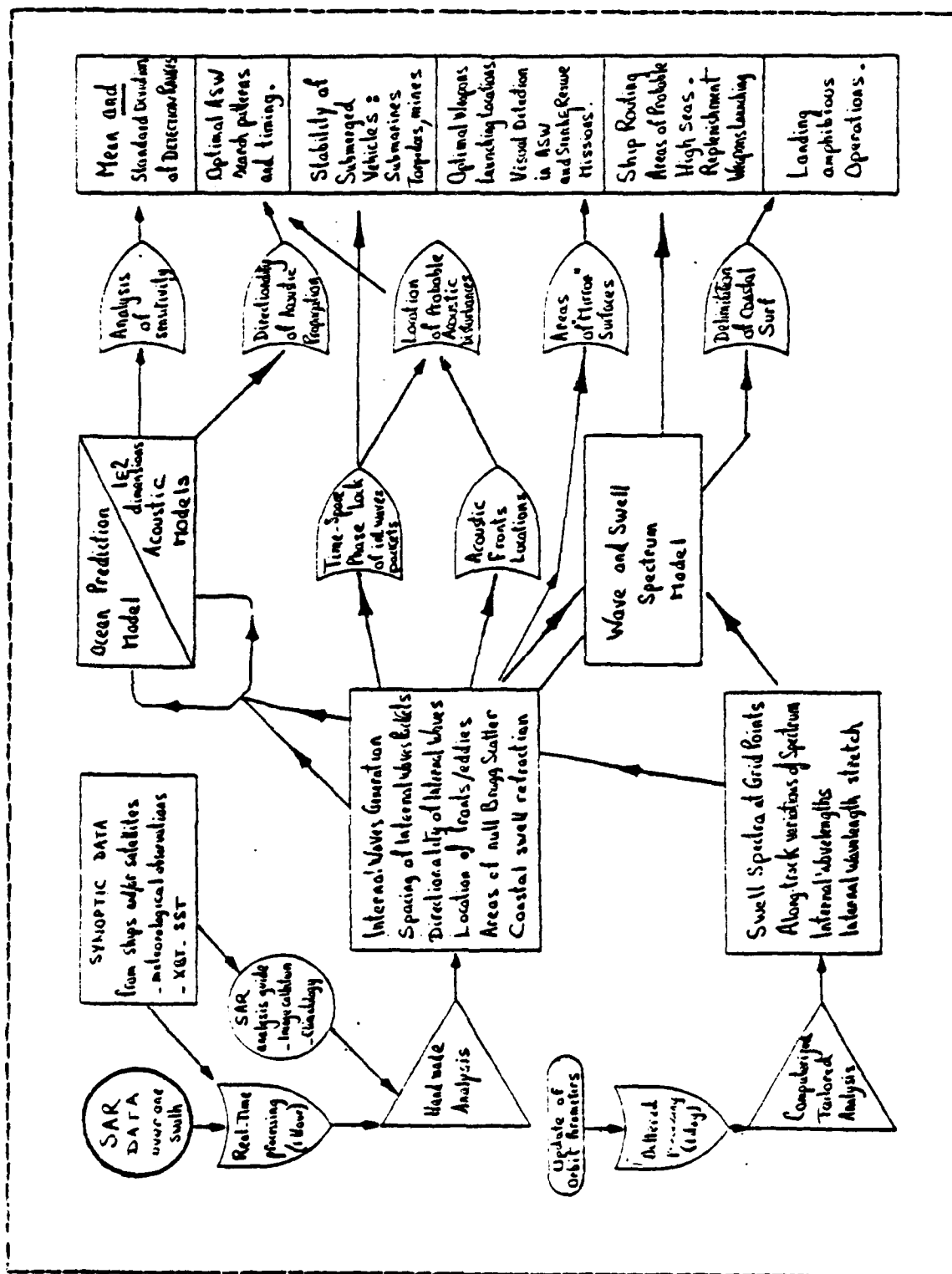
Figure 9.1 OPERATIONAL USE OF SAR DERIVED INFORMATION.

X. SUMMARY AND RECOMMENDATIONS

The SAR image gathered by SEASAT over the Bay of Biscay on August 20 1978 showed a number of internal features which were generally in good agreement with analysed synoptic and climatological data and could have alternatively been used to infer valuable sea-truth in operational, real-time sampling.

Wave packets propagating offshore from the shelfbreak had an inter-packet spacing on the order of 23KM corresponding to a semi-diurnal generation at the main canyons indenting the shelfbreak at low barotropic tide (maximum ebbing surface flow). Speeds computed from observed density profiles were 0.55M/S +/- 0.5. over the slope, which compares well with the wave speed of 0.51M/S calculated for those packets from the SAR image. These high frequency internal waves have a period of the order of 70MIN. Assuming those waves became linear far enough from their generation points, a mean depth of the mixed layer of 20M was inferred and spatial variations ascertained from climatological data and observed group spacing.

Drastic spatial variations in the wavelength observed in a given group and between different ones were analysed, and assumed to be due to current shear and horizontal density gradients. They coincided with a sharp thermal front at the shelfbreak and an alongshore surface geostrophic jet. A line of surface enhancement of Bragg waves corresponded to this front, which was analysed by quasi-synoptic XBT sampling. This front is generally present in summer conditions when a corresponding upwelling breaks the surface.

123

Nonlinear descriptions of the internal waves in each internal wave packet yielded estimates of their amplitudes, probably as large as 15M on the continental slope.

A tentative application to underwater acoustics shows, under severe simplifying assumptions, that detection ranges in such a situation are essentially direction-dependent and that sonar search patterns (or, conversely, submarine escape routes) could be greatly enhanced if these internal features could be sampled on a regular basis and taken into account. Adequate operational XBT sampling could give some in-situ information on this variability. It is recommended that, in areas where internal waves are known to occur, consecutive launches of XBT's be made at a time (or distance) interval, corresponding to half a period (wavelength), thus giving an approximation of the internal wave amplitude and consequently of the variations in detection ranges that can be expected. Internal wave climatology developed using SAR images would be helpful in designing a sampling plan.

The following ocean features of operational interest can be inferred from the SAR image studied here:

a)   An area of intense internal activity is clearly visible on the continental slope in the form of short internal wave groups propagating from the heads of the major canyons and generated approximately at the time of low tide at Brest. These perturbations probably correspond with a larger scale widening (weakening) of the thermocline and periodic mixing processes. The possible operational consequences are (1) drastic changes in detection ranges due to a varying thermal structure in time and space and a probable increase in ambient noise level due to bottom stress and turbidity currents, and (2) sudden modifications in buoyancy that may affect underwater vehicles (e.g., submarines, torpedoes).

b)   A well-defined front, located at the upper part of the shelfbreak, is apparent on the SAR image as a strong

localised enhancement of the high frequency waves. It corresponds to the well-known shelfbreak upwelling in the summer in the area, which has been demonstrated by synoptic XBT sampling. Insonification through such a front is essentially dependent on the relative positions of source and receiver.

c) In the open sea, several fields of internal waves are organised in groups spreading from the shelf. The general direction of the crests is parallel to the isobaths and creates anisotropies in sound speed structure and insonification volume.

d) Other features, not considered here, have eventual tactical importance: (1) the localisation of areas of calms and therefore mirror sea surface for visual search in ASW and SAR (Search and Rescue) missions and site selection for weapon launch, and (2) the coastal refraction of the swell giving a possible surf hindcasting capability for minesweeping and amphibious landing operations.

The coming SIR-B missions will cover the Bay of Biscay and consequently provide some information on the time variability of the characteristics appearing in this single SAR image. Combined international effort to increase synoptic in-situ data acquisition at this time should be eminently beneficial.

Spaceborne imaging radars will supply new capabilities for understanding and perhaps even continually sampling the evolution of the internal ocean. These capabilities may dramatically change the parameters of undersea warfare. Every effort should therefore be made in allied navies to understand and master these consequences, from both scientific and operational points of view, to make sure that no dangerous and destabilizing consequences could result from their universal exploitation.

BIBLIOGRAPHY

Alpers, W. R., and Salusti, E., (1933), Scilla and Charybdis observed from space, J.Geophys.Res., vol 88, 1800-1808

Alpers, W. R., Ross, D. B., and Ruffenach, C. L., (1981), On the detectability of ocean surface waves by real and synthetic aperture radar, J.Geophys.Res., vol 86, 6481-6498

Alpers, W. R., and Ruffenach, C. L., (1979), The effects of orbital motions on synthetic aperture imagery of ocean waves, IEEE Trans. Antennas Propagat., AP-27, 685-690

Apel, J.R., (1983), Nonlinear features of internal waves off Baja California as observed from the SEASAT imaging radar, J. Geophys. Res., Vol 88, No 7; 4459-4466

Baines, P.G., (1981), Satellite observation of Internal Waves on the Australian N.W. shelf, Australian J.Mar.Fresh Water Res., Vol132, No3; 457-463

Baines, P.G., (1982), On Internal Tide Generation Models, Deep-Sea Res., vol 29, No 3A; 307-338

Baines, P.G., (1983), Tidal motions in submarine canyons - a laboratory experiment, J. Phys. Oc., Vol 13; 310-328

Beal, R.C., De Leonibus, P.S., Katz, I., (1981), Spaceborne synthetic aperture radar for oceanography, The Johns Hopkins University Press .Baltimore, New-York

Brock, H.K., (1978), The AESD Parabolic Equation Model, NORDA, TN 12

Brown, W.E., Jr., Elachi, C., and Thomson, T.W., (1976), Radar imaging of ocean surface patterns, J.Geophys.Res., Vol 81, 2657-2667

Canus, Y., (1971), Contribution a l'etude de la circulation au voisinage du fond sur le plateau continental dans le Sud du Golfe de Gascogne, These de docteur du 3eme cycle Universite de Bretagne Occidentale

Carruthers, J.N., (1963), History, sand waves and near-bed currents at la Chapelle Bank, Nature, Vol 197, 942-946

Cartwright, D.E., and Stride, A.H., (1958), Large sand waves near the edge of the continental shelf, Nature, Vol 4601, 41-42

Cartwright, D.E. and Woods, A.J., (1963), Measurements of upper and lower tidal currents at Banc de la Chapelle, Deutsche Hydrographische Zeitschrift, Vol 16, 64-76

Cartwright, D.E., (1980), The tides of the Northeastern Atlantic Ocean, Royal Society of London, Philosophical Transactions, Vol 298 A 1436, 87-135

Cavanie, A.,Hyacinthe, J-L, (1976), Etude des courants et de la maree a la limite du plateau continental d'apres les mesures effectuees pendant la campagne "Golfe de Gascogne" Rapport scientifique technique, CNEXO, N: 23, 87-135

Chiari, P., (1983), Private communication

Curtin and Mooers, C.N.K., (1975), Observation of Internal Waves J.Geophys.Res., Vol 80, 882-390

Danois, (1948), Les profondeurs de la mer, Paris

Dechambenoy C., and others, (1977), Quelques resultats de mesures par navires et avion de la structure thermique superficielle de la mer au large de la Bretagne, Revue Hydrographique Internationale, Monaco LIV (2) July, 1977

Dickson, R.R., Hughes, D.G. (1981), Satellite evidence of mesoscale eddy activity over the Biscay abyssal plain, Oceanologica Acta, Vol 4, Nr 1

Dickson, R.R., Gurbutt, P.A., Narayana Pillai, V., (1980), Satellite evidence of enhanced Upwelling Along the European Continental Slope Jounal of Physical Oceanography, Vol 10, Nr 5,

Dysthe, K.B., and Das, K.P., (1981), Coupling between surface-wave spectrum and an internal wave: modulation al interaction, J.Fluid Mech., 104,483-503

Elachi, C. and Apel, J.R., (1976), Internal Wave Observations made with an Airborne Synthetic Aperture Imaging Radar. Geophysical Res. Lett., 3,647-650

Ellet, D.J., (1982), Problems of Noreast Atlantic Circulation, Challenger Society newsletter 282nd Scientific Meeting 16 September 1982

Etienne, A., (1982), Etude spectrale des Ondes internes et de la Turbulence, Cahiers oceanographiques XXII, 7, 657-685

Ford, J.P., Cimino, J.B., Elachi, C., (1982), Space Shuttle Columbia Views the World With Imaging Radar: the SIR-A experiment, JPL publication Nr 82-95

Foreman, T.L., (1982), The ARL:UT Range Dependent Ray Model MEDUSA, Applied Research Laboratory of the University of Texas at Austin, (unpublished)

Fontanel, A., (1978), Utilisation pour l'oceanologie des satellites d'observation de la terre, Actes de colloques, No5 CNEXO, Paris, 309-326

Fu, L., Holt, B., (1982), Seasat Views Oceans and Sea Ice with Synthetic Aperture Radar, JPL publication 81-120

Gargett, A.E., and Hughes, B.A., (1931), On the Interaction of Surface and Internal Waves, J.Fluid.Mech., 52, 179-192

Gonzales and others, (1979), SEASAT Synthetic Aperture Radar: Ocean Wave Detection Capabilities. Science 204, 1418-1421

Gould, W.J., (1978), Currents on continental margins and beyond Philosophical Transactions ,R. soc. London A 290, 87-98

Gould, W.J., Mc Kee, W.D., (1973), Vertical structure of Semi-diurnal Tidal Currents in the Bay of Biscay. Nature, Vol 244, Nr 5411, 88-91,

Gould, W.J., (1971), Observation of an event in some current measurements in the Bay of Biscay Deep-Sea Research, Vol 18, 35-49

Harger, R.O., (1981), SAR Ocean Imaging Mechanisms, In "Spaceborne Synthetic Aperture Radar for Oceanography", 20-37, edited by Beal, R.C., Deleonibus, P., and Katz I., John Hopkins Press, Baltimore Md

Hasselmann, K., (1980), A simple algorithm for the direct extraction of two-dimensional surface radar image spectrum from the return signal of a synthetic a perture radar, Int.J.Remote sensing, Vol1, No3, 219-240

Hecht, A., and Hughes, P., (1971), Observations of temperature fluctuations in the upper layers of the Bay of Biscay, Deep-Sea Resarch, Vol 18, 663 to 534

Huthnance, (1980), Waves and Currents near the Continental Shelf Edge, Report No 97 I.O.S. (unpublished manuscript),

James, I.D., (1982), Tidal currents at two deep-sea moorings near the shelf edge, Deep-Sea Research, 1971, Vol 29, N: 9A, 1099-1111

Katz, E.J., (1967), Effect of th Propagatin of Internal Water Waves on Underwater Sound transmission, Journal of Acoustical Society of America, 42, 83

Kiyo Tomiyasu, (1978), Tutorial Review of synthetic aperture radar with applications to Imaging of the Ocean Surface,

Laughton, A.S, Roberts, D.G., Graves, R., (1975), Bathymetry of the Northeast Atlantic : MidAtlantic Ridge to Southwest Europe, Deep Sea Research, 22, 791-310

Leblond, P.H., Mysak, L.A., (1980), Waves in the ocean

Lee, D., Botseas 3., (1982), An implicit finite-differneca computer model for soving the parabolic equation, NUSC, TR 6659.

Lee, O.S., (1961), Effect of an Internal Wave on Sound in the Ocean, Journal of Acoustical Society of America, 33:677-681

Lee, O.S., (1965), Summary of Published Information on Internal Waves in the sea with Notes on Application to Naval Operations, NEL Technical Report

Lee, O.S., (1964), Internal Waves and Sound Pressure Level Changes, First U.S. Navy Symposium on Military Oceanography, Naval Oceanographic Office, 17-19 June(1964.

Le Floch, J., Mauvais, J-L, (1968), Mesures de courant au voisinage du fond dans le Golfe de Gascogne, Cahiers Oceanographiques, XX, 10 D68, 885 to 892

Le Floch, J., Sur la circulation de l'eau d'origine mediterraneenne dans le Golfe de Gascogne et ses variations a courte periode, Cahiers Oceanographiques, XXI, 7 653 to 661

Le Floch, J., Maze, R. (1980), Un aspect de la dynamique des fronts thermiques profonds du plateau continental de Bretagne Sud. Influence du passage d'une depression, Annales Hydrographiques, N: 755

Le Floch, J., Sur quelques observations de fluctuations de temperature et de vitesse de courant associees a des ondes internes ou a la turbulence, Cahiers Oceanographiques

Le Floch, J., (1978), Quelques aspects de l'oceanographie physique du plateau continental armoricain J. Rech. Oceanogr., Vol III Nr 2,

Little, A.D., (1966), Internal Waves: Their influence Upon Naval Operations, Report to the Navy Bureau of Ships, No. 4090266, Contract NObsr 93055, Project SF-101-03-21, Department of the Navy Naval Systems Command

Little, A.D., (1967), Internal Waves in the Ocean, ASW Sonar Technology Report No. 4321267, Department of the Navy Naval Systems Command, N00024-68-C-1137, Project Serial Number SF-101-03-21, Task 08648, December 1967

Longuet-Higgins, M.S., and Steward, R.W., (1960), Changes in the form of Short Gravity Waves on Long waves and in Tidal Currents, J. Fluid Mech., 8., 565-533

Maze, M.R., (1980), Formation d'ondes internes stationnaires sur le talus continental. Application au Golfe de Gascogne, Annales Hydrographiques, Nr 754, 45-58

Meadows, G.A., (1983), SEASAT Synthetic Aperture Radar Observations of Wave-Current and Wave-Topography interactions, J. Geophys. Res., Vol 88 No C7, 4393-4405

Meadows, G.A., Shuchman, R.A., and Lyden, J.D., (1982), Analysis of Remotely Sensed Long-Period Wave Motions, J. Geophys. Res., Vol 87 No C8, 5731-5740

Mitchel, R.H., (1982), Synthetic aperture radar (SAR) image quality considerations, Optical Engineering, Vol 21 No 1; 48-55

Millot, C., Lamy, A., (1980), Variabilite et discontinuites des caractères physiques dans l'Ocean Atlantique a l'Est du du West, Laboratoire l'Oceanographie Physique- Museum National d'Histoire Naturelle, Rapport interne Nr 80.04, June 80

Mollo-Christensen, E., (1982), Surface Wave Modulation Patterns in Radar Images, Naval Research Reviews, Vol XXXIV One 40-50

Mollo-Christensen, E., and Mascarenhas, A.Da.S., Jr, (1979), Heat Storage in the Oceanic Upper Mixed Layer Inferred from Landsat Data, Science, 203, 653-654

Mooers, C.N.K., (1971), Documentation on program IMSIWEG, unpublished.

Mooers, C.N.K., (1975(a)), Several Effects of Baroclinic Currents on the Three-Dimensional Propagation of Inertial-Internal Waves, Geophysical Fluid Dynamics, Vol.6, 277-284

Mooers, C.N.K., (1975(b)), Several Effects of a Baroclinic Current on the Cross-Stream Propagation of Inertial-Internal Waves, Geophysical Fluid Dynamics, Vol6, 245-275

Mooers, C.N.K., (1977), Frontal Dynamics and Frontogenesis, in "Oceanic Fronts and Coastal Processes", Proceedings of a Workshop, held at the Marine Sciences Research Center May 25-27 1977, edited by Bowman, M.J., and Esaias, J.E.

Mooers, C.N.K., (1975), Sound Velocity Perturbations due to low frequency motions in the ocean, J. Ac. Soc. Am., Vol 57, No5, May 1975

Mitchell, R.H., (1982), Synthetic aperture radar image quality considerations, Optical Engineering, 21(1) 048-055

Mowbray, D.E, Rarity, B.S.H., (1967), A theoretical and experimental investigation of the phase configuration of internal waves of small amplitude in a density stratified liquid, J. Fluid Mech., Vol 28 part 1, 1-16

Osborne, A.R., Burch, T.L., (1980), Internal Solitons in the Adaman Sea, Science, Vol 208, Nr 4413, 451-460

Phillips, O.M., (1981), The Structure of Short Gravity Waves on the Ocean Surface, In "Spaceborne Synthetic Aperture Radar for Oceanography", 24-31 edited by R.C.Beal, P.Deleonibus and I.Katz, John Hopkins Press,Baltimore Md.

Phillips, O.M., (1973), On the Interaction between Internal and Surface Waves, Phys.Atmos.Oceans, 9,954-961

Pingree, R.D., Griffiths, D.K., (1982), Tidal friction and the diurnal tides on the North-West European Shelf, J.mar.biol.Ass.UK., 62, 577-593

Pingree, R.D., Griffiths, D.K., (1974), The turbulent layer on the continental shelf, Nature, 250, 720-722

Pingree, R.D., Griffiths, D.K., (1981), S2 tidal simulations on the North-West European Shelf, J.mar.biol.Ass.UK., 61, 609-616

Pingree, R.D., Mardell, G.T., (1981), Slope turbulence, internal waves and phytoplancton growth at the Celtic Sea skelf-break, Phil.Trans.R.Soc.London, A302, 663-682

Pingree, R.D., and others, (1982), Celtic Sea and Armorican current structure and the vertical distributions of temperature and chlorophyll, Continental Shelf Research, Vol1,Nr1, 99-116

Pingree, R.D., (1978), Cyclonic eddies and cross-frontal mixing, J.mar.biol.Ass.UK., 58, 955-963

Pingree, R.D. (1979), Baroclinic eddies bordering the celtic sea in late summer, J.mar.biol.Ass.UK., 59, 689-698

Pingree, R.D., (1975) The advance and retreat of the thermocline on the Continental Shelf, J.mar.biol.Ass.UK., 55, 965-974

Pravdo, S., Huneycutt, B., Holt, B., Held, D., (1983), Seasat Synthetic-Aperture Radar Data User's Manual, JPL Publication 82-90

Prony, J.R., and Apel, J.R., (1975), On the use of High Frequency acoustics for the study of internal waves, J. Geophys. Res., 80, 75

Raillard, J., (1975), Les zones frontales dans le Nord du Golfe de Gascogne et en Mer Celtique, Rapport Interne de l'Université de Bretagne Occidentale (Septembre(1975)

Rattray, M., Jr., (1960), On the coastal generation of internal tides, Tellus 12 54-62

Sawyer, C., and Apel, J.R., (1976), Satellite Images of Ocean Internal Waves Signature, NOAA / ER Report (Sep)

130

SHOM, (1968), (Service Hydrographique et Oceanographique de la Marine), Courants de Maree dans la Manche et sur les Cotes Francaises de l'Atlantique. Publication No 550

SHOM, (1966), (Service Hydrographique et Oceanographique de la Marine), Instructions Nautiques Serie C, Vol II

Shuchman, R.A., and Zelenka, J.S., (1978), Processing of ocean wave data from a synthetic aperture radar, Boundary Layer Meteorology, Vol13, 181-191

Stommel, H., Meincke, J., Zenk, W., (1977), New animals for the eddy zoo, Polymode News, (unpubl. Newsl.), 22.1

Shuchman, R.A. and Kasischke, (1981) Boundary Layer Meteorology, Vol13, 181-191

Stride, A.H., Tucker, M.J., (1960), Internal Waves and Waves of Sand, Nature, Nr 4754, Dec 10 1950

Sverdrup, H.U., Johnson, M.W., Fleming, R.H., (1942), The Oceans

Swallow, J.C., Gould, W.J., Saunders, P.M., (1977), Evidence for a poleward eastern boundary current in the North Atlantic Ocean, International council for the exploration of the sea C.M. 1977/c: 32

Tomiyasu, K., (1982), Tutorial review of synthetic aperture radar (SAR) with apllications to imaging the ocean surface, Proceedings of the IEEE Vol 66, No 5

Tomiyasu, K., (1982), Synthetic Aperture Radar imaging from an inclined geosynchronous orbit. Geoscience and Remote Sensing, IEEE

Valenzuela, G., (1978), Theories for the Interaction of Electromagnetic and Oceanic Waves-A Review, Boundary-Layer Meteorology, Vol.13, p.61-85

Vesecki, J.F., and Stewart, R.H., (1982), The Observation of Ocean Surface Phenomena Using Imagery from the SEASAT Synthetic Aperture Radar : An Assessment, J. Geophys. Res., Vol 87 #C5 3397-3430, April 30 1982

Warren, B.A., Wunsch, C., (1981), Evolution of Physical Oceanography

Zachariasen, F., (1973), The effects of surface currents on the equilibrium surface-wave spectral energy density, Tech.Rep.JSR-73-2, Stanford Res.Inst.,Menlo Park,Calif.

INITIAL DISTRIBUTION LIST

No. Copies

1. Defense Technical Information Center   2
   Cameron Station
   Alexandria, Virginia 22314

2. Library, Code 0142   2
   Naval Postgraduate School
   Monterey, California 93943

3. Professor C.N.K. Mooers, Chairman, Code 68Mr   2
   Department of Oceanography
   Naval Postgraduate School
   Monterey, California 93943

4. Professor R.J. Renard, Chairman, Code 63Rd   1
   Department of Meteorology
   Naval Postgraduate School
   Monterey, California 93943

5. Dr. J.L. Mueller, Code 68My   1
   Department of Oceanography
   Naval Postgraduate School
   Monterey, California 93943

6. L.V. Jean-Francois Soubrier   5
   Cellule Operationelle d'Environnement de la Marine
   2, Avenue Rapp
   75340 Paris Cedex 07, France

7. Director   1
   Naval Oceanography Division
   Naval Observatory
   34th and Massachusetts Avenue NW
   Washington, D.C. 20390

8. Commander   1
   Naval Oceanography Command
   NSTL Station
   Bay St. Louis, MS 39522

9. Commanding Officer   1
   Naval Oceanographic Office
   NSTL Station
   Bay St. Louis, MS 39522

10. Commanding Officer   1
    Fleet Numerical Oceanography Center
    Monterey, Ca 93943

11. Commanding Officer   1
    Naval Ocean Research and Development Activity
    NSTL Station
    Bay St. Louis, MS 39522

12. Commanding Officer   1
    Naval Environmental Prediction Research Facility
    Monterey, CA 93943

13. Chief of Naval Research   1
    800 N. Quincy Street
    Arlington, VA 22217

14. Scientific Liaison Office   1
    Office of Naval Research
    Scripps Institution of Oceanography
    La Jolla, CA 92037

15. Library   1
    Scripps Institution of Oceanography
    P.O. Box 2367
    La Jolla, CA 92037

16. Library   1
    Department of Oceanography
    University of Washington
    Seattle, WA 98105

17. Library   1
    School of Oceanography
    Oregon State University
    Corvallis, OR 97331

18. Commanding Officer   1
    Naval Oceanography Commander Center, Rota
    Box 31
    Fleet Post Office
    San Francisco, CA 09540

19. Jet Propulsion Laboratory   2
    California Institute of Technology
    4800 Oak Drive, Pasadena, Ca 91109

20. SACLANT ASW Research Center   2
    (1 for R. Molcard, Applied Oceanography Group)
    Viale San Bartolomeo 400
    I- 19026- LA SPEZIA- Italy

21. Professor Emeritus G. Haltiner, Code 63   1
    Department of Meteorology
    Naval Postgraduate School
    Monterey, Ca 93943

22. Dr R.H. Bourke Code 68Bf   1
    Department of Oceanography
    Naval Postgraduate School
    Monterey, Ca 93943

23. Mr C.R. Dunlap Code 68Du   1
    Department of Oceanography
    Naval Postgraduate School
    Monterey, Ca 93943

24. Professor G. Cantin, Code 69Ci   1
    Department of Mechanical Engineering
    Naval Postgraduate School
    Monterey, California 93943

25. Dr A. Coppens, Code 61Cz   1
    Department of Physics
    Naval Postgraduate School
    Monterey, California 93943

26. Monsieur l'Amiral   3
    Chef d'Etat-Major de la Marine
    2 rue Royale
    75200 Paris Naval, France

27. Monsieur le Contre-Amiral   2
    Attache Naval aupres de l'Ambassade de France
    a Washington.
    1759 R Street NW,
    Washington, D.C. 20008

28. Monsieur le Capitaine de Vaisseau   2
    Commandant le CEPMAN
    BP 38, 83800 Toulon Naval, France

29. Capitaine de Vaisseau (e.r.) Beydon   1
    Meteorologie Nationale (Meteo/Maritime)
    92106 Boulogne Billancourt Cedex, France

30. Meteorologie Nationale   1
    SMM/Documentation
    2 Avenue Rapp
    75340 Paris Cedex 07, France

31. Monsieur l'Ingenieur en Chef de l'Armement   1
    Directeur de l'EPSHOM
    B.P. 426
    29275 Brest Cedex, France

32. Centre National pour l'Exploitation des Oceans 1
    COB/BNDO
    B.P. 337
    29273 Brest Cedex, France

33. Mr Michel Lefebvre   1
    Centre de Recherches et de Geodesie Spatiale
    18 av. Edouard Belin
    31055 Toulouse Cedex, France

134

34. Monsieur le Directeur   1
    Centre de Meteorologie Spatiale
    22300 Lannion, France

35. Capitaine de Corvette Laurent Monsaingeon   1
    Cellule Operationelle de la Marine
    2, Avenue Rapp
    75340 Paris Cedex 07, France

36. Mr. Robert Beal   1
    The Johns Hopkins University
    Applied Physics Laboratory
    Laurel, Md 20707

37. Professor A.R. Robinson   1
    Division of Engineering and Applied Physics
    Harvard University
    Cambridge, Ma 02138

38. Lcdr. B. Johnsen,   1
    619 Hillcrest Avenue
    Pacific Grove, Ca, 93950
    Monterey, California 93943

39. Dr. D.S. Yost, Code 56Yo   1
    Department of National Security Affairs
    Naval Postgraduate School
    Monterey, California 93943

40. Lieutenant (J.G) D. Durban, USN   1
    NAVOCEANCOMPAC, Keflavik IC
    FPO New York, NY 09571

END

FILMED

1-84

DTIC